TEM investigation of rapidly deformed Cu and Mo shaped charge liner material

By

Shaun Cronjé

B.Sc. Hons.

A dissertation submitted in fulfilment of the requirement for the degree

MAGISTER SCIENTIAE

in the

Department of Physics
Faculty of Natural and Agricultural Sciences

at the

University of the Free State
Republic of South Africa

***Supervisor*: Dr. R.E. Kroon**
***Co-supervisor*: Prof W.D. Roos**
***Date*: May 2007**

'Because there is no evil in this world, only evil men.'

Acknowledgements

The author wishes to thank the following individuals and institutions:

- Dr R. E. Kroon, my supervisor for his patience, advice and showing interest in my work and life. You have showed me the meaning of being a true scientist.

- Prof W. D. Roos, my co–supervisor for his advice and jokes.

- All the staff at the Instrumentation Unit at the University of the Free State. Without your talents, this project would never have been completed.

- The staff and students at the Nelson Mandela Metropolitan University. You welcomed me with open arms and never hesitated to help me when I needed it. A special thanks to Prof J.H. Neethling for his help with the Transmission Electron Microscopy work.

- Prof G.N. Nurick for hosting me at the Blast Impact and Survivability Research Unit at the University of Cape Town, and Mr T. Cloete for his assistance with the Split Hopkinson Pressure Bar.

- Prof. P.W.J. van Wyk and Ms. B.B. Janecke at the Centre for Confocal and Electron Microscopy.

- Prof J.A.A Engelbrecht for useful discussions.

- Denel Land Systems and Dr J. Terblanche for providing the shaped charge liners and funding.

- This material is based upon work supported by the National Research Foundation. This assistance is gratefully acknowledged.

- The staff and students at the Department of Physics, University of the Free State.

- My family and friends for their support and patience.

- Nicoline, for her love, support and taking the good with the bad.

- My Here God….. vir “Uitkoms”.

Abstract

The strength and ductility of metals is a vast and important research area in which certain trends are well known, but where it is difficult to predict results with a high level of certainty, especially under extreme conditions e.g. high strain rates and very small grain sizes. Results may also be strongly influenced by impurities. All of the above factors play a vital role in the performance of shaped charge liners. Of particular interest is the material used in the manufacturing of liners. The microstructure and extended defects of copper and molybdenum shaped charge liners were investigated.

Samples were extracted from the liners by electric discharge machining, to minimize any microstructural damage. Chemical testing revealed a higher than expected impurity concentration. Samples were annealed under two different annealing conditions, in order to obtain a variety of starting microstructures. Copper samples were annealed at 300˚C for 30 minutes and 500˚C for 30 minutes. Molybdenum samples were annealed at 1200˚C for 30 minutes and 1200˚C for 3 hours. These samples were then deformed at high strain rates using a split Hopkinson pressure bar. Two strain rates were used, the higher strain rate being approximately twice that of the lower strain rate. For both the copper and molybdenum the lower strain rate was on average 700 s^{-1}, while the higher strain rate was on average 1550 s^{-1} and 1650 s^{-1} in the case of copper and molybdenum respectively. In the case of the molybdenum, the results showed a strong strain rate dependency of the yield strength which is typical of body centred cubic materials, whereas no such strain rate dependency could be detected in the copper results. Both materials show significant softening due to annealing, but relatively small changes between less and more intense annealing procedures. The unannealed samples showed significant variation in the stress-strain results, which is attributed to them originating from different parts of the liner. The uniformity of results after annealing indicates that the stress-strain properties of both materials after annealing are not strongly dependent on their prior straining history.

The microstructure of these samples was examined using an optical microscope as well as a scanning electron microscope. The grain size was determined using the Heyn method. The as-received copper material had an elongated and heavily deformed microstructure. The lower annealing temperature produced a recrystallised grain structure, having an average grain size of 5 μm. The higher annealing temperature allowed grain growth with grains averaging 9 μm. The annealed copper samples contained annealing twins. In the case of molybdenum, the as-received material consisted of large (200 μm) grains. Annealing under both annealing conditions produced the same recrystallised, non-uniform grain structure with grains ranging from 47 μm to 92 μm.

Transmission electron microscopy investigations of the samples revealed that deformation twinning occurred in the annealed and strained copper samples. This twinning occurred at a lower strain rate than expected. Dislocations in an annealed but unstrained copper sample occurred in entangled networks separated with areas containing no dislocations. These mixed dislocations were found to have Burgers vectors of the type $\mathbf{b} = {}^{a}/_{2}\langle 110\rangle$. Pure edge dislocations with a [100] projected direction in the (110) plane with a Burgers vector of the type $\mathbf{b} = {}^{a}/_{2}[1\,\bar{1}\,0]$ were also found. These dislocation arrays appear as ripple like structures. No evidence of twinning was found in the molybdenum samples. Some dislocations with Burger vectors of the type $\mathbf{b} = {}^{a}/_{2}\langle 111\rangle$ were found in the molybdenum samples. There are however exceptions, which is difficult to explain. This is an important observation, and further research would have to be performed.

Opsomming

Die ondersoek na die mikrostrukture in vervormde metale is van groot belang vir verskeie industriële toepassings. Die fundamentele gedrag van metale as gevolg van vervorming, is goed gedokumenteer. Daar is egter sekere toestande van vervorming waar die resultate moeilik is om te voorspel en ook nie goed verstaan word nie. Diè toestande sluit in vervorming teen hoë vervormingstempo's en vervorming van metale met 'n klein korrelstruktuur. Beide hierdie toestande speel 'n rol tydens die ontsteking van 'n holladingplofkop. Van besonderse belang, is die materiaal wat gebruik word in die vervaardiging van holladingplofkoppe. Die mikrostruktuur en defekte van koper en molibdeen holladingplofkoppe is ondersoek.

Monsters is uit holladingplofkopkegels, met 'n vonkerosiemasjien gesny. Hierdie tegniek is gebruik om te verseker dat die minimum verandering aan die mikrostruktuur van die materiaal veroorsaak word. Chemiese analiese het aangetoon dat beide materiale meer onsuiwerhede bevat het as wat verwag was. Kopermonsters is by 300˚C en 500˚C vir 30 minute elk uitgegloei, terwyl die molibdeen monsters teen 1200˚C vir 30 minute of 1200˚C vir 3 ure uitgegloei is. Die monsters is daarna teen verskillende tempo's met behulp van 'n splyt-Hopkinson-drukstaaf vervorm. Twee vervormingstempo's is gebruik met die hoër tempo ongeveer twee maal die van die laer tempo. Vir beide die materiale was die lae tempo 'n gemiddeld van 700 s^{-1}, terwyl 'n hoë tempo van 1550 s^{-1} en 1650 s^{-1}vir die koper en molibdeen onderskeidelik gebruik is. Molibdeen resultate toon 'n sterk vervormingstempo afhanklikheid, tipies van binnesentries kubiese materiale, terwyl geen so 'n afhanklikheid vir die koper waargeneem kon word nie. Albei materiale toon aansienlike versagting a.g.v. uitgloeiing, maar geen verskille in hardheid tussen die uitgloei prosedures nie. Aangesien monsters uit verskillende dele van die kegels afkomstig was, het 'n groot variasie in die resultate van onverhitte monsters voorgekom. Dit wil blyk dat die vervorming eienskappe van metale onafhanklik is van die uitgloei geskiedenis, aangesien die verhitte monsters uniforme resultate gelewer het.

Aftaselektronmikroskoop en optiese mikroskoop resultate toon dat die koper, voor uitgloeiing, ‘n hoogs vervormde en verlengde korrelstruktuur het. Deur die Heyn metode te gebruik is gevind dat die gemiddelde korrelgrootte by 300˚C, 5 µm was en by 500˚C, 9 µm. Uitgloeitweelinge is ook in hierdie koper monsters opgemerk. In die geval van molibdeen het die onverhitte monsters ‘n groot (200 µm) korrelstruktuur gehad. Uitgloeing onder beide toestande het dieselfde herkristalliseerde struktuur met ‘n korrelgrootte van tussen 47 µm en 92 µm opgelewer.

In ‘n transmissie-elektronmikroskoop-ondersoek is die voorkoms van vervormings tweelinge in beide die verhitte en vervormde kopermonsters ook opgemerk. Hierdie tweelingvorming het by ‘n laer vervormingstempo as wat verwag was plaasgevind. Ontwrigtingsnetwerke het in ‘n verhitte, maar onvervormde koper monster voorgekom. Hierdie gemengde ontwrigtings is gekenmerk deur ‘n Burgers vektor **b** = $^{a}/_{2}$<110>. Suiwer kantontwrigtings met ‘n [100] geprojekteerde rigting in die (110) vlak met ‘n Burgers vektor **b** = $^{a}/_{2}[1\bar{1}0]$ is ook gekry. Hierdie ontwrigtings manifesteer as riffels. Geen teken van tweelinge is in die molibdeen monsters gevind nie. ‘n Aantal ontwrigtings met ‘n Burgers vektor **b** = $^{a}/_{2}$<111> is gevind. Daar is wel uitsonderings wat moeilik is om te verklaar. Hierdie is ‘n belangrike waarneming en vereis verdere ondersoek.

Key words

Copper

Deformation

Grain size

High Strain Rate

Microstructure

Molybdenum

Shaped Charge Liner

Split Hopkinson Pressure Bar

Stress-Strain

Transmission Electron Microscopy

Twinning

Acronyms

AES	Auger Electron Spectroscopy
AFM	Atomic Force Microscopy
ASTM	American Society for Testing and Materials
BCC	Body Centred Cubic
BF	Bright field
BISRU	Blast Impact and Survivability Research Unit
BSED	Backscattered Electron Detector
CCD	Charge Coupled Device
CD	Charge Diameter
CSIR	Council for Scientific and Industrial Research
DC	Direct Current
DF	Dark Field
EBSD	Electron Backscattered Diffraction
EDM	Electric Discharge Machining
EDS	Energy Dispersive X-ray Spectroscopy
ETP	Electrolytic Tough Pitch
FCC	Face Centred Cubic
GDMS	Glow Discharge Mass Spectrometry
GDOS	Glow Discharge Optical Spectroscopy
HCP	Hexagonal Close Packed
HERF	High Energy Rate Fabrication
ICPMS	Inductively Coupled Plasma Mass Spectrometry
IGA	Interstitial Gas Analysis
NMMU	Nelson Mandela Metropolitan University
OFHC	Oxygen Free High Conductivity
ppm	parts per million
RSF	Relative Sensitivity Factor
SAD	Selected Area Diffraction
SED	Secondary Electron Detector
SEM	Scanning Electron Microscope
SHPB	Split Hopkinson Pressure Bar
TEM	Transmission Electron Microscope
UFS	University of the Free State

Contents

Chapter 1

Introduction

1.1 Overview 1
1.2 Research objectives 2
1.3 Dissertation layout 3
1.4 References 4

Chapter 2

Literature study on Shaped Charges

2.1 Introduction to shaped charges 5
2.2 Materials and manufacturing methods for shaped charges and their effects on penetration performance 6
2.2.1 Liner materials 7
2.2.2 Microstructure and extended defects 8
2.2.3 Manufacturing processes for shaped charge liners 9
2.2.4 Liner design 11
2.3 Models for jet breakup time based on microstructure 12
2.3.1 Decreasing dislocation density model 12
2.3.2 Void growth model 13
2.3.3 Grain boundary impurity concentration model 13
2.4 Summary 14
2.5 References 15

Chapter 3

Literature study on the high strain rate plastic deformation of metals

3.1 Dislocations and other defects in FCC and BCC metals 17

3.1.1 Basic classifications of dislocations 17

3.1.2 Slip and slip directions 19

3.1.3 Surface defects – grain boundaries, stacking faults and twin boundaries 20

3.1.4 Control of grain size 27

3.2 Low strain rate plastic deformation of metals 28

3.2.1 The Tensile Test and Stress – Strain Diagram 28

3.3 Literature results for plastically deformed copper 31

3.3.1 Introduction 31

3.3.2 Effect of grain size on high strain rate deformation of copper 31

3.3.3 Dynamic recrystallisation 33

3.3.4 Deformation mechanisms 35

3.3.5 Voids 38

3.3.6 Impurities 38

3.4 Literature results for plastically deformed molybdenum 40

3.5 Literature results for plastically deformed tantalum 42

3.6 Summary 44

3.7 References 46

Chapter 4

An overview of experimental techniques

4.1 Introduction 48

4.2 Spark erosion 49

4.3 Annealing 55

4.4 The Split Hopkinson Pressure 58
4.4.1 History and Experimental Setup 58
4.4.2 Basic theory 60
4.4.3 Calibration 62
4.4.4 Data analysis 64
4.5 Scanning Electron Microscopy (SEM) 68
4.6 Transmission Electron Microscopy (TEM) 70
4.7 Chemical testing 77
4.8 References 85

Chapter 5

Deformation of samples by means of the Split Hopkinson Pressure Bar

5.1 Introduction 87
5.2 Experimental 88
5.2.1 Experimental procedure 88
5.2.2 Data analysis 92
5.3 Results and Discussion for copper 95
5.4 Results and Discussion for molybdenum 103
5.5 Comparison between copper and molybdenum 109
5.6 References 111

Chapter 6

Determination of sample grain size

6.1 Introduction 112
6.2 Experimental 112
6.2.1 Polishing of the samples 113

6.2.2 Etching of the samples 114
6.2.3 Imaging of the samples 116
6.2.4 Determination of the average grain size per sample 118
6.3 Results and Discussion for copper 120
6.4 Additional techniques 125
6.5 Results and Discussion for molybdenum 126
6.6 Discussion and Conclusions 130
6.7 References 132

Chapter 7

Transmission Electron Microscope investigation of samples

7.1 Introduction 133
7.2 Experimental 134
7.2.1 Sample Preparation 134
7.2.2 Indexing of diffraction patterns 136
7.2.3 Camera lengths 138
7.2.4 Rotation Calibration 140
7.3 Results for copper 143
7.3.1 Dislocations 145
7.3.2 Twins 152
7.3.3 Ripples 156
7.3.4 Oxide layer 160
7.3.5 Ion milling damage 164
7.4 Results for molybdenum 165
7.4.1 Overview 165
7.4.2 Dislocation analysis 169
7.5 Discussion and conclusion 176
7.6 References 178

Chapter 8

Final Conclusions and Remarks

8.1 Introduction 180
8.2 Conclusions regarding the copper used in this study 180
8.3 Conclusions regarding the molybdenum used in this study 182
8.4 General comments and suggestions for future work 183

Chapter 1

Introduction

1.1 Overview

The strength and ductility of metals is a vast and important research area in which certain trends are well known, but where it is difficult to predict results with a high level of certainty, especially under extreme conditions e.g. high strain rates, high temperatures and very small grain sizes. In addition, results may be strongly influenced by impurities. All of the above factors play a vital role in the performance, use and effectiveness of shaped charge liners.

A shaped charge is an explosive device in which a concave metal hemisphere or cone, called a liner, is surrounded by a high explosive charge and enclosed in a steel or aluminium casing. Upon detonation, the liner material is deformed at a very high strain rate and ejected as a high velocity jet of material which has great penetrative power. The study of shaped charges is of great importance since they have both military and civil (e.g. demolition, drilling) applications (Baum, 2005). The effectiveness of shaped charges depends on a range of factors, which include liner design, the materials employed and the manufacturing process.

Of particular interest is the material used in the manufacturing of liners. Since the penetration potential is linked to the jet length and momentum characteristics it follows that the material to be used must optimally be both ductile and dense (McWilliams *et al.*, 2002). Experiments have however shown that this is not necessarily the case. Lead which has a higher density than the more commonly used copper, and which likewise has a face centred cubic structure (FCC) which would indicate excellent ductility, underperforms by a considerable margin. Graphite and ceramic cones with negligible ductility have shown reasonable penetration into steel targets (Doig, 1998).

A phenomenon that inhibits penetration is jet break up. By means of x-ray flash photography it has been frequently observed that the jet breaks up into a discontinuous array of fragments (McWilliams *et al.*, 2002). It is preferable to have a continuous jet impacting on the target.

Past research on shaped charge liners were conducted mainly on oxygen free high conductivity (OFHC) copper. Although actively researched (e.g. Zernow and Lowry, 1992, Gurevitch *et al*., 1992, Meyers *et al.,* 1992, and Gourdin, 1992), copper is still not fully understood. The current trend is to investigate the possible use of molybdenum and tantalum. Copper has a face centred cubic (FCC) structure, whereas molybdenum has a body centred cubic (BCC) structure: therefore it is suspected that the manner in which these materials respond to deformation will be fundamentally different.

Shaped charge predictions based on hydrocodes treat jet deformation as in a continuous fluid (Mostert *et al.*, 1987). Yet grain size is known to affect shaped charge performance. This effect cannot be explained by fluid dynamics models, nor can the models explain the difference in behaviour between materials with FCC and BCC structures. In addition, X-ray diffraction patterns of aluminium and copper have shown that shaped charge liner jets remain in the solid state (Gurevitch *et al*., 1992).

From the above it is clear that extensive experimental research is needed in order to obtain a better understanding of the processes and factors involved in the high strain rate deformation of metals. From this it might be possible to construct models which are able to accurately predict the deformation behaviour of metals.

1.2 Research objectives

The aim of this project was to characterize the microstructure and extended defects of shaped charge liners. Samples were extracted from copper (Cu) and molybdenum (Mo) liners provided by Denel Land Systems by means of Electric Discharge Machining (EDM), also commonly known as spark erosion. These samples were then

annealed at various temperatures and then compressed at various strain rates using a Split Hopkinson Pressure Bar (SHPB). Investigation of the resulting microstructure was then performed using among others Scanning Electron Microscopy (SEM) and Transmission Electron Microscopy (TEM). Comparisons were made regarding the roles that crystal structure, microstructure and strain rate play in the high strain rate deformation of metals.

Although beyond the scope of the present project, it is hoped that this information can be used to find and explain some correlation between these properties and the high strain rate ductility of these metals.

1.3 Dissertation layout

Chapter 1 includes the introduction and aim of this study. This is followed by *Chapter 2*, in which the shaped charge is described in detail. An overview of models for jet break up-time based on microstructure is also given. Complimentary to this, *Chapter 3* discusses defects in cubic crystal structure metals and past research done on plastically deformed metals. *Chapter 4* gives background information regarding the theory and use of the most important experimental techniques used during the course of this study including, but not limited to EDM, SHPB, SEM and TEM. This chapter also includes a detailed description on the extraction of samples from the shaped charge liners using EDM, and the heat treatment procedures for these samples. The chemical analysis that was done on each material (copper and molybdenum) to determine the exact elemental make-up used is also discussed. The results of compression tests done on the samples and a complete discussion on this subject can be found in *Chapter 5*. *Chapter 6* gives an in depth discussion on the grain structure of each sample. This is then followed in *Chapter 7* by a discussion on the microstructure of each sample as investigated by means of TEM. The conclusion as well as recommendations for future work is outlined in *Chapter 8*.

1.4 References

Baum D. **[2005]** www.llnl.gov/str/Baum.html, Downloaded: 2005-08-25

Doig A. **[1998]** *Journal of Battlefield Technology* **1(1)** p1

Gourdin W.H. **[1992]** *Characterization of Copper Shaped-Charge Liner Materials at Tensile Strain Rates of* $10^4 s^{-1}$ in *Shock-Wave And High–Strain-Rate Phenomena In Materials* (Meyers M.A., Murr L.E. and StaudHammer K.P.), Marcel Dekker Inc.

Gurevitch A., Murr L.E., Varma S.K., Thiagarajan S. and Fisher W.W. **[1992]** *Comparative Studies of Shaped Charge Component Microstructures* in *Shock-Wave And High–Strain-Rate Phenomena In Materials* (Meyers M.A., Murr L.E. and StaudHammer K.P.), Marcel Dekker Inc.

McWilliams S.T., Baker E.L., Ng K.W., Vuong T. and Mazeski R.P. **[2002]** International Infantry and Small arms conference, Atlantic City, USA p1

Meyers M.A., Meyer L.W., Beatty J., Andrade U., Vecchio K.S. and Chokski A.H. **[1992]** *High Strain, High-Strain-Rate Deformation of Copper* in *Shock-Wave And High–Strain-Rate Phenomena In Materials* (Meyers M.A., Murr L.E. and StaudHammer K.P.), Marcel Dekker Inc.

Mostert, F.J. and König, P.J **[1987]** *S. Afr. J. Physics*. **10(3)** p127

Zernow L. and Lowry L **[1992]** *Deformation of Copper in Shaped Charge Jets* in *Shock-Wave And High–Strain-Rate Phenomena In Materials* (Meyers M.A., Murr L.E. and StaudHammer K.P.), Marcel Dekker Inc.

Chapter 2

Literature study on Shaped Charges

2.1 Introduction to shaped charges

As mentioned in chapter 1, a shaped charge is an explosive device in which a thin concave metal hemisphere or cone, called a liner, is surrounded by a high explosive charge and enclosed in a steel or aluminium casing (see figure 2.1).

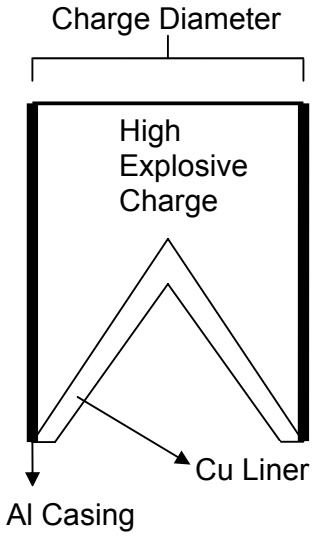

Figure 2.1: Shaped charge warhead construction.

Upon detonation, the liner material is deformed at a very high strain rate and part of it is ejected as a high velocity jet of material which has great penetrative power (see figure 2.2). The study of shaped charges is of great importance since they have both military and civil (e.g. demolition, drilling) applications (Baum, 2005).

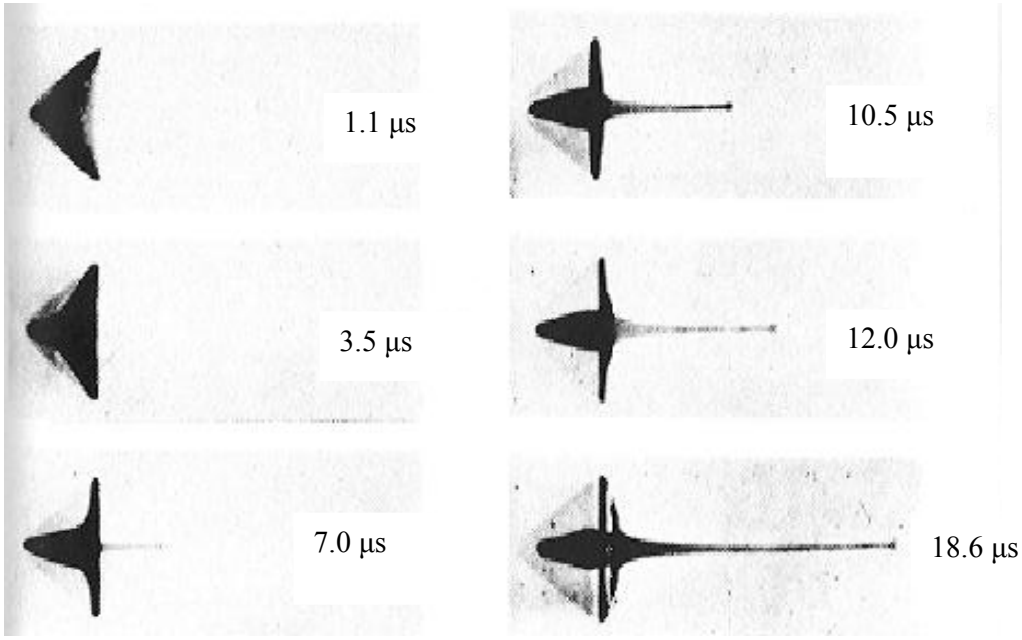

Figure 2.2: X-ray photograph of jet formation. Time given are the elapsed time after the detonation wave reached the apex of the liner (Walters, 1998, p339).

2.2 Materials and manufacturing methods for shaped charges and their effects on penetration performance

A number of variables are responsible for the penetration performance of shaped charges. The most important of these include liner material, liner microstructure and extended defects, manufacturing method and liner design.

2.2.1 Liner materials

The effect of liner and target densities on penetration performance at constant standoff* can be predicted using the Hill, Mott and Pack hydrodynamic penetration equation,

$$P \propto L\sqrt{\frac{\rho_j}{\rho_t}} \qquad \textbf{(2.1)}$$

that relates the penetration P to the jet length L and the target and jet densities ρ_t and ρ_j respectively (Doig, 2002, p53). Target penetration is improved if jet density, and by implication liner density, is increased as illustrated in figure 2.3. This, however, is only true if the jet length remains long - a phenomenon that degrades penetration is jet break up. By means of x-ray flash photography it has been frequently observed that the jet breaks up into a discontinuous array of fragments (McWilliams *et al.*, 2002). It is preferable to have a continuous jet impacting on the target. A good copper jet will be approximately 8 charge diameters (CD) long in air before it particulates (Doig, 2002, p53).

From the above it is clear that in theory the material to be used must optimally be both ductile and dense. This would suggest that the best performance would be obtained from a very dense metal liner with a face centred cubic (FCC) crystal structure which is inherently ductile. Experimentally this is not always the case. Copper, due to its reasonable density and excellent ductility, has remained the most popular material for shaped charges, yet excellent results have been obtained with certain body centred cubic (BCC) crystal structure materials like tantalum and molybdenum even though the BCC structure should imply that these materials are less than optimally ductile. Even graphite and ceramic cones with negligible ductility have shown decent penetration into steel. In comparison, lead, which has excellent ductility due to its

* Distance between warhead and target surface at time of detonation. See section 2.2.4.

FCC structure and is denser than copper, shows mediocre performance when compared to this material (Doig, 2002, p55).

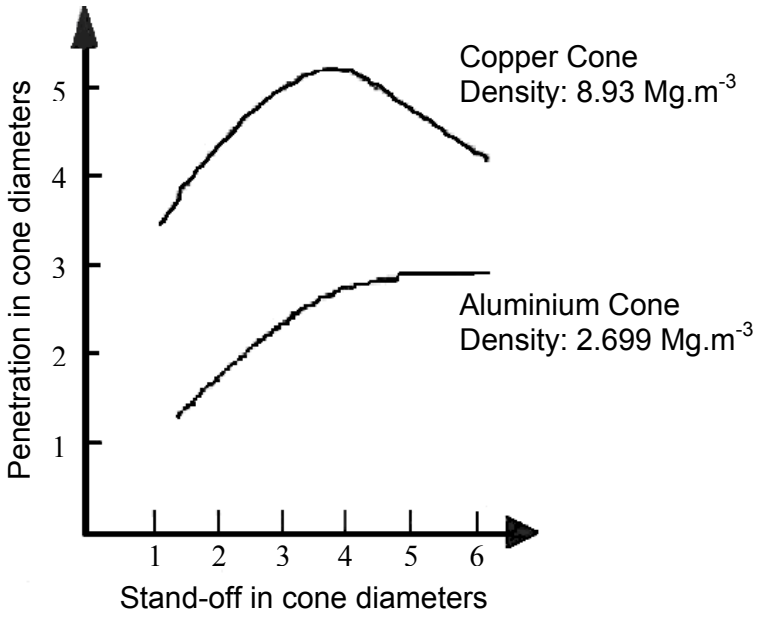

Figure 2.3: Penetration of various cone materials into steel. (Adapted from Doig, 2002, p53; densities from Askeland, 1998, p830)

It should be noted that a solid coherent jet can only be formed if the formation process is subsonic, otherwise the jet will spread out radially. This implies that the collision velocity must be smaller than the liner material bulk speed of sound. A higher collision velocity can thus be used with a material that has a high bulk speed sound i.e. the speed of sound in that specific material (Walters, 1989, p106).

2.2.2 Microstructure and extended defects

The ductility of liner materials during jet elongation, and their tendency to cause jet break up, is strongly correlated to the microstructure of the material used in the liner, as well as to the presence of impurities in the liner material (see section 2.3.3). Liner microstructure is largely dependent on the original material properties and the manufacturing processes used to produce the liner. As microstructure is the main

focus of this dissertation, this topic and its effects on liner performance will be discussed in detail in chapter 3. It is however necessary to note that experimentally the best performance has been obtained with a fine, uniform recrystallised grain structure (Held, 2001; Schmidt *et al.,* 1991).

2.2.3 Manufacturing processes for shaped charge liners

Several manufacturing processes are used for shaped charge liners, each with advantages and disadvantages.

Machining: The production of liners by machining from a copper rod is very expensive and yields a liner with a less than optimal crystal structure due to the nature of the raw material used. Especially in larger rods used to make liners with a charge diameter in excess of 100 mm the crystal structure is not homogeneous, and the grain sizes are large (Held, 2001).

Deep drawing: In this inexpensive technique a liner is formed in a few steps. The process is best suited to the manufacturing of small liners. Larger liners require additional annealing between steps to reduce the strain hardening (Held, 2001).

Cold forging: This technique (also known as the Swiss process) is approximately five times as expensive as deep drawing, but yields a better microstructure. A copper billet is transformed into a liner by repeated pressing and annealing to reduce the strain hardening. Final wall thickness is achieved by machining of the external wall surface. A very fine microstructure can be achieved by recrystallisation annealing (Held, 2001).

Warm forging: Fewer and smaller forging steps than in cold forging are used to form liners at a temperature slightly below the recrystallisation temperature, but higher than the recovery temperature of the material used. A very fine microstructure is achieved using this technique (Held, 2001).

Hot forging: This involves one step forging at a temperature much higher than the recrystallisation temperature and was mainly carried out in earlier times. This forging step is followed by machining of the cone surface to remove the oxidised layer. Although the process is low cost, the microstructure produced is too rough due to grain growth to ensure optimal performance (Held, 2001).

High-energy rate fabrication: A process which produces liners capable of delivering very long jets and break up times is the High-Energy Rate Fabrication (HERF) method. A billet is pressed out by means of a piston impacting on it with a velocity of 20 ms^{-1}. A very fine rotationally symmetric microstructure can be achieved with this technique (Held, 2001).

Electroforming: Good results have also been obtained by liners formed by electroforming copper on a polished mandrel. The process of electroforming is best described as a process similar to electroplating, but one that is used in manufacturing metallic articles, rather than one that produces surface coatings. Copper is electrodeposited onto a conical shape made of stainless steel, which is highly polished to ensure easy separation of the formed liner from the core. Liners are produced with thin, but very long crystallites or dendrites which are oriented to the axis of symmetry (Tian *et al.,* 2003; Held, 2001).

Flow forming: A popular manufacturing process used in the production of copper shaped charges is flowforming. In flowforming an annealed copper blank is plastically deformed by a roller tool over a mandrel at room temperature to achieve the desired shape (see figure 2.4). This plastic deformation causes the cone wall to be thinner than the original plate, and also leads to work hardening. Excess flash material on the rim of the cone is machined off. The cone is then annealed at approximately 500˚C for 30 minutes to remove work hardening by recrystallisation of the grain structure to achieve fully equiaxed grains with a grain size of less than 30 μm (Doig, 2002, p54).

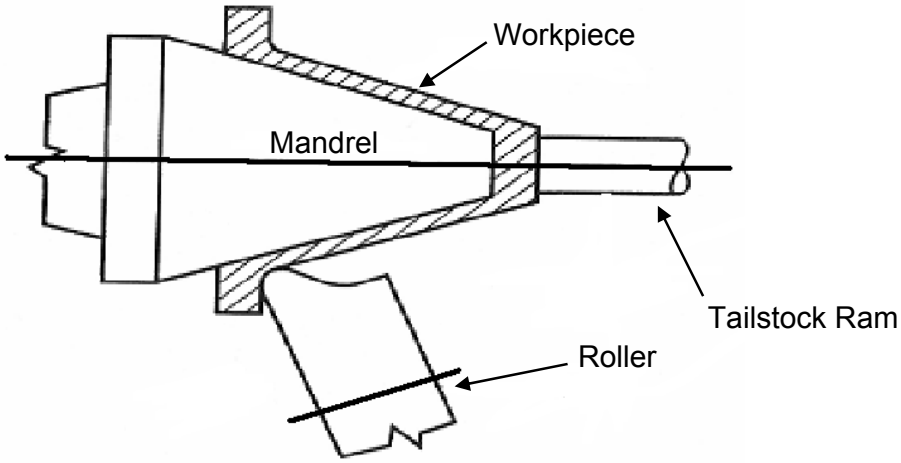

Figure 2.4: Flow forming process. (Adapted from Doig, 2002, p54)

2.2.4 Liner design

Various variables in liner design influence the penetration performance of shaped charges:

Standoff: A built in standoff tube at the front of the liner about two charge diameters long initiates detonation of the explosive charge and allows the jet tip to form and reach full speed before meeting the target. For standoff above eight charge diameters penetration of copper jets rapidly decreases due to the effect of the lateral velocity of particles (see figure 2.3). Later particles might not hit in the same position as the jet tip, resulting in a widening effect of the target crater rather than a deepening effect (Doig, 2002, p56).

Charge diameter: a conical shaped charge diameter will penetrate the same target twice as deeply as a similar liner with half the charge diameter and half the standoff, even though the shock wave velocity of the charge explosion remains the same (Doig, 2002, p56).

Cone geometry: A reduction in penetration is encountered with an increase in cone angle due to the increase in width and weight of the jet which causes a decrease in jet

velocity. A decrease in jet velocity is also obtained if the liner wall thickness is increased beyond an optimal level. (Doig, 2002, p56). A decrease in cone angle causes an increase in jet velocity, but is offset by a decrease in jet mass (Walters, 1989, p311).

Other factors that influences performance, and that must therefore be optimized, includes charge height, case confinement, explosive type and initiation method. These variables are often interlinked.

2.3 Models for jet break up time based on microstructure

Due to the negative effect that jet particulation has on liner performance and penetration, a large amount of research has been conducted on the phenomenon, but without producing a satisfactory and final conclusion. Computer modelling using hydrocodes are an important tool in researching shaped charge liner performance (Doig, 2002, p55). Hydrodynamic deformation is, however, independent of factors like the microstructure of the liner material and external properties of the deformation process like strain rate and temperature. Because these factors play such an important role in the deformation process these models cannot produce an accurate prediction of the performance of a liner (Doig, 2002, p55). Three broad theories exist, which attempt to explain the factors contributing and leading to jet break up.

2.3.1 Decreasing dislocation density model

In 1987, Mostert *et al.* proposed the first model for shaped charge jet break up time that explicitly took microstructure in consideration. By assuming that the initial density of dislocations at the time of jet formation is inversely proportional to the liner grain size, and that it is implicitly related to the shock loading of the liner during the acceleration and the jet formation phase, the model proposed that the jet ductility is

influenced via the behaviour of an excess of moving dislocations. The surface of the jet was considered to be the dominant sink for these dislocations. Plastic deformation ended, and jet break up commenced, when the density of these dislocations had been reduced to a critical level by escape through the surface of the jet.

The model can only predict the number of jet fragments produced if there is a known periodic internal variation in the moving dislocation density along the length of the jet. The model does, however, predict the experimentally found trend between jet ductility and liner grain size, namely that an increase in ductility is observed with a reduction in grain size.

2.3.2 Void growth model

Various researchers have noticed voids and coalesced void tunnels in recovered liner jet fragments. It has been proposed by Gurevitch *et al.* (1993) that due to the prominence that voids assume in recovered jet fragments, their formation may play an important role in the jet formation and instabilities leading to jet break up and fragmentation. In Gurevitch *et al.* (1993), Scanning Electron Microscopy (SEM) examination of recovered copper jet fragments revealed these voids and void tunnels near the tips of the fragments. Additional porosity was also observed in the interior of the fragments, but no voids or porosity was noted in the surrounding copper.

2.3.3 Grain boundary impurity concentration model

It is well known that impurities such as oxygen and sulphur, causes embrittlement in copper and molybdenum (Schwartz *et al.,* 1998). In contrast, the addition of carbon to molybdenum liners can be beneficial as it inhibits the diffusion of oxygen at the grain boundaries (Lightenberger *et al.,* 1996).

Some experiments have shown that liners with larger grain sizes and low impurity concentrations perform better than liners with small grain sizes and higher impurity concentrations (Schwartz *et al.,* 1998), and so it was suggested that the break up time

of jets is fundamentally related to the grain boundary impurity concentration. The combined effect of impurity concentration and grain size was determined, by assuming that all impurity atoms diffuse along, and remain at, the grain boundaries, triple lines, and/or quadruple nodes. A geometrical analysis based on an assumed tetrakaidecahedron grain shape was applied to determine the relationship between grain size, impurity content, and break up time in sulphur doped oxygen free high conductivity (OFHC) copper. The number of impurity atoms as a function of grain size, the number of available sites at crystalline defects, and the intercrystalline impurity concentration was calculated. It was observed that the break up time of copper shaped charge liners doped with sulphur decreased as the grain boundary impurity content increased, which suggests that grain boundary impurity content is a reliable predictor of shaped charge jet ductility. It was suggested that the segregation of impurities to certain types of grain boundaries and the type of dislocations forming the grain boundaries, might also play an important role. Lassila (1992, p543) measured the impurities at brittle fracture surfaces using Auger Electron Spectroscopy and found a correlation between jet particulation and impurities.

2.4 Summary

From the preceding paragraphs, it is clear that the penetration performance of shaped charges is dependent on a number of factors. These factors include liner design, the manufacturing method used, the material used and the actual microstructural properties of the material. Although all these factors are important, only the microstructural properties of the two materials used (copper and molybdenum) are of direct relevance to this study. It is clear that the grain structure of the material, as well as the presence of impurities, porosity and dislocations in the material are of great importance in the outcome of this study.

2.5 References

Askeland D.R. **[1998]** *The Science and Engineering of Materials*, Stanley Thornes Ltd.

Baum D. **[2005]** www.llnl.gov/str/Baum.html, Downloaded: 2005-08-25

Doig A. **[1998]** *Journal of Battlefield Technology* **1(1)** p1

Doig A. **[2002]** *Military Metallurgy*, Maney Publishing.

Gurevitch A.C., Murr L.E., Fisher W.W., Varma S.K and Advani A.H. and Zernow L **[1993]** *Journal of Material Science* **28** p2795

Held M **[2001]** *Journal of Battlefield Technology* **10(3)** p1

Lassila D.H. **[1992]** *Material Characteristics Related to the Fracture and Particulation of Electrodeposited-Copper Shaped Charge Jets* in *Shock-Wave And High–Strain-Rate Phenomena In Materials* (Meyers M.A., Murr L.E. and StaudHammer K.P.), Marcel Dekker Inc.

Lichtenberger A., Verstraete N., Salignon D., Daumas M.T. and Collard J. **[1996]** *16th International Symposium on Ballistics*, San Francisco, USA. p49

McWilliams S.T., Baker E.L., Ng K.W., Vuong T. and Mazeski R.P. **[2002]** International Infantry and Small arms, Atlantic City, USA. p1

Mostert, F.J. and König, P.J **[1987]** *S. Afr. J. Physics*. **10(3)** p127

Schmidt C.G. Caligiuri R.D., Giovanola J.H. and Erlich D.C. **[1991]** *Metallurgical Transactions* **22A** p2349

Schwartz, A.J., Lassila D.H. and Baker E.L **[1998]** *17th International Symposium on Ballistics*, Midrand, South Africa. p439

Tian W.H., Fan A.L., Gao H.Y., Luo J. and Wang Z. **[2003]** *Materials, Science and Engineering* **A350(1-2)** p160

Walters W.P., Zukas J.A. **[1998]** *Fundamentals of Shaped Charges*, CMC Press.

Chapter 3

Literature study on the high strain rate plastic deformation of metals

3.1 Dislocations and other defects in FCC and BCC metals

3.1.1 Basic classification of dislocations

Dislocations are line imperfections in an otherwise perfect lattice. They are formed in materials during solidification, or when the material has been deformed. Two basic types of dislocations, namely screw and edge dislocations, can be identified.

The screw dislocation can be illustrated by cutting partway through a perfect crystal, and then skewing the crystal one atom spacing (see figure 3.1). Critical to understanding dislocations is the Burgers vector. By following a crystallographic plane one revolution around the axis on which the crystal was skewed, starting at point **X**, and travelling an equal amount of atom spacings in each direction, we arrive at point **Y** which is one atom spacing from the starting point **X**. The vector which is required to complete the loop is the Burgers vector **b**. If this rotation is continued, a spiral path would be traced out. The axis around which this path is traced out, is the screw dislocation line. The Burgers vector is parallel to the screw dislocation.

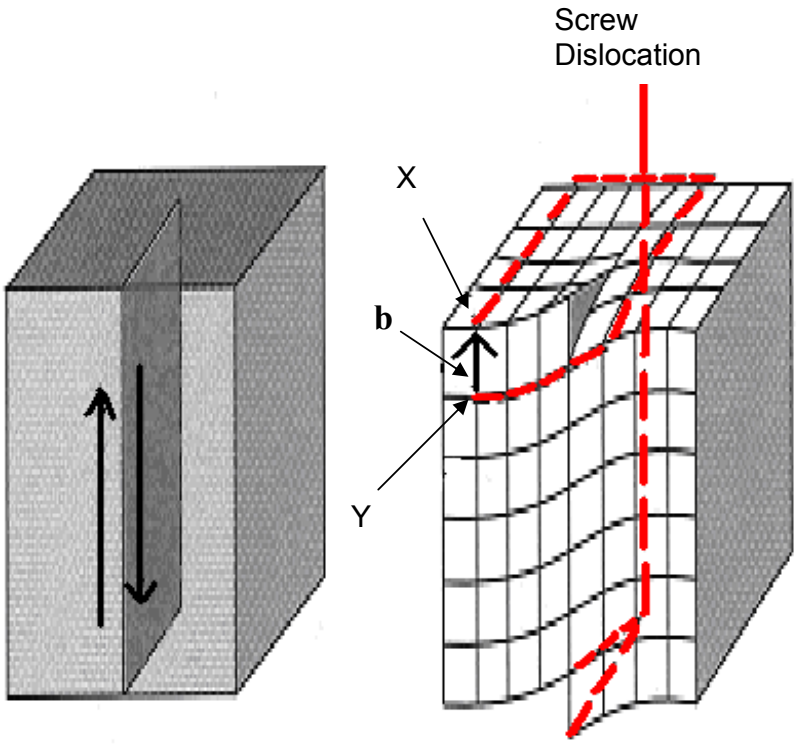

Figure 3.1: Screw dislocation and Burgers vector**.** (Adapted from Askeland, 1998, p80)

An edge dislocation can be illustrated by slicing partway through a perfect crystal, and filling the cut with an additional plane of atoms (see figure 3.2), the bottom edge of this additional plane representing the edge dislocation line. If a clockwise loop is followed around the edge dislocation, starting at point **X** and going an equal number of atom spacings in each direction, a point **Y** is reach one atom spacing from point **X**. The vector required to complete the loop is once again the Burgers vector. In the case of the edge dislocation, the Burgers vector is perpendicular to the dislocation.

It is also possible that mixed dislocations can form. These dislocations have both edge and screw dislocation components, but the Burgers vector remains the same for all portions of the dislocation (Askeland, 1998, pp80, 81).

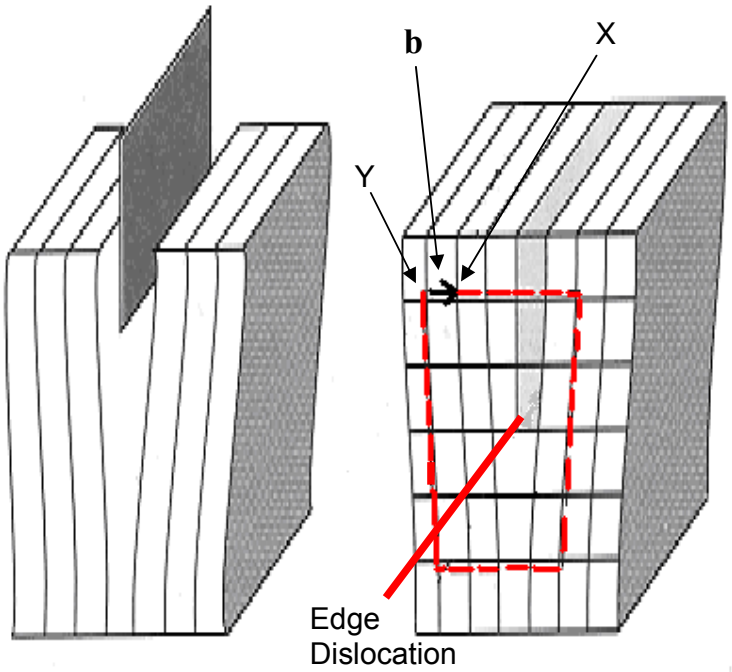

Figure 3.2: An edge dislocation with Burgers vector indicated. (Adapted from Askeland, 1998, p80)

3.1.2 Slip and slip directions

When a shear force is applied to a crystal containing a dislocation, acting in the direction of the Burgers vector of the dislocation, the dislocation can move by breaking the bonds between atoms in one plane. The force needed to initiate this process is called the critical shear stress. This process by which a dislocation moves, and causes a material to deform, is called slip. The direction in which the dislocation moves is called the slip direction, and is almost always the direction in which atoms are most closely packed. In the case of edge dislocations, the slip direction is in the direction of the Burgers vector. In a screw dislocation, the dislocation moves in a direction perpendicular to the Burgers vector, but the crystal deforms parallel to the Burgers vector. FCC metals slip along the <110> directions, while BCC metals slip

along the <111> directions because these are the most densely packed directions for each crystal structure respectively. During slip the dislocation sweeps out the plane formed by the dislocation line and the Burgers vector. This plane, known as the slip plane, together with the slip direction, forms the slip system (Askeland, 1998, p83). The dislocation is the line in the slip plane separating the slipped and unslipped regions. Figure 3.3 illustrates how slip causes deformation of a material. The slip planes for FCC metals are {111}- type, while BCC metals can slip on the {110}, {112} and {123} families of planes (Cottrell, 1956, p3).

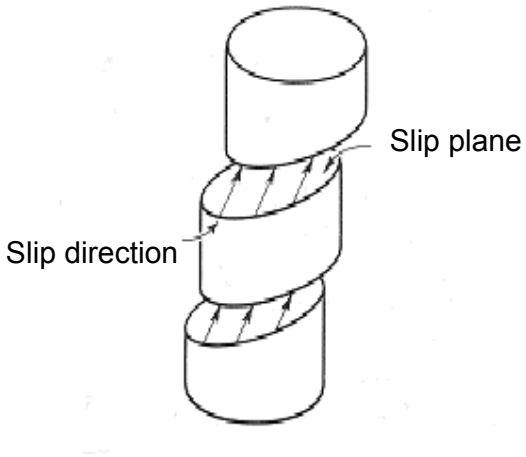

Figure 3.3: Slip and deformation resulting from slip (Barret and Massalski, 1980, p403).

3.1.3 Surface defects – grain boundaries, stacking faults and twin boundaries

The microstructure of metals consists of grains. A grain is a portion of the material in which the arrangement of atoms are the same, but in which the orientation of the lattice differs from each adjoining grain (see figure 3.4). The surface that separates grains is called a grain boundary. As atoms are not evenly spaced in these areas, regions of tension and regions of compression occur.

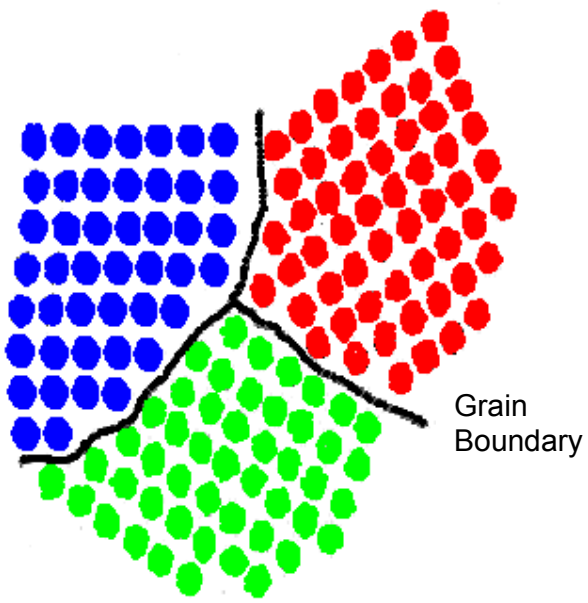

Figure 3.4: Grains and grain boundaries (Askeland, 1998, p97).

Properties of materials are strongly influenced by the size and number of grains they contain. A dislocation can only move until it encounters a grain boundary. It follows then that an increase in grain boundaries will have a strengthening effect on the material. This can be achieved by increasing the number of grains, and hence decreasing the grain size. The relation between grain size and yield strength is given by the Hall - Petch equation

$$\sigma_y = \sigma_0 + \frac{K_s}{\sqrt{d}} \qquad \textbf{(3.1)}$$

where σ_y is the yield strength of the material, σ_0 and K_s are constants for the material and d is the average diameter of the grains (Askeland, 1998, pp 97,98). Note that σ_0 is the yield strength of a single grain, if d approaches ∞.

The preceding paragraph described a high angle grain boundary. Other surface defects that should be considered include small angle grain boundaries, stacking faults and twin boundaries. Small angle grain boundaries are a misorientation or an angular

mismatch, Θ, between adjoining grain boundaries caused by an array of dislocations (see figure 3.5). Because the energy of the surface is less than in the case of normal grain boundaries, the small angle grain boundaries are less effective in blocking slip. Small angle grain boundaries caused by screw dislocation are known as twist boundaries, and in the case of edge dislocations they are known as tilt boundaries. Tilt boundaries can thus be thought of as a series of edge dislocations with separation D (Askeland, 1998, p101; Elliot, p148).

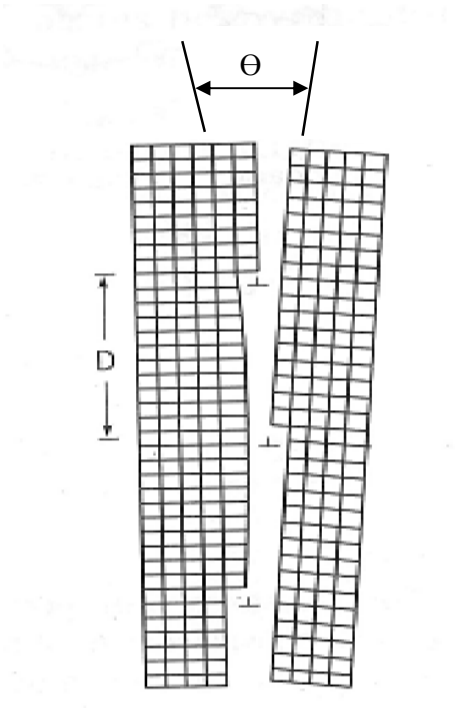

Figure 3.5: Small angle grain boundary (Askeland, 1998, p101).

A common defect in FCC metals which interferes with the slip process is a stacking fault. A stacking fault occurs where there is a change from the normal stacking sequence of the close packed planes. In a perfect FCC lattice a plane stacking sequence of ABCABCABC occurs. Now in the case of a stacking fault, a sequence like ABCAB●ABCABC is possible, the dot merely indicating where a type C plane has been left out (Askeland, 1998, p101). The crystal orientation on both sides of the stacking fault is the same.

When a mirror image misorientation of the lattice structure occurs, it is known as a twin boundary (see figure 3.6).

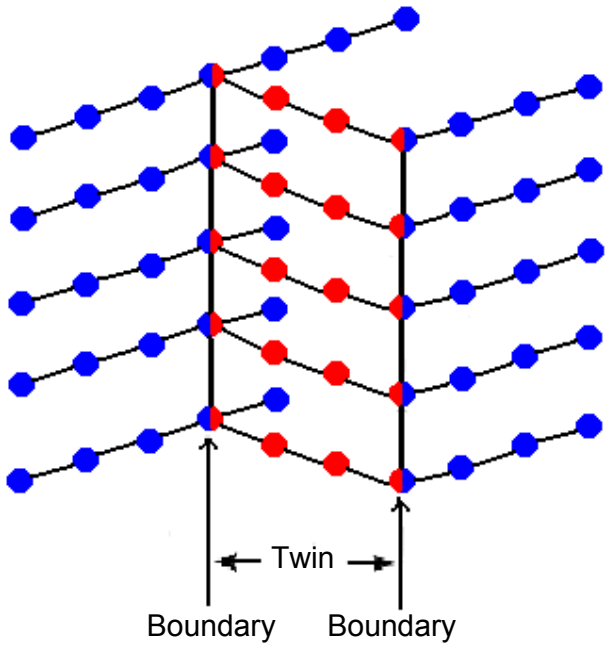

Figure 3.6: Twins (Askeland, 1998, p102)

Twinned crystals consist of two parts symmetrically related to one another either by rotation, or a reflection. Twins are most often encountered after annealing or deformation. It is important to note that the crystal orientation on either side of a twin boundary is not the same, which gives rise to extra diffraction spots (twin spots) in an electron diffraction image. The following is a summary of the discussion on twins from Cullity, 1978, p59 - 62. The relationship between these two parts as described above can be obtained by a reflection across the {111} plane normal to the twin axis. This plane, called the twin plane is also the composition plane. When metallographic analysis of a metal sample takes place, annealing twins may appear in two forms. In figure 3.7(a) one part of the grain (B) is twinned in respect to the other part (A). The two parts are connected on the composition plane (111) which makes a line trace on the plane of polish. The more common variation is seen in figure 3.7(b). The grain shows three parts. Parts A1 and A2 is of identical orientation, but is separated by part B known as a twin band. This twin band is twinned in respect to A1 and A2.

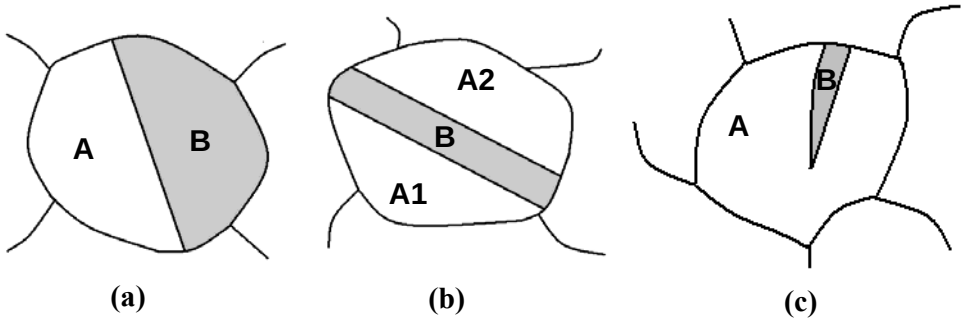

Figure 3.7: (a) Annealing twin of type I, **(b)** Annealing twin of type II, **(c)** Deformation twin. (Adapted from Cullity, 1978, p60).

These twins are the result of a change in the normal growth mechanism. Suppose that during grain growth, a grain boundary is parallel to the (111) plane and is advancing in a direction normal to this boundary [111]. During this advancing, atoms are leaving the lattice of the consumed grain and joining that of the growing grain. These layers are added parallel to the (111) plane in the sequence ABCABC for an FCC crystal. A twin will occur if an anomaly occurs in this layering sequence. If this sequence becomes altered to CBACBA, the crystal so formed will still be FCC, but will be twinned in respect to the former crystal. If a similar occurrence takes place at a later stage, a crystal with the original orientation will start growing, thus forming a twin band. This change of sequence to form a twin band is shown in figure 3.8.

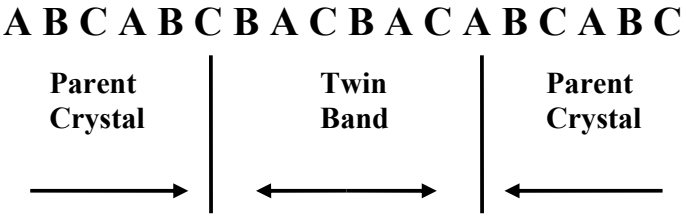

Figure 3.8: Layer sequence change in a twin band.

Figure 3.9 shows the structure of such a twin band. The plane of the drawing is the $(1\bar{1}0)$ plane with the (111) twin plane perpendicular to this plane, and the [111] twin axis lying in this plane. Open dots represent atoms in the plane while closed dots represent atoms in the layers immediately above or below. The reflection symmetry is shown with the dashed lines.

There is another possible way to describe the orientation relationship between a FCC crystal and its twin: the (111) layers of the twin are in a direction which would result from a homogeneous shear in a $[11\bar{2}]$ direction. This is also shown in figure 3.9. It is indicated by arrows going from initial positions D, E, F to final positions in the twin.

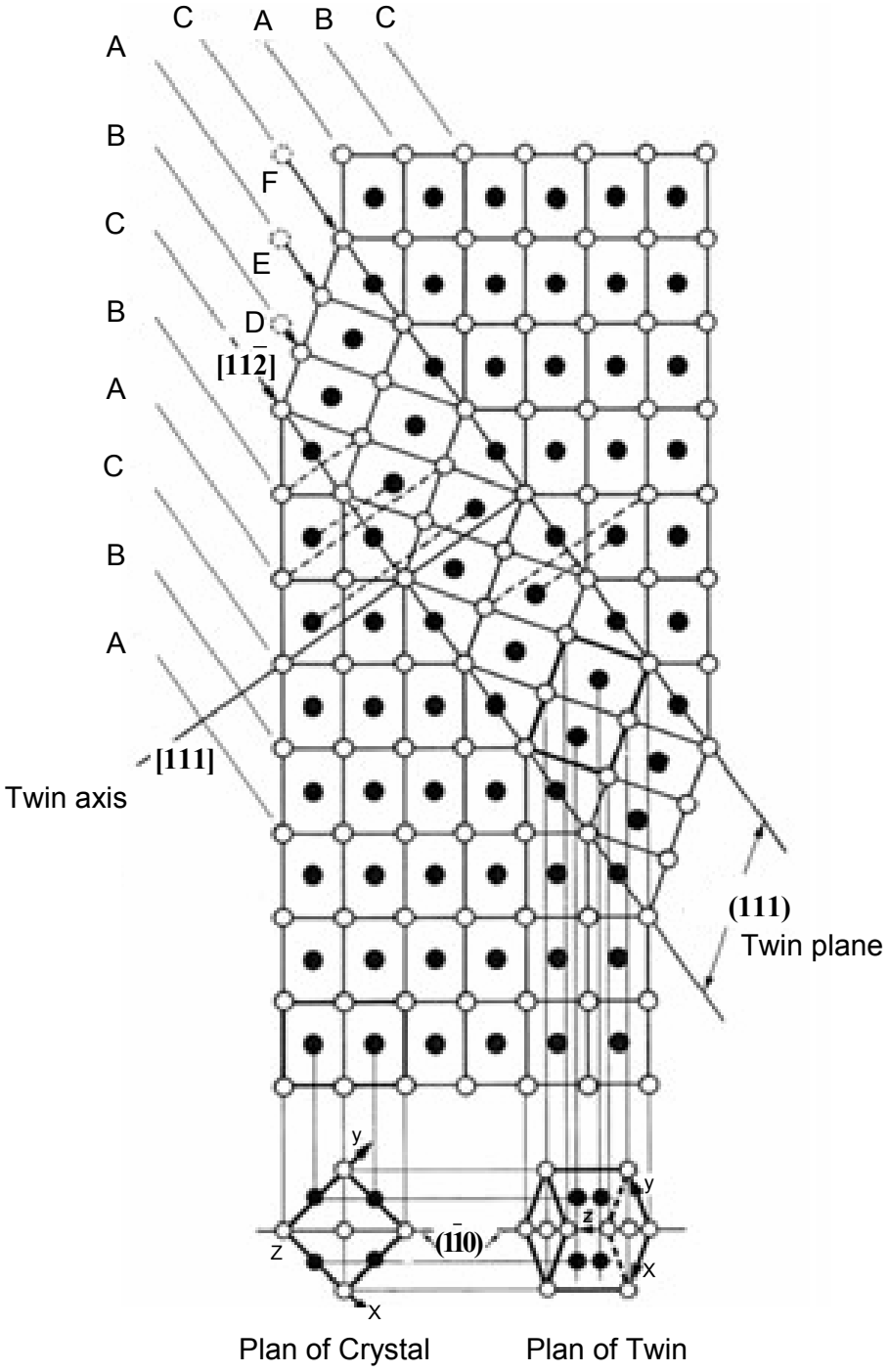

Figure 3.9: Structure of a twin band (Cullity, 1978, p61).

Twins formed due to deformation are commonly found in BCC and HCP lattices. In both cases the orientation relationship between parent crystal and twin is that of reflection across a plane. As a material with a HCP crystal structure is not investigated during this study, attention will only be given to BCC twins. In BCC structures, the twin plane is (112) and the twinning shear is in the direction **[11$\bar{1}$]**.

Twins in general can form on different planes in the same crystal. Taking recrystallised copper as an example, it is not unreasonable to expect to see twin bands running in different directions in the same grain. This is due to the fact that a FCC lattice has four {111} planes of different orientation on which twinning takes place. Repeated twinning may also occur in a crystal, some of which will form entirely new orientations. If for instance crystal A twins to form crystal B, which twins to form crystal C, then B and C are said to be first- and second order twins of A. This repeated twinning does not necessarily have to lead to new orientations. In Fig 3.7(b), A2 is a second order twin of A1 even though they both have the same orientation.

It should be noted that surface energies can give an indication of the ability of a surface defect to interfere with the slip process. As grain boundaries have high surface energies, they are much more effective to interfere with the slip process than either stacking faults or twin boundaries (Askeland, 1998, p101). Table 3.1 shows the surface energies for various surface defects in copper.

Table 3.1: Energies of surface defects in copper. (Adapted from Askeland, 1998, p102)

Surface imperfection in copper	**Energy** ($mJ.m^{-2}$)
Stacking fault	75
Twin boundary	45
Grain boundary	645

3.1.4 Control of grain size

Due to the important role grain size plays in the behaviour of metals, especially with regard to ductile behaviour, it is preferable to be able to control this property. Grain size is an important consideration in this study (see section 2.2.2) and will be varied by means of annealing. Annealing is a heat treatment designed to eliminate strain hardening that has occurred during any forging process – in the case of this study, the manufacturing process used to produce the shaped charge liner. According to Askeland (1998, pp202, 203), annealing takes place in three steps (see figure 3.10):

- The forged piece contains deformed grains and a large density of tangled dislocations. When the piece is initially heated, the additional thermal energy allows dislocations to move, and form a polygonised subgrain structure. Such a subgrain structure was reported by Gurevitch et al., (1992) in extruded OFHC copper (figure 3.11). This indicates that recovery occurred during the sample preparation process. The dislocation density however remains the same. This is called recovery or a stress relief anneal.

- When a critical recrystallisation temperature for each material is reached (200˚C for copper and 900˚C for molybdenum) recrystallisation can occur by the nucleation and growth of new grains. Rapid recovery takes place. Residual stresses are eliminated, and a polygonised dislocation structure is formed. Small grains then nucleate at the cell boundaries of the polygonised structure. In this process most of the dislocations are eliminated.

- If annealing takes place at temperatures higher than the recrystallisation temperature of the material, both recovery and recrystallisation occurs rapidly. The grains begin to grow, with some grains consuming smaller grains.

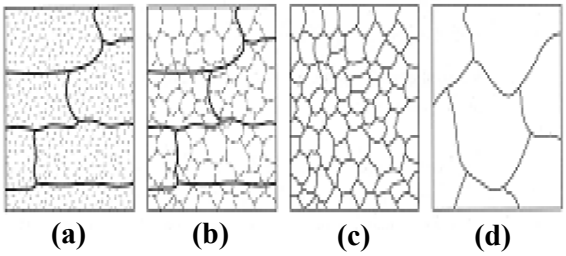

Figure 3.10: Microstructure: **(a)** after cold working, **(b)** after recovery, **(c)** after recrystallisation and **(d)** after grain growth (Askeland, 1998, p203).

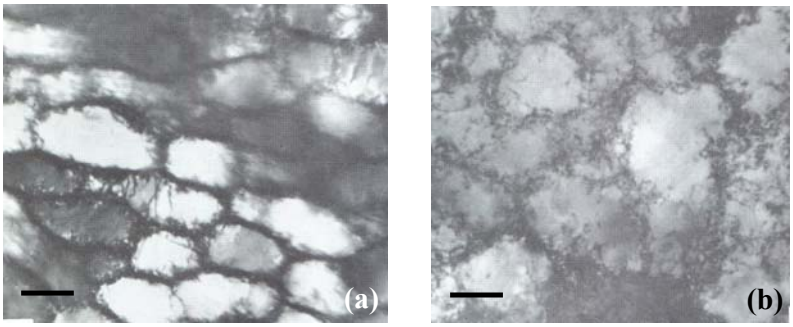

Figure 3.11: (a, b) Subgrain structures in copper as reported by Gurevitch *et al.* (1992). Scale bar indicates 200 nm.

3.2 Low strain rate plastic deformation of metals

3.2.1. The Tensile Test and Stress – Strain Diagram

The resistance of a material to a static or slowly applied force, in other words an attempt to deform the material at a low strain rate, can be measured by means of the tensile test. Figure 3.12 shows the basic experimental setup for performing the tensile test.

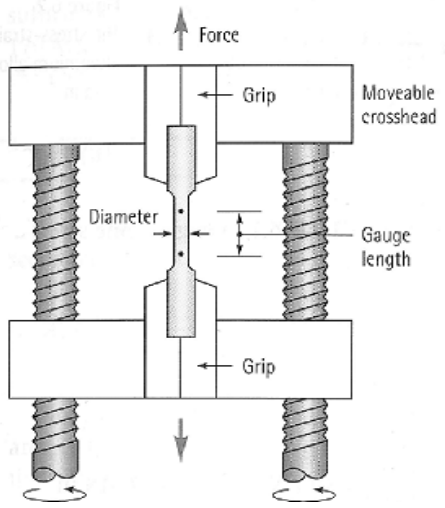

Figure 3.12: Experimental setup for the tensile test (Askeland, 1998, p141).

The tensile test is described by Askeland (1998, pp140, 141) as follows: A specimen is placed in the apparatus, and a load or force F is applied to the specimen. This force causes the specimen to stretch. The amount of stretch is measured by means of a strain gauge or extensiometer. The result is highly dependent on the size and shape of material used, but can be normalised to apply for all sizes and shapes of a single material if the force applied to the specimen is converted to stress, and the elongation length is converted to strain. Engineering stress σ and engineering strain ε are defined as follows:

$$\sigma = \frac{F}{A_0} \tag{3.2}$$

$$\varepsilon = \frac{l - l_0}{l_0} \tag{3.3}$$

In these equations A_0 is the original cross-sectional area of the specimen, l_0 is the original gauge length, and l is the gauge length after the force F was applied. The results of the tensile test are then recorded by means of the stress-strain curve as shown in figure 3.13.

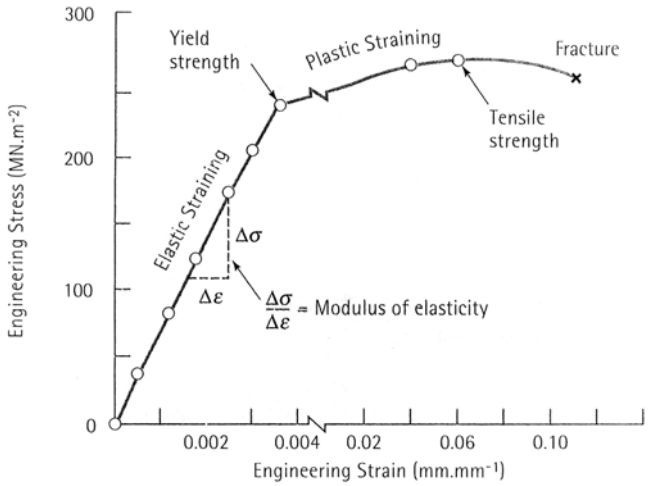

Figure 3.13: Stress-strain curve of an aluminium alloy (Askeland, 1998, p142).

Starting at a low stress and strain it follows from the stress-strain curve that the material will undergo temporary elastic deformation – the material returning to its original shape when the force is removed. The slope of the stress-strain curve in this region is known as the modus of elasticity of the material. This elastic straining of the sample does not occur indefinitely for the sample. At some critical point (called the yield strength of the material), the stress and strain is of such a magnitude that the sample is permanently deformed, even after the load is removed. This is known as plastic deformation. In many ductile materials, deformation does not remain uniform. It is possible that one region deforms more than other regions, and the result is a decrease in local cross sectional area. This so-called neck that forms requires a lower force to continue its deformation, and subsequently the engineering stress calculated in equation 3.2 from the original A_0 decreases. The tensile strength is the strength at which necking begins in ductile materials, and corresponds to the maximum stress in the stress-strain curve.

It should be noted that tensile properties are temperature dependent. Generally yield strength, tensile strength and modulus of elasticity decrease at higher temperatures, whereas ductility commonly increases (Askeland, 1998, p149).

3.3 Literature results for plastically deformed copper

3.3.1 Introduction

As mentioned in Chapter 1, copper is one of the most commonly used materials for the manufacturing of shaped charge liners. It is therefore not surprising that the majority of research done on materials undergoing high strain rate deformation has been done on copper. Although progress has been made in understanding the processes that drive copper jet formation and jet break up, no definitive conclusion can yet be made. Some observations that have been made are discussed below.

3.3.2 Effect of grain size on high strain rate deformation of copper

It is well known that the grain size of unfired shaped charges liners plays a significant role in jet performance (see section 2.2.2). This has been well documented by among others Doig (2002, p55) and Meyers *et al.,* (1995).

However, this was not found to be the case by Schmidt *et al.* (1991), who performed experiments to observe the deformation of copper at high strain rates and to relate differences in grain size to differences in deformation behaviour. From his study it was concluded that the stress-strain behaviour of copper at high strain rates (10^4 to 10^5 s^{-1}), as determined from a rod impact test, was not affected significantly by variations in grain size. Specimen profiles for the coarse (54 μm) grained and fine (16 μm) grained samples did not exhibit substantial differences in the stress-strain curves. The intermediate (29 μm) grained sample did exhibit a lower flow stress[1] for strains above 0.5. However this sample was impacted at a greater velocity than the fine and coarse grained samples. The size of surface irregularities on the deformed copper specimens decreased with decreasing grain size. In general, the stress-strain behaviour at high shear strain rates (1200-9000 s^{-1}), as measured from the torsional Hopkinson bar test, was not affected by grain size for shear strains below about 0.7. However above shear

[1]The shear stress required to cause plastic deformation of solid metals.

strains of 0.7, coarse-grained material exhibited less ductility than fine-grained material. Schmidt *et al.* (1991) concluded from the torsional Hopkinson bar test that a coarse grain size promotes unstable deformation in thin sections of copper. Deformation of coarse-grained copper (54 μm) produced large surface irregularities (~100 μm) that represents substantial variations in the cross sections of a thin segment (0.5 -1 mm thick) of the material. The large variations in cross section, in turn, promote unstable deformation. It was concluded that grain size had only a small influence on the high strain rate stress-strain behaviour of copper.

Gourdin *et al.* (1992) quoted a Ballistics Research Laboratory report stating that a decrease in the average liner grain size from 120 μm to 20 μm produces an increase of 25 % penetration in rolled homogeneous armour for five standoff distances and also includes figure 3.14, showing the increase of penetration for liners with small grain sizes. The smaller grains sizes were obtained by annealing at lower (< 400°C) temperatures.

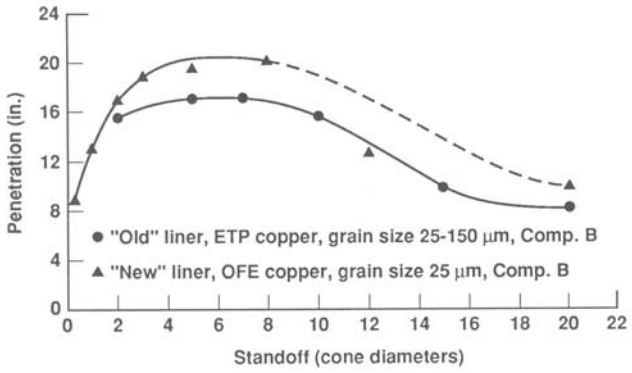

Figure 3.14: Effect of grain size on penetration (Gourdin *et al.,* 1992a).

In a second report, Gourdin *et al.* (1992b) showed that the break up time of electromagnetically expanded rings cut from copper liner material increased with decreasing grain size (see figure 3.15).

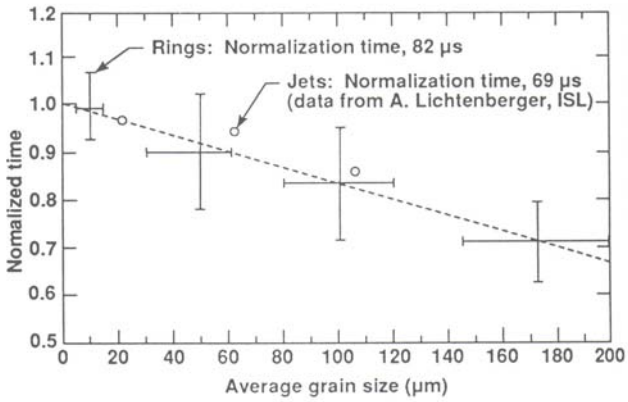

Figure 3.15: Break up times for jets and rings (Gourdin *et al.,* 1992b).

3.3.3 Dynamic recrystallisation

Various observations indicate that dynamic recrystallisation has taken place during copper jet formation, or copper sample deformation at high strain rates. The most common of these observations are a reduction in grain size between strained and unstrained copper.

Both Tian *et al.* (2003) and Gurevitch *et al.* (1993b) reported dynamic recrystallisation. Furthermore Tian *et al.* (2003) observed dislocation free zones in most areas of thin foil taken from recovered copper fragments (strain rate of 10^7 s^{-1}) in contrast to a high density of dislocations that were observed in samples taken from the liner that was plastically deformed at a strain rate of $4x10^4$ s^{-1}. Electron backscattered diffraction (EBSD) analyses revealed that the <110> fibrous microtexture that existed in these liners disappeared after straining, and was replaced by a random orientation of grains. According to the authors these results indicate that dynamic recovery and recrystallisation plays an important role in high strain rate deformation by virtue of a temperature increase during the deformation process.

Rapidly deformed copper which underwent dynamic recrystallisation generally shows a reduction in grain size between the original copper samples or liners and the strained samples or liners. One such study was done by Gurevitch *et al.* (1993a) on the

microstructure of copper liners before and after shaped charge detonation. It was observed that the grain size for the undetonated cones was reduced in the recovered copper jet fragments. This reduction was by a factor of 1.5. In the study the grain structure and grain substructures of drawn and annealed OFHC copper with a grain size of 35 μm were examined using optical and scanning electron microscopy, as well as transmission electron microscopy. There was no significant variation of the grain size of the recovered fragment except near the surface. It was expected by the authors to observe a central core of annular rings of microcrystalline grain size differences, but such an observation was not made. Similar results were obtained in a second study by Gurevitch *et al.* (1993b), but with a more significant grain size reduction, the average grain size being reduced from 45 μm to 15 μm.

No evidence of grain size reduction was found by Tian *et al.* (2003) in electroformed copper liners before and after plastic deformation at strain rate of $4x10^4$ s^{-1} as well as recovered jet fragments from detonated (strain rate of 10^7 s^{-1}) liners.

Although Krejci *et al.* (1995) reported a reduction in grain size, two additional observations were made that are not in full agreement with the conclusions drawn from the studies of Gurevitch (1993a,b) about solid slugs and jets undergoing dynamic recrystallisation. Firstly a serrated like appearance was noted on the slug surface. The authors noted that it was plausible to explain it as a consequence of shock waves arising from intensive deceleration when the slug came into contact with the steel target. However to obtain such structures on the surface, it must be assumed that the material was in a semi-solid state. The second feature that is contradictory to dynamic recrystallisation was the appearance of columnar crystals on the surface of an interior cavity of the slug. Columnar crystals, together with shrinkage defects, are typical of casting structures and can only grow from melted material. The authors concluded that the outer surface layer of the liner is in a liquid state during collapse. It is therefore possible that the jet could also be in a liquid, or semi-solid state. Note, however, that most of these results were obtained from the slug, and thus cannot automatically be accepted for the jet. Furthermore, if the slug was indeed in a semi-solid or liquid state at some time, this could have been caused by heating due to the kinetic energy of the slug being transformed to frictional heating on impact with the steel target. A soft recovery technique would have delivered more conclusive results.

Such a technique would eliminate any additional strain or excessive heating effects on the sample material which is caused by the severe deceleration experienced by the jets when impact with the target material occurs.

3.3.4 Deformation mechanisms

Gurevitch *et al.* (1993a) noted that a shaped charge liner undergoes three definite steps:

1. Precursor bar fabrication, prior to drawing and processing of the cone.
2. The drawing and processing of the cone.
3. The detonation of the cone to form a plastically extending and particulating jet.

Each step represents a unique deformation process characterized by different strain rate phenomena. The first two processes are characterized by quasi-static processes, while the detonation regime is characterized by dynamic processes due to the high strain rate deformation. Evidence exists for two main deformation mechanisms that play a role during high strain rate deformation. These processes, slip and twinning, can be seen as competitive mechanisms (Meyers *et al.*, 1995). Plastic flow will occur by the one that requires the lower stress. Tian *et al.* (2003) noted that deformation at normal strain rates is ascribed to conventional slip mechanisms.

As mentioned in section 3.1.3, the occurrence of twinning is an observation of great importance. Closely related to twinning, is the formation of microbands. According to Li *et al.* (2004) these microbands, which are similar to slip bands, were first thought by researchers to be deformed twins, but it was later found that they were formed by two high density dislocation walls. It has been shown that the formation of micro bands and twins are dependent on the geometry of the applied shock wave. By applying a planar shock wave, twins were generated, while under spherical shock waves microbands are most prevalent. It has also been noted that the grain size was an important factor in the formation of microbands. The grain size must be above a critical value for microbands to form, and above this value their density increased

with grain size. It has also been shown that the number of twins increased with a decrease in stacking fault energy of various metals.

Twinning was observed by Meyers *et al.* (1995). Samples of Oxygen Free High Conductivity (OFHC) copper with average grain sizes of 9.5 μm, 25 μm, 117 μm and 315 μm were subjected to high strain rate plastic deformation in which high shear strains of approximately 2 to 7 were produced. The copper plate samples were shock hardened by planar impact using an explosively accelerated flyer plate resulting in a pressure of approximately 50 GPa with an initial pulse duration of 2 μs. Quasistatic compression tests were conducted in the strain rate range of 10^{-4} s^{-1} to 10^{-1} s^{-1} at room temperature. High strain rate tests were conducted in a split Hopkinson bar. While twinning was observed for the larger grain sizes in the samples that underwent shock loading at a shock pressure of 50 GPa, twinning was virtually absent in the smallest grain size specimen shocked at the same pressure. It was concluded that the differences in response due to grain size are the result of differences in microstructural changes affected by shock loading. Plastic deformation was localized in the coarse grain specimen, while deformation was homogeneous in the smallest grain size sample. A rationale was proposed to explain the above observations of the slip-twinning transition based on the intersection of plots in the Hall-Petch diagram for these two competing plastic deformation processes. An example of such a diagram is shown in figure 3.16. At constant strain rate and temperature, this transition will take place when a certain critical grain size is reached. It is suggested that the grain size dependence of shock response can significantly affect the performance of shaped charges, with smaller grain size material undergoing more hardening than larger grain size material, and that liner performance will be enhanced by a fine grain size liner material.

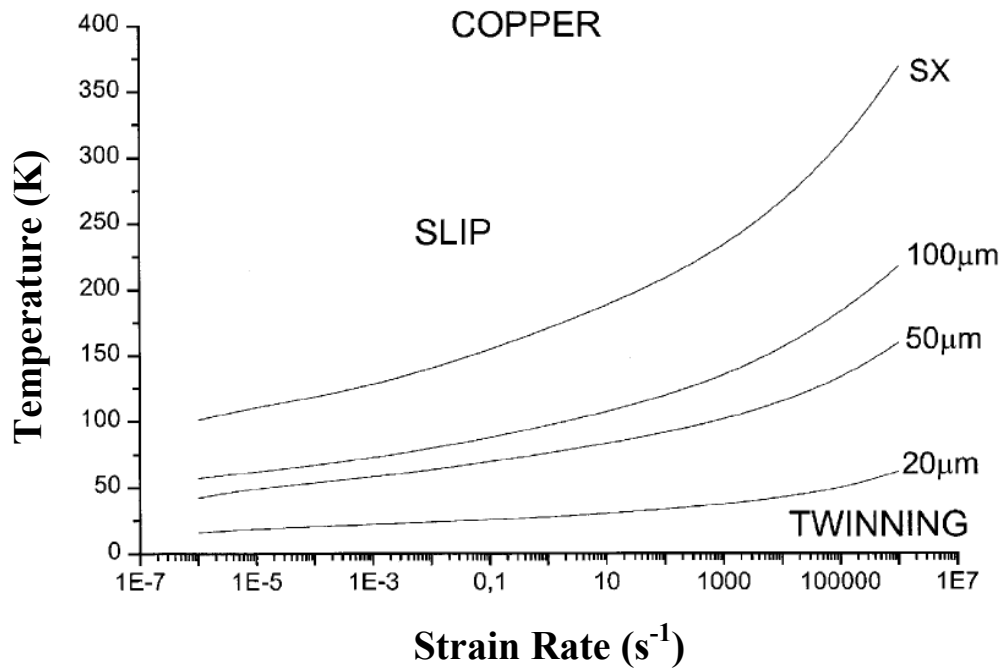

Figure 3.16: Model of Meyers *et al*. (2001) for the slip-twinning threshold in copper. (SX means single crystalline).

Li *et al.* (2004) studied deformed microstructures near the impact crater in annealed and cold rolled pure copper targets struck by steel balls with a speed of 1.5 km/s which produced spherical shock waves. It was found in both targets that the dominant microstructure was very fine microbands, and no twinning was observed. Microbands were coincident with traces of the (111) slip planes.

Twins were also observed in recovered jet fragments by Krejci *et al.* (1995).

3.3.5 Voids

As mentioned in section 2.3.2., the formation of voids may play an important role in both the jet formation as well as instabilities leading to jet break up and fragmentation. In a study performed by Gurevitch *et al.* (1993a) SEM was used to show that the recovered jet fragment tips exhibited voids and coalesced void tunnels, which are believed to have developed during jet elongation by diffusion and growth at high strain rate. Additional porosity in the interior of the jet fragments was also observed by Gurevitch *et al.* (1993b). Similar results were obtained by Tian *et al.* (2003). A wide range of crystal defects occurred in recovered copper jet fragments. These defects included vacancy clusters and porosity. It has been shown that shocked ductile materials develop cracks by nucleation, growth and linking up of microscopic voids. Impurities and inclusions can act as void nucleation sites (Heller, 2002).

3.3.6 Impurities

As suggested in section 2.3.3, the role of impurities might be more important than grain size or microstructure, as some significant differences were observed between OFHC copper jet microstructure and electrolytic tough pitch (ETP) copper jet microstructure by Gurevitch *et al.* (1993a). Unlike grain size and other microstructure, which are easily altered during plastic deformation, impurities can be carried along in the deformation process, and they can directly and continually influence the process, including the stability of the elongating jet. Gurevitch *et al.* (1993a) also stated that oxide inclusions in especially ETP copper would contribute to void formation.

Schwartz *et al.* (1998) suggested that the break up time of jets is fundamentally related to the grain boundary impurity concentration. The combined effect of impurity concentration and grain size was determined, by assuming that all impurity atoms diffuse along, and remain at, the grain boundaries. A geometrical analysis based on an assumed tetrakaidecahedron grain shape was applied to determine the relationship between grain size, impurity content, and break up time in sulphur doped OFHC copper. The number of impurity atoms as a function of grain size, the number of

available sites at crystalline defects, and the intercrystalline impurity concentration was calculated. It was observed that the break up time of copper shaped charge liners doped with sulphur decreased as the grain boundary impurity content increased (see figure 3.17), which suggests that grain boundary impurity content is a reliable predictor of shaped charge jet ductility. It was suggested that the segregation of impurities at certain boundaries compared to a uniform distribution, and the type of dislocations forming the grain boundaries, might also play an important role.

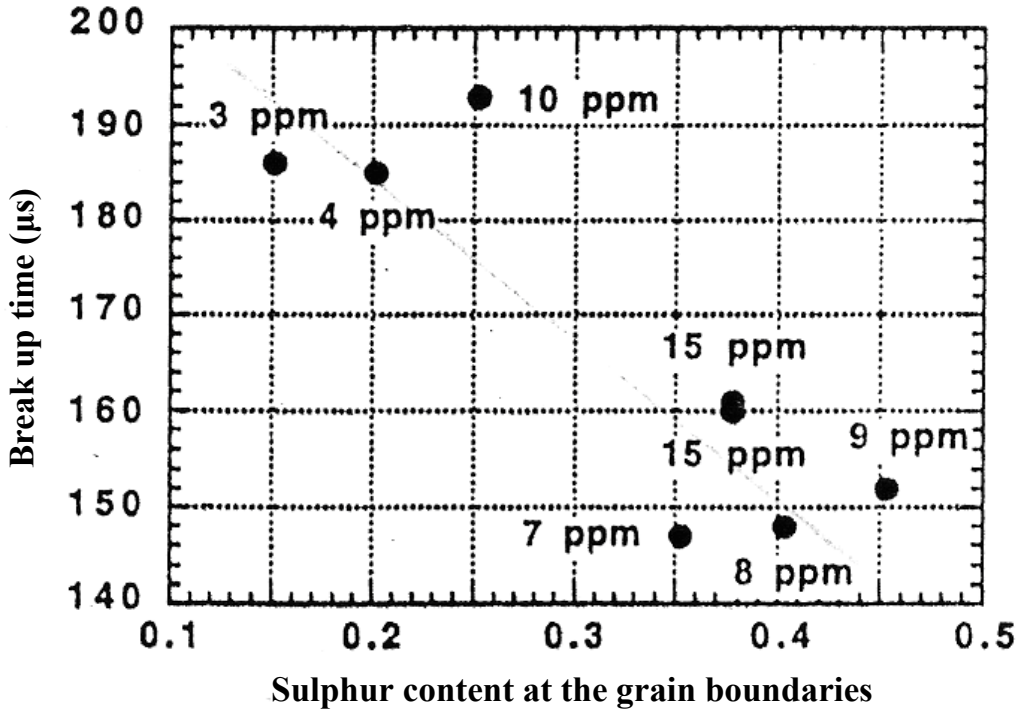

Figure 3.17: Jet break up time as a function of sulphur content at grain boundaries (1.0 on X axis represents a full monolayer of sulphur coverage of a grain) (Schwartz *et al.,* 1998).

3.4 Literature results for plastically deformed molybdenum

Molybdenum is an attractive material for shaped charge liners due to a high bulk sound speed (5124 $m.s^{-1}$) and a relatively high density (10.22 $Mg.m^{-3}$). As mentioned in section 2.2.1, this high density leads to improved penetration due to better momentum characteristics. The high bulk sound speed is desirable in order to achieve high velocity coherent jet tips (Baker *et al.,* 1993). Although some previous research has been done on molybdenum liners, especially regarding manufacturing processes, few studies have been done regarding the microstructural evolution of this material during jet formation and jet break up. Most research conducted on BCC metals focused on tantalum (which will be discussed in section 3.5).

Research by Lightenberger *et al.* (1996) gives results concerning the basic metallurgical and mechanical properties of molybdenum used in liners. It was noted that the grain size is usually between 15 μm and 100 μm, and that grains are oriented parallel to the liner axis. Chemical analysis has also shown that sulphur and oxygen induce brittleness. This is of great concern in the manufacturing of molybdenum liners, because sintered products are generally not very good in terms of reproducibility with regards to microstructure and purity. Samples were tested in compression, and these results were used to construct figure 3.18, which shows the influence of strain rate on the flow stress for a sintered molybdenum product.

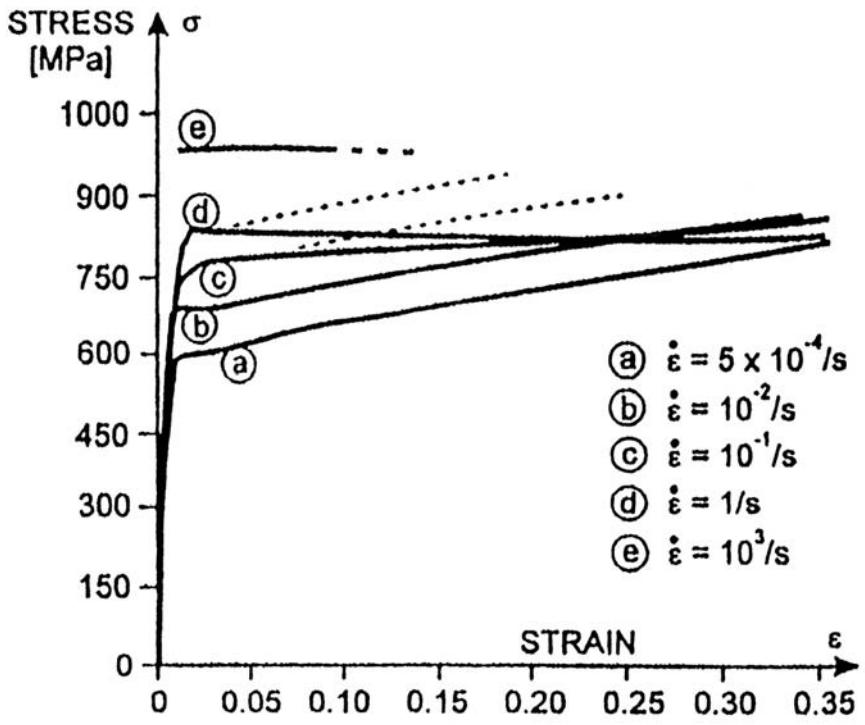

Figure 3.18: Stress-strain curves for molybdenum at different strain rates ($\dot{\varepsilon}$) (Lightenberger *et al.,* 1996).

The flow stress could be related to the strain rate by

$$\sigma = \alpha + \beta \log \dot{\varepsilon} \qquad \textbf{(3.4)}$$

with α = 870 MPa and β = 127 MPa.

The results of toughness tests are shown in figure 3.19.

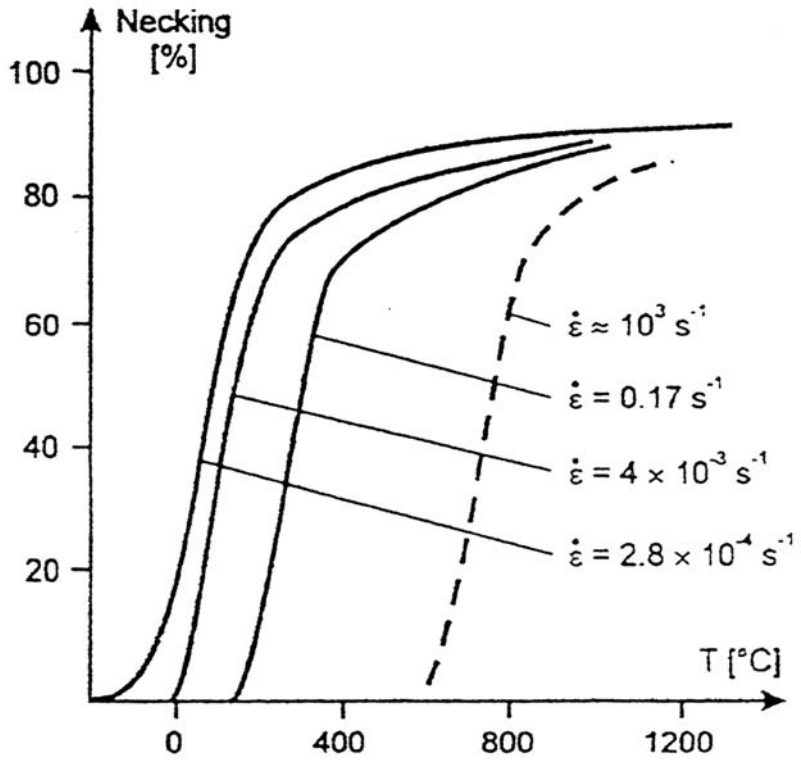

Figure 3.19: Ductile-Brittle transition of Mo (Lightenberger *et al.,* 1996).

It was concluded that the best liner performance will be obtained with sintered products with a fine grain size, and that temperature plays the most important role in the ductility of a jet.

During this literature study, no Transmission Electron Microscopy (TEM) results concerning molybdenum liners were found.

3.5 Literature results for plastically deformed tantalum

Nemat-Nasser *et al.* (1998) subjected polycrystalline tantalum to high plastic shear strains at strain rates exceeding $5x10^{4}\ s^{-1}$. Samples were tested at room temperature and 600˚C under both adiabatic and quasi-isothermal conditions. The quasi-isothermal conditions were created by conducting incremental tests and allowing the specimen to

return to its original temperature before conducting the next strain increment. Slip of perfect screw dislocations, on the {110}–type planes along the <111> directions was found to be the dominant deformation mechanism. The substructures of adiabatically tested samples included dislocation arrays, grouped dislocations, elongated dislocation cells, sub-grains and recrystallised sub-micron sized grains (0.15 μm). In contrast, isothermally tested specimens featured higher dislocation densities and inhomogeneous dislocation distributions. In both cases small dislocation loops were observed in the shearbands. It was observed that the plastic deformation was highly concentrated, which produced a narrow shear localized region across the specimen. Although no deformation homogeneity was observed at a shear strains of up to 3.4, deformation homogeneity was found within the shearbands of specimens deformed to a shear strain of 9.1.

As mentioned in section 3.1.3, twinning and slip are competing mechanisms of deformation. This is especially true in the case of BCC metals where the yield stress is highly temperature dependent.

In a study by Murr *et al.* (1997) tantalum samples with an average grain size of 43 μm were shock loaded using an accelerated flyer plate which produced a peak shock pressure of 45 GPa at a pulse duration of 1.8 μs. This deformation produced twinning. The authors proposed a model that predicts the threshold shock stress for twinning in tantalum. This model is an extension of initial considerations of Meyers *et al.* (1995). A very low temperature and strain rate dependence of the twinning stress is assumed, and the model includes grain size effects. The model does not take shock heating into account. At a critical strain rate, the flow curves for slip and twinning intersect indicating the start of the slip/twinning transition. The model yields quantitative predictions of the threshold stress for twinning in tantalum that corresponds with experimental results. The predictions of the model concerning the stress as a function of grain size are shown in figure 3.20.

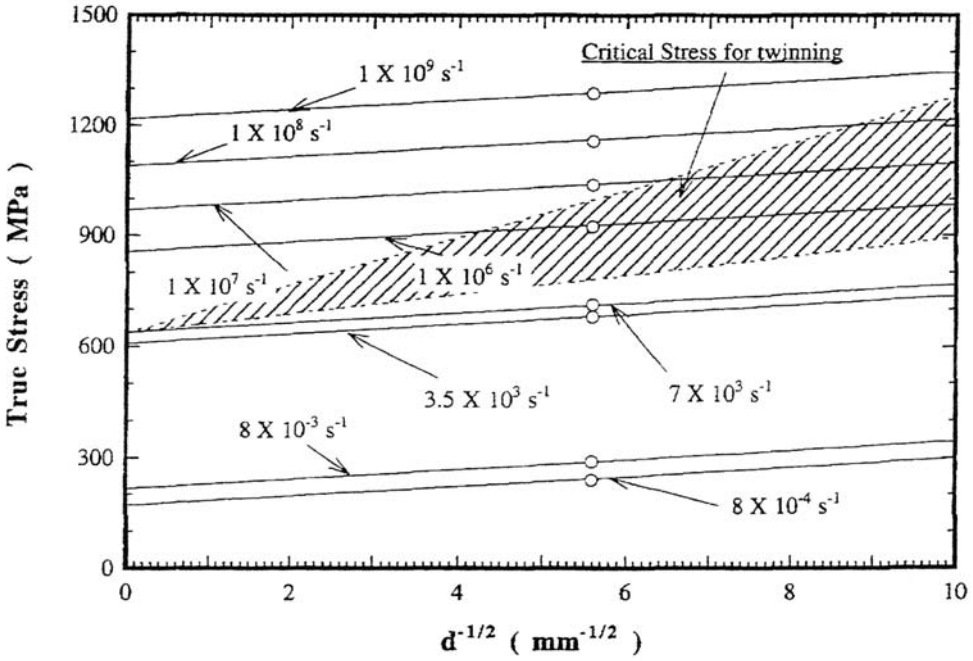

Figure 3.20: Hall-Petch relation for slip and twinning for tantalum (hatched area represents uncertainty) (Murr *et al.,* 1997).

Nemat-Nasser *et al*. (1998) found the dominant deformation mechanism in tantalum strained at $5x10^4$ s^{-1} to be slip of screw dislocations on the {110} planes, with elongated dislocation cells with a small misorientation being the most predominant microstructural characteristic of the shear localization region. These dislocation cells became smaller with an increase in shear strain. Interestingly, no evidence of deformation induced twinning was observed.

3.6 Summary

Dislocations are line imperfections in an otherwise perfect lattice. They are formed in materials during solidification or when the material has been deformed. Two basic types of dislocations, namely screw and edge dislocations, can be identified. This process by which a dislocation moves and causes a material to deform is called slip. Slip is not the only deformation mechanism. A second possibility is that of deformation twinning. Twinned crystals consist of two parts symmetrically related to

one another. It should be noted that all twinning is not necessary due to deformation twinning, but that annealing twins also exist. These twins are particularly prevalent in annealed FCC materials. These two deformation mechanisms are competing, indicating that a slip-twin transition will occur. Although some models predict this transition, no clear agreement has been reached by researchers.

Properties of materials are strongly influenced by the size and number of grains they contain. A dislocation can only move until it encounters a grain boundary. It follows then that an increase in grain boundaries will have a strengthening effect on the material. This can be achieved by increasing the number of grains, and hence decreasing the grain size. Although smaller grain sizes generally correspond to a decrease in ductility, many researchers have reported an increase in jet break up time with a decrease in grain size. Nevertheless, this result is not uncontested. Some researchers do, however, present evidence of a decrease in the grain size of recovered copper jet fragments compared to the original liner material, and attribute this to dynamic recrystallisation of the jet as it elongates.

Impurities seem to also play a role in the performance of both copper and molybdenum shaped charges. While these impurities usually cause embrittlement, it could also serve as nucleation sites for the formation of voids, which can further lead to jet break up.

3.7 References

Askeland D.R. **[1998]** *The Science and Engineering of Materials*, Stanley Thornes Ltd.

Baker E.L, Voorhis G.P., Campbell R. and Choi C.S. **[1993]** *14th International Symposium on Ballistics*, Quebec, Canada. P137

Barret C. and Massalski T.B.. **[1980]** *Structure of Metals*, Pergamon Press.

Cottrell A.H. **[1956]** *Dislocations and Plastic Flow in Crystals*, Oxford University Press.

Cullity B.D **[1978]** *Elements of X-Ray Diffraction,* Addison-Wesley Publishing Company.

Doig A. **[2002]** *Military Metallurgy*, Maney Publishing.

Gourdin W.H. **[1992a]** *Characterization of Copper Shaped-Charge Liner Materials at Tensile Strain Rates of $10^4 s^{-1}$* in *Shock-Wave And High–Strain-Rate Phenomena In Materials* (Meyers M.A., Murr L.E. and StaudHammer K.P.), Marcel Dekker Inc.

Gourdin W.H. **[1992b]** *Correlation Between the Ultimate Elongations of Rapidly Expanding Rings and Stretching Metal Jets* in *Shock-Wave And High–Strain-Rate Phenomena In Materials* (Meyers M.A., Murr L.E. and StaudHammer K.P.), Marcel Dekker Inc.

Gurevitch A.C., Murr L.E., Shih H.K., Niou C-S., Advani A.H., Manuel D. and Zernow L. **[1993a]** *Materials Characterization* **30** p201

Gurevitch A.C., Murr L.E., Fisher W.W., Varma S.K and Advani A.H. **[1993b]** *Journal of Material Science* **28** p2795

Heller A. **[2002]** *Science and Technology Review, July/August,* p13

Li G.A., Zhen L., Li H.T., Tan X **[2004]** *Materials, Science and Engineering* **A384(12-18)** p12

Lichtenberger A., Verstraete N., Salignon D., Daumas M.T. and Collard J. **[1996]** *16th International Symposium on Ballistics*, San Francisco, USA. p49

Krejci J., Brezina J. and Buchar J. **[1995]** *15th International Symposium on Ballistics*, Jerusalem, Israel. p49

Meyers M.A., Andrade U.R. and Chokshi A.H. **[1995]** *Metallurgical and Materials transactions* **26A** p2881

Meyers M.A., Vöhringer O. and Lubarda V.A. **[2001]** *Acta Materialia* **49** p4025.

Murr L.E., Meyers M.A., Niou C-S., Chen Y.J., Pappu S. and Kennedy C. **[1997]** *Acta mater*. **45(1)** p157

Nemat-Nasser S., Isaacs J.B. and Liu M. **[1998]** *Acta mater.* **46(4)** p1307

Schmidt C.G. Caligiuri R.D., Giovanola J.H. and Erlich D.C. **[1991]** *Metallurgical Transactions* **22A** p2349

Schwartz, A.J., Lassila D.H. and Baker E.L **[1998]** *17th International Symposium on Ballistics*, Midrand, South Africa. p439

Tian W.H., Fan A.L., Gao H.Y., Luo J. and Wang Z. **[2003]** *Materials, Science and Engineering* **A350(1-2)** p160

Walters W.P., Zukas J.A. **[1998]** *Fundamentals of Shaped Charges*, CMCPress.

Chapter 4

An overview of experimental techniques

4.1 Introduction

The project outline and research objectives were briefly discussed in Chapter 1. The following experimental stages were used to meet these objectives.

- Sample extraction by means of Electric Discharge Machining (EDM), also commonly known as spark erosion.

- Annealing of the samples at different temperatures and times to obtain different microstructures.

- Straining of the samples at different strain rates by means of the Split Hopkinson Pressure Bar.

- Determining the grain size of each sample. This includes polishing of the samples, etching of the samples, and investigation of the grain structure using a Scanning Electron Microscope (SEM). Use can also be made of supporting techniques i.e. Optical Microscopy and Atomic Force Microscopy (AFM).

- Investigation of the microstructure using a Transmission Electron Microscope (TEM).

- Chemical analysis of the samples to determine the elemental make-up of the bulk material used by Denel Land Systems in the manufacturing of shaped charge liners.

To be able to make comparisons between samples with different microstructures and that were deformed at different strain rates it was decided to construct a sample matrix for each material (copper with a FCC crystal structure and molybdenum with a BCC crystal structure) as shown in table 4.1.

Table 4.1: Sample matrix for samples used during study.

	T0	**T1**	**T2**
S0	A B C	A B C	A B C
S1	A B C	A B C	A B C
S2	A B C	A B C	A B C

T0 and S0 denote samples that were unannealed and unstrained, respectively. T1 denote an annealing condition, T2 being a higher temperature anneal than T1, or the same temperature, but having a longer annealing time. S1 indicates that a sample was deformed at the lower value of the two strain rates used. S2 being a higher strain rate than S1. Thus as an example, T0S2 would denote a sample that was left unannealed, but was deformed at the highest strain rate. This then gives nine different types of samples for each material. Three samples of each type were prepared. One would be used as a TEM sample, one would be used to determine the grain size and grain structure of that specific type of sample, and one sample would be kept as a backup. This meant that 27 samples of each material had to be extracted, for a total of 54 samples.

The following sections give a description of the primary techniques used during this study, and also discusses the experimental procedures used, and the results obtained during sample extraction and annealing.

4.2 Spark erosion

Extracting samples from the shaped charge liners provided proved to be challenging and extremely time consuming. A technique had to be found that minimized any deformation of the sample, as well as any heating effects. This had to be done to

ensure that the microstructure of the sample was not altered in any way. These restrictions excluded the use of lathe turning and laser cutting. It was decided that spark erosion would be used to cut the cylindrical samples with a diameter of approximately 5 mm from the liners. This technique was employed firstly since it minimizes microstructural damage to the sample, and secondly because it is the most commonly used technique in research conducted on shaped charges for the cutting of samples (Meyers *et al*., 1995).

The basic experimental setup for a spark erosion apparatus consists of a sample holder containing the sample that is at a zero potential, and an electrode that is connected to a DC source via capacitors (Viljoen *et al*., 1989). The process is then as follows:

- The sample and electrode are placed in a dielectric fluid.
- An electric field builds up. Since the dielectric fluid acts as an insulator no current flows until the gap between sample and electrode is decreased to a critical size - then discharge takes place.
- The current causes resistive heating of the discharge channel.
- When the flow of current is interrupted by limited capacitance, this discharge channel collapses.
- The molten metal on the surface of the material evaporates explosively.
- A small crater is formed.
- By moving the sample and electrode closer to each other the process repeats.

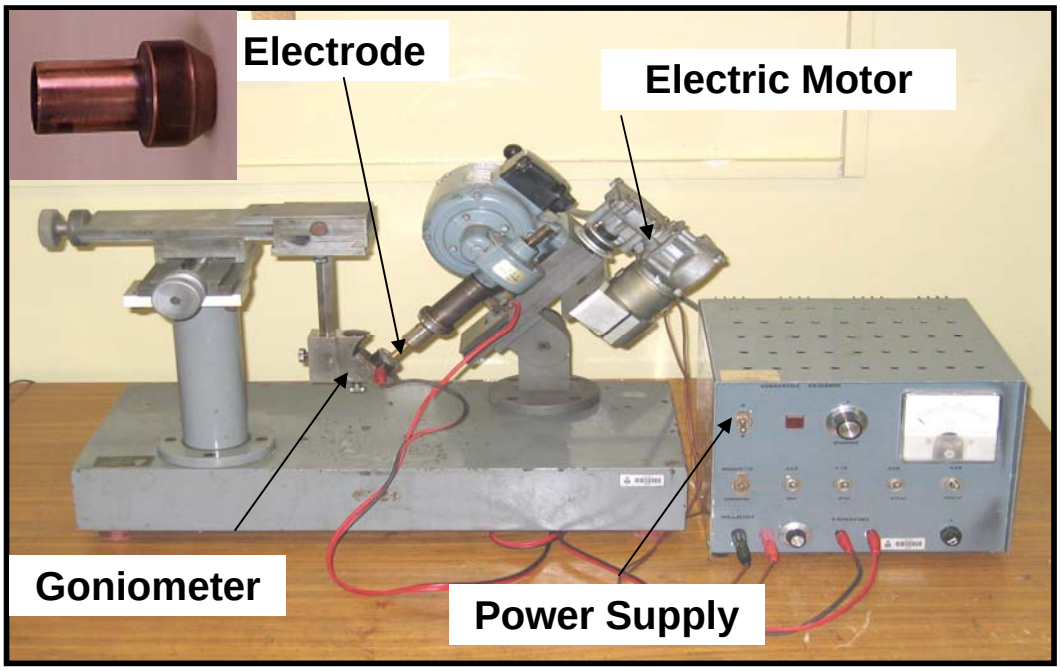

Figure 4.1: Spark erosion apparatus at the UFS. An example of a Cu/W electrode is shown in the top left corner.

A basic spark erosion apparatus had been constructed at the Department of Physics at the University of the Free State in the late 1970's. This apparatus is shown in figure 4.1. However, the apparatus had not been used for many years and an attempt was made to return it to service. The electronic control unit of the apparatus was altered to optimize the cutting rate of the apparatus. This included increasing the voltage of the power supply and adding various heat sinks to components for more efficient dispersion of heat inside the electronic system. The greatest challenge was choosing and acquiring an electrode material that delivered acceptable results in terms of cutting speed and electrode life. Consulting the documentation of the apparatus, as well as the persons involved with its construction, did not solve the problem. Even an industrial spark erosion technician in Bloemfontein could not offer any useful advice. Two scientific studies were done on electrode materials and electrode cutting rates.

The first of these employed density measurements and Auger Electron Spectroscopy (AES) measurements to determine the composition of an existing electrode. Energy Dispersive X-Ray Spectroscopy (EDS) would have been employed, but was not available on the Bloemfontein campus at that time. By

means of water displacement it was found that the density was 18±2 $Mg.m^{-3}$, which isolated Au, U, W or an alloy containing a refractory metal as candidates for the material. It was decided to employ the (AES) technique. The following settings were used:

- Base Pressure: 10^{-9} Torr.
- Electron beam energy: 3 keV.
- Analyser: Single pass cylindrical mirror analyzer.

The resultant Auger spectrum after argon ion sputtering of the sample surface to remove any contaminants is shown in figure 4.2.

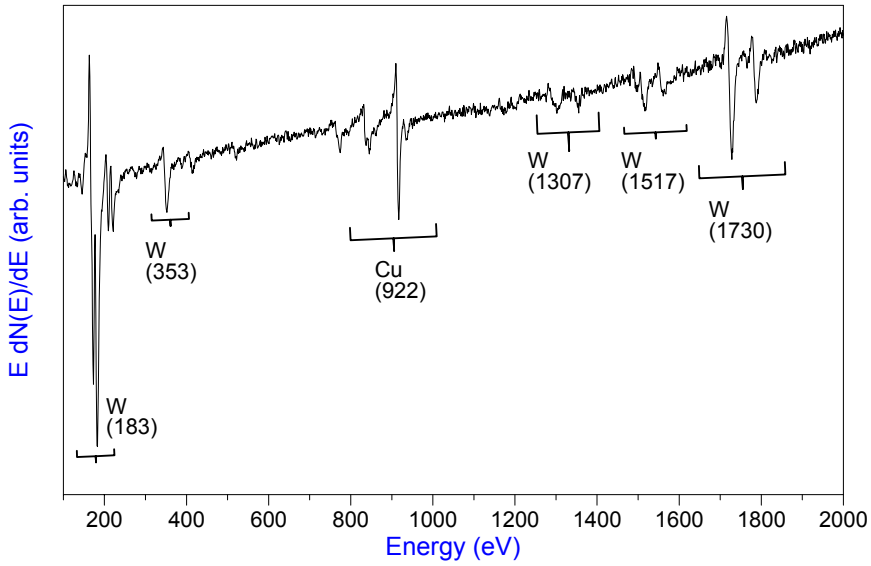

Figure 4.2: Auger spectrum of unknown electrode.

Consulting the Handbook of Auger Electron Spectroscopy (Hedberg, 1995, pp 96, 260, 261), the Auger peaks were found to correspond to those of copper and tungsten.

Using the equation

$$X_a = \frac{I_a / S_a}{\sum I_i / S_i} \qquad \textbf{(4.1)}$$

where X_a is the atomic % of element i, I_i is the Auger intensity of element i and S_i is the sensitivity of element i (Hedberg, 1995, p 17), it was found that the electrode contained 13 atomic % Cu and 87 atomic % W. Using these values it was possible to calculate the electrode density, which gave a value of 17.9 $Mg.m^{-3}$ Using the original density measurement of 18 $Mg.m^{-3}$, a composition of approximately 70% W and 30% Cu in atomic percentage were calculated. Both of these methods gave an indication that the electrode consisted of a copper - tungsten alloy, with tungsten forming the bulk of the compositional makeup. Although neither of these methods can be considered to be very accurate, both served the desired function.

The second study concentrated on the cutting rate of various electrode materials, namely copper and stainless steel, as well as their erosion resistance. Electrodes of various materials were used to cut commercial copper and stainless steel. After a cutting time of an hour the depth of the resulting cut as well as the decreased length of electrode remaining were measured, and from this the cutting rate and erosion rate were determined. The results for the cutting of copper are shown in table 4.2 while the results for the stainless steel are shown in table 4.3. Note that cutting was performed using both possible polarities. When the sample was at a zero potential and the cutting electrode at a positive potential, it is referred to as the normal polarity. In a reverse polarity setup the sample is at a zero potential and the electrode is at a positive potential.

Table 4.2: Cutting results of copper using various electrode materials.

Electrode material	**Normal polarity**		**Reverse Polarity**	
	Cutting rate ($mm.h^{-1}$)	**Erosion rate ($mm.h^{-1}$)**	**Cutting rate ($mm.h^{-1}$)**	**Erosion rate ($mm.h^{-1}$)**
Brass	0.0	25.3	0.6	11.4
Graphite	0.0	0.4	0.2	0.6
Cu/W	0.5	0.4	0.4	0.2
Cu	0.5	5.2	0.5	4.4
Stainless steel	0.9	6.0	0.6	11.4

Table 4.3: Cutting results of stainless steel using various electrode materials.

Electrode material	Normal polarity		Reverse Polarity	
	Cutting rate ($mm.h^{-1}$)	Erosion rate ($mm.h^{-1}$)	Cutting rate ($mm.h^{-1}$)	Erosion rate ($mm.h^{-1}$)
Brass	0.9	8.2	6.6	12.6
Graphite	0.4	0.1	5.8	1.4
Cu/W	1.6	0.0	0.5	0.1
Cu	3.5	0.5	1.8	2.8
Stainless steel	0.7	3.7	1.9	8.5

After considering the cutting rates achieved using the different electrode materials, in view of their respective erosion rates, it was found that a Cu/W alloy produced the best overall results as an electrode material. Quotes for this material were received from both the United States and Great Britain, since the material where unobtainable in South Africa. The material was then acquired from Central Metals and Alloys Ltd. in England. This material came in the form of five rods with a diameter of 15 mm and 200 mm long at a cost of £205.90. This alloy was the closest match (in terms of composition) to the original electrode that could be obtained, and consisted of 76% W and 24% Cu in atomic percentage. This composition was also recommended by the supplier of the bars. Lathe turning of the electrodes from these bars was performed by the Instrumentation division at the UFS. Even with all these improvements the cutting of the samples was a slow process. The average cutting time for a copper sample was approximately 8 hours, while a molybdenum sample could be produced in just over 40 hours. This time consuming process was aggravated by the tendency of the samples to pull skew just before the cut was completed. This caused the sample to be cut skew, which made it useless. This phenomenon is thought to be due to residual stresses in the material caused by the forging process of the liners. By adapting the sample holder of the spark erosion apparatus this problem was solved. This involved fixing the sample on a stub in such a way that the excess material pulled skew while the sample remained straight. The cutting of copper samples, as well as some molybdenum samples, was performed using the apparatus housed at the Physics department. The majority of the molybdenum samples were later sent to “TK

Manufacturing" for cutting. This is a firm located in Port Elizabeth, which specializes in wire spark erosion cutting. The procedure is the same as in the case of normal spark erosion cutting, except that a thin wire is used as an electrode. Better flushing of eroded material away from the sample (which is not possible in the UFS system) as well as the thin wire requiring less material to be eroded for a cut makes wire spark erosion a superior technique.

4.3 Annealing

As outlined in the project objectives, the stress-strain response of each material was tested with three different microstructures. To obtain these different microstructures, samples were either left unannealed, or annealed at two different temperatures and times. This would then result in recovery, recrystallisation and grain growth in the samples which then would produce different microstructures as explained in section 3.1.4.

The annealing system used is shown in figure 4.3, with a schematic diagram in figure 4.4.

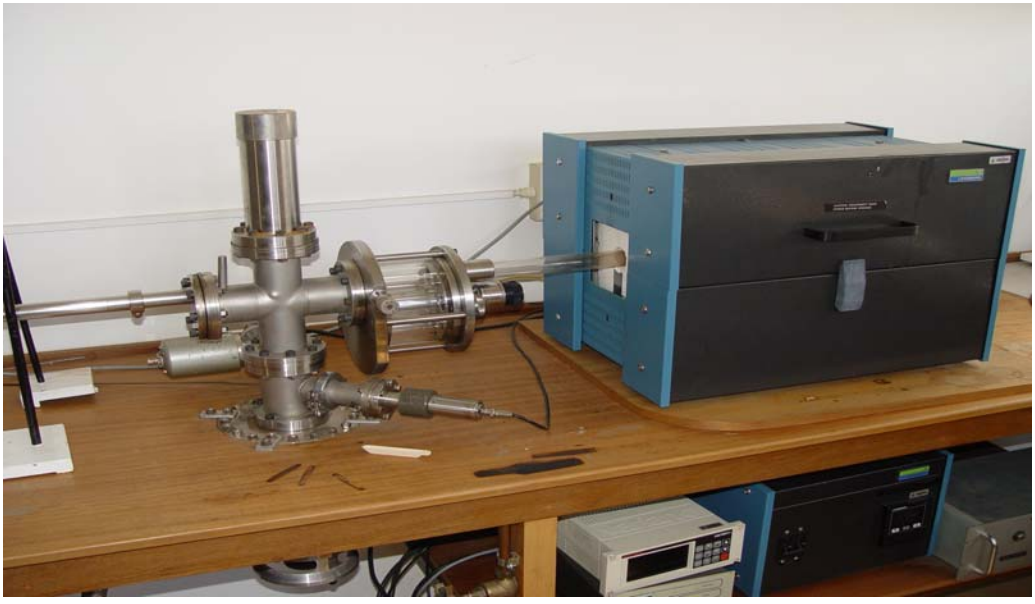

Figure 4.3: Annealing System at the UFS.

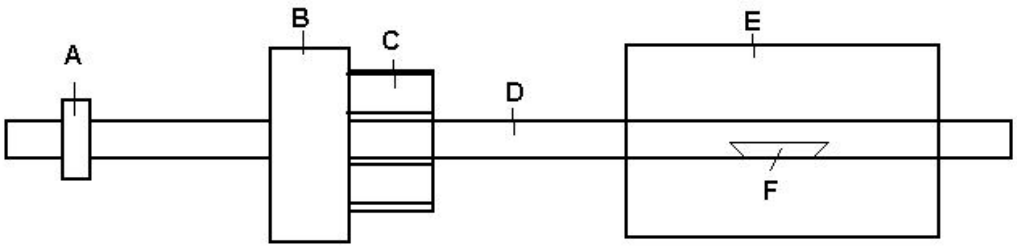

A- Magnet
B- Pump System
C- Carousel
D- Quartz tube
E- Oven
F- Boat

Figure 4.4: Experimental setup for annealing process.

The annealing system consists of a vacuum system connected to an annealing oven, in this case a Lindberg 55322 oven. The temperature inside the oven is measured by a thermocouple. High vacuum conditions are needed during the annealing process to minimize any oxidation and contamination of the samples. To achieve this, a rotary vane pump and a turbomolecular pump were used. In order to open the vacuum a minimum amount of times, eight ceramic sample boats can be placed inside the carousel and these can be selected in turn and pushed into the oven. In order to measure the pressure a cold cathode ionization pressure gauge (Penning) was used, and an average vacuum pressure of 10^{-5} Torr was measured. The samples had to be placed inside ceramic boats, and the boats in turn placed inside the carousel. To push the samples inside the oven, an iron rod, which is controlled by a magnet, was used.

The annealing details for **copper** were as follows:

- 9 samples were annealed at 300˚C for 30 min, and cooled to 150˚C at an average cooling rate of 1.4˚C/min before extracting from the annealing oven.

- 9 samples were annealed at 500˚C for 30 min, and cooled to 150˚C at an average cooling rate of 1.9˚C/min before extracting from the annealing oven.

The annealing details for **molybdenum** were as follows:

- 9 samples were annealed at 1200˚C for 30 min, and cooled to 500˚C at an average cooling rate of 16.1˚C/min before extracting from the annealing oven.

- 9 samples were annealed at 1200˚C for 3 hours, and cooled to 500˚C at an average cooling rate of 16.3˚C/min before extracting from the annealing oven.

These temperatures were chosen based on the recrystallisation temperatures for the materials used. These temperatures are shown in table 4.4.

Table 4.4: Recrystallisation temperature for copper and molybdenum (adapted from Askeland, 1998, p205).

Metal	Melting Temperature (˚C)	Recrystallisation Temperature (˚C)
Copper	1085	200
Molybdenum	2610	900

In the case of copper, the annealing time was kept constant, with the annealing temperature being increased to ensure a larger grain structure. For molybdenum this was not possible. This was due to the fact that the available oven could only reach 1200˚C. Even then, the quartz tube used suffered serious damage during annealing. For this reason the temperature was kept constant while the annealing time was increased between the two sample batches. However, 1200˚C is well above the quoted recrystallisation temperature of molybdenum, and should have been sufficient to ensure adequate grain growth.

4.4 The Split Hopkinson Pressure Bar

4.4.1 History and Experimental Setup

Due to its relative simplicity and robustness, the Split Hopkinson Pressure Bar (SHPB) continues to be one of the most commonly used methods of testing materials at high rates of strain of between 50 s^{-1} and 10^4 s^{-1}. It was developed by Kolsky in the late 1940's from an earlier design of Hopkinson in 1914, and is also known as the Kolsky bar test (Kaiser, 1998; Gray, 1985).

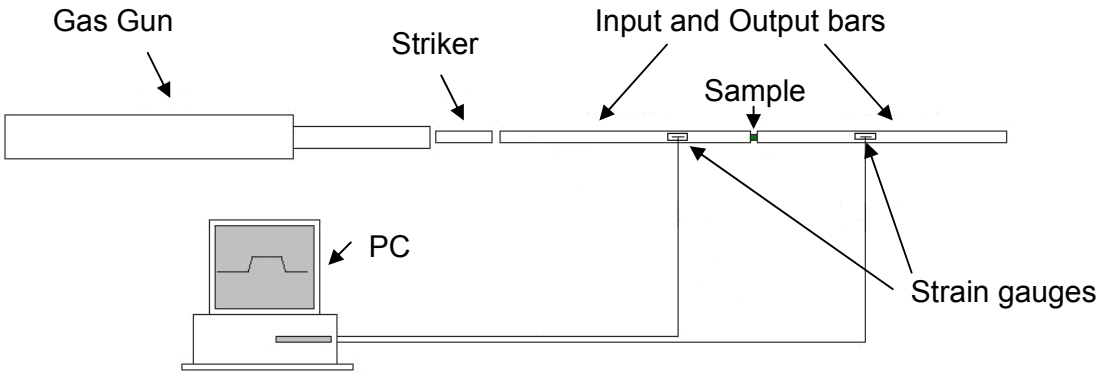

Figure 4.5: Schematic of Split Hopkinson bar apparatus (adapted from Marais *et al*. 2004).

Figure 4.5 shows the basic experimental setup. The SHPB apparatus consists of two long slender bars, the input and output bars that sandwich a short cylindrical specimen between them. Utilizing a high-pressure gas gun, a third bar, known as the striker bar, is propelled at the input bar, causing a compressive stress wave to travel through the input bar to the input bar and test specimen interface. At this interface, a portion of the stress wave propagates through the test specimen while the remainder of the pulse reflects back through the input bar as a tensile stress wave. The non-reflected portion of the stress pulse transmits through the test specimen and into the output bar causing both elastic and irreversible plastic deformation to the specimen. By recording the strains in the input and output bars by using strain gauges, the stress-strain properties of the specimen can be calculated (Kaiser, 1998). Figure 4.6 shows the circuit diagram for a strain gauge which in practice is an electric circuit that is capable of

measuring the minute changes in resistance corresponding to strain. A Wheatstone bridge is used for the measurement of the changing electrical resistance. In figure 4.6, if R1, R2, R3, and R4 are equal, and a voltage, V_{IN}, is applied between contact points A and C, then the output between points B and D will show no potential difference. However, if R4 is changed to some value which does not equal R1, R2, and R3 due to a changing strain in the sample, the bridge will become unbalanced and a voltage will exist at the output terminals which can then be used to determine the induced strain.

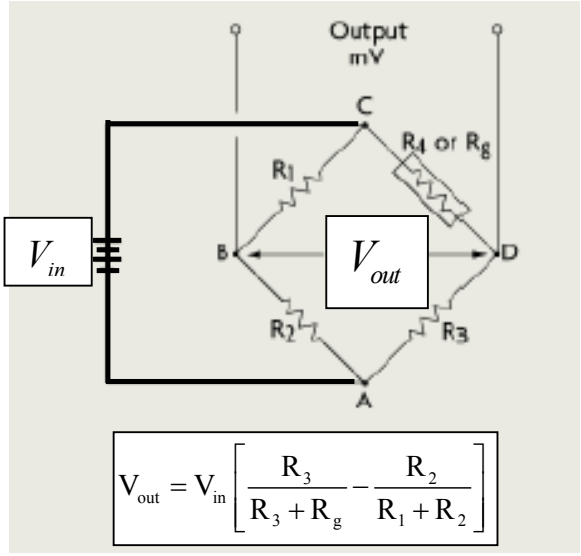

Figure 4.6: Strain gauge circuit (www.omega.com/literature/transactions/volume3/strain2.html).

In practice, R4 is a bonded strain gauge. These gauges consist of a grid of very fine wire or foil bonded to the backing or carrier matrix as shown in figure 4.7. In practice two strain gauges are used on opposite sides of each bar. If the bar bends, one side will be in tension while the other side will be in compressed, and the signals will cancel. In this way bending strains are not registered, while compression strains are registered double. The other reference resistors are also strain gauges, housed in a stress free environment near the bar for temperature compensation.

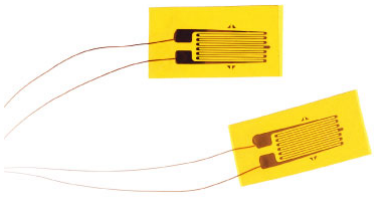

Figure 4.7: Bonded strain gauges. (www.omega.com/literature/transactions/volume3/strain.html).

The results from a typical measurement using a copper sample is shown in figure 4.8, and the same data is used to generate figures 4.9-4.12.

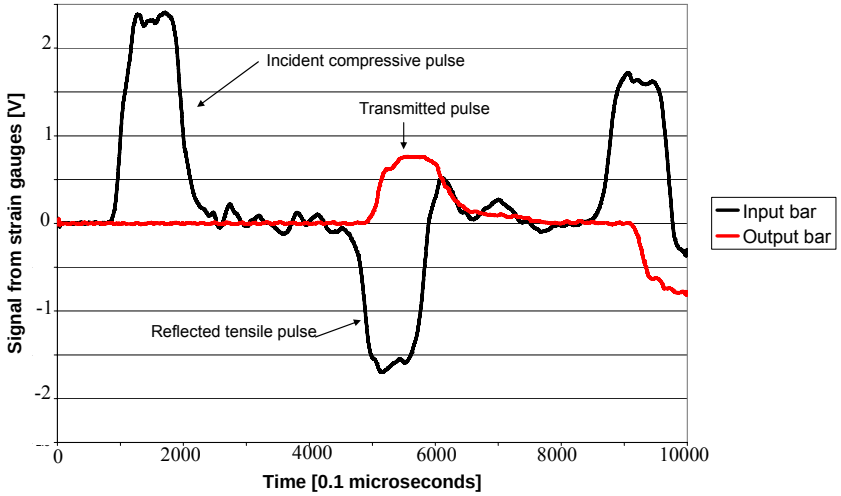

Figure 4.8: Typical signals from the strain gauges during copper sample straining with the split Hopkinson bar.

4.4.2 Basic theory

The following description is based on unpublished notes provided by Mr. T. Cloete, as well as the dissertation by S.T. Marais (Marais *et al.,* 2004). For simplicity, it is assumed that the striker, input and output bars are all made of the same material, and that the striker is narrower and much shorter than the input bar. The striker bar cross sectional area will be denoted by A_s, its initial speed by v_0 and its rebound speed by v_{reb}, while the cross sectional area of the input and output bars will be denoted by A_b. One dimensional wave propagation without dispersion is used to model the stress

waves in the bars. The stress wave speed in a bar is the speed of sound, given by $C = \sqrt{\frac{E}{\rho}}$ where E is the Young's modulus of the material and ρ is its density.

Repeated use will be made of the following fact: for a bar containing a stress wave with stress σ, the particles in the stressed region move with velocity $v = \frac{\sigma}{\rho C}$ relative to the unstressed part of the bar. This may be motivated by considering a length L of uniformly stressed region. The stress in this region can produce a force $F = \sigma A$ for a time $\frac{L}{C}$, or a total impulse of $\sigma A \frac{L}{C}$. This must equal the momentum contained in the region, namely $(\rho AL)v$. It follows that

$$\sigma = \rho C v . \qquad \textbf{(4.2)}$$

Thus, a stress in a region is equivalent to a relative motion of the particles in that region.

By considering the impact of the striker bar with the stationary input bar, which creates two stress waves, the striker rebound velocity can be calculated. The first travels forward in the input bar, while the second travels backwards in the striker, adding a component Δv_s to the stressed regions particle velocity. Since the striker had initial velocity v_0, its stressed region near the point of impact now has particles with velocity $v_0 - \Delta v_s$. The input bar was initially stationary, but after impact its stress region has particle velocity Δv_b. Since the bars are in contact, their impact points travel at the same velocity, and so

$$v_0 - \Delta v_s = \Delta v_b . \qquad \textbf{(4.3)}$$

For the short time that the two bars remain in contact, they exert equal (but opposite) forces on one another. This can be expressed in terms of the stresses as $\sigma_s A_s = \sigma_b A_b$, or using equation 4.3 and recalling that the materials are the same, as

$$(\Delta v_s) A_s = (\Delta v_b) A_b \,. \qquad \textbf{(4.4)}$$

Eliminating Δv_b from equations 4.3 and 4.4 gives $\Delta v_s = \dfrac{A_b}{A_b + A_s} v_0$.

The compressive stress wave in the striker bar travels backwards until it reaches the end free surface, from which it reflects as a tensile wave. Thereafter a region develops from the side furthest from the impact end, for which there exists both a compressive wave travelling backwards and a tensile wave travelling forwards, superimposed on one another. The effective stress in this region, and hence the particle velocity, is therefore doubled. Thus the rebound velocity is given by

$$v_{\text{reb}} = v_0 - 2\Delta v_s = v_0 - 2\frac{A_b}{A_b + A_s} v_0 = \frac{A_s - A_b}{A_s + A_b} v_0 \,. \qquad \textbf{(4.5)}$$

Note that the striker rebound velocity given in the expression above is not negative unless the striker area is less than the bar area, which was assumed to be the case.

4.4.3 Calibration

Calibration is necessary in order to convert the voltage signal to a stress signal. This can be done in three ways:

(a) Theoretically, the voltage for a given stress can be calculated based on the theory of the strain gauge and Wheatstone bridge. The result is $V = GK_{gf} \dfrac{\sigma}{E} \dfrac{N}{4} V_{br}$, where G is the amplifier gain (in this study 1000), K_{gf} is the gauge factor or strain sensitivity (the ratio of its relative change in resistance to the applied strain), N is the number of active arms in the bridge (in this case 2) and V_{br} is the bridge voltage. The Young's modulus E is calculated from the density and measured speed of the stress wave, while the other factors depend on the gauges and electronics.

(b) By the conservation of momentum, the loss of momentum of the striker as it rebounds must equal the impulse inside the input bar. The loss of striker momentum is $\Delta p = m_s\left(v_0 - v_{\text{reb}}\right) = \dfrac{2m_s A_b}{A_s + A_b} v_0$, while if $\sigma = kV$ then the impulse registered as the stress wave passes the strain gauge in the input bar is given by $I = \int F dt = \int \sigma A_b dt = kA_b \int V dt$. The voltage signal of the compressive stress wave in the input bar can be integrated numerically, and hence the calibration obtained as shown in figure 4.9. The compressive stress wave in the input bar is reflected as a tensile wave, so if the integration described above is continued over time while the reflected tensile wave passes the strain gauge, the integrated value decreases by an amount equal to the impulse remaining in the input bar. The rest of the momentum has been transferred to the output bar, and when it is correctly calibrated and its impulse calculated by integration, the result should match the total integrated value of the input bar. Accuracy of this method is dependent on the values of striker impact speed, and measurements relating to the input and output bar diameters.

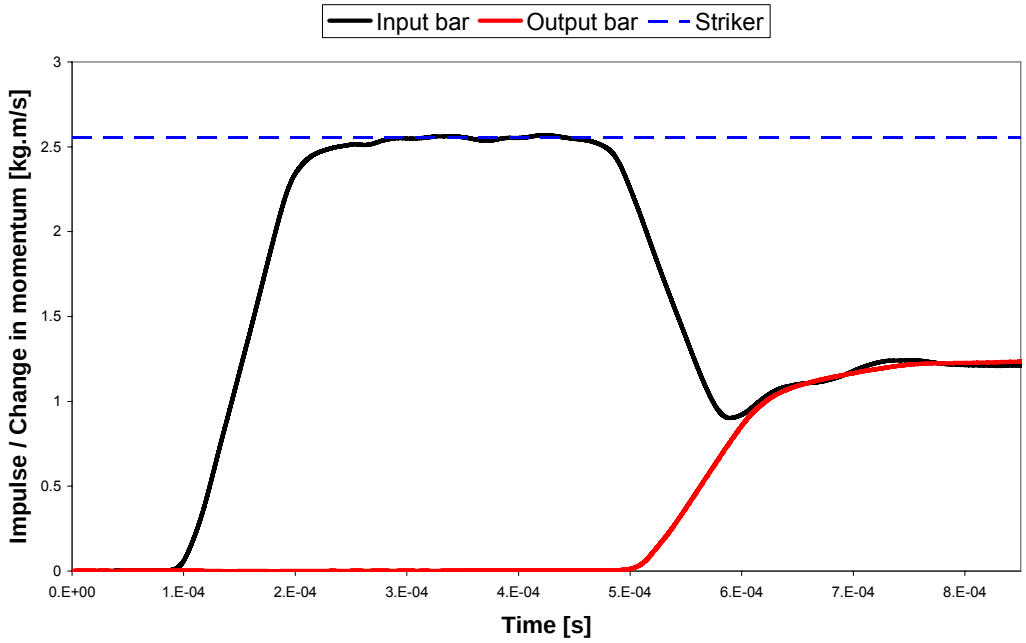

Figure 4.9: Momentum calibration of strain gauge signals from the input and output bar.

(c) The stress in the input bar can be calculated and compared to the measured voltage to get a calibration factor. This is done by eliminating Δv_b from equations 4.3 and 4.4 to get $\Delta v_b = \frac{A_s}{A_b + A_s} v_0$. Using equation 4.2, this particle velocity corresponds to a stress $\sigma = \frac{A_s}{A_b + A_s} v_0 \rho C$ in the input bar. If the voltage signal from the strain gauge in the input bar is rectangular, unattenuated and undistorted by dispersion, then its flat top region corresponds to the calculated stress above.

It must be noted that each of these calibrations has their drawbacks. Because the theoretical method is so highly depended on the electronic components used in the strain gauge, its value can differ from the correct calibration factor due to temperature changes in the components used, which in turn can affect and thus change the known parameters used in the calculation. This method is thus only used as an initial estimate of the calibration factor. The stress method is affected by dispersion, but not by the rebound velocity. Although it was assumed that no dispersion took place, it must be assumed that an error, although slight due to dispersion exists in the stress method calculations and subsequently the stress method serves only as a check. The main calibration is performed using the momentum calibration, which is unaffected by dispersion, and can only be influenced by the calculation of the rebound velocity. It is of course wise to take into account all three methods before deciding on the final calibration factor.

4.4.4 Data analysis

It should be noted that the initial stress pulse passing the strain gauge on the input bar only reaches the end of the bar at a later time given by $t_1 = \frac{L_1}{C_1}$, where L_1 is the distance separating the strain gauge from the end of the bar. By shifting the pulse later by this time, one obtains the incident stress wave σ_i at the end of the input bar as a function of time, where the subscript ***i*** implies the incident wave. This corresponds

to a particle velocity of $v_i = \frac{\sigma_i}{\rho C}$. In a similar way, the reflected tensile wave in the input bar only reaches the strain gauge at time t_1 after being at the end of the bar. By shifting this pulse earlier in time, one obtains the reflected stress wave σ_r at the end of the input bar as a function of time, where the subscript ***r*** implies the reflected wave. This tensile (negative) stress wave corresponds to a particle velocity of $v_r = \frac{-\sigma_r}{\rho C}$, in the same direction as that for the incident pulse, and the total particle velocity at the end of the input bar is $v_1 = v_i + v_r$.

In the output bar, the transmitted compressive pulse at the strain gauge must be shifted back in time by $t_2 = \frac{L_2}{C_2}$, where L_2 is the distance separating the front of the bar from the strain gauge. This gives the transmitted stress wave σ_t at the front of the output bar as a function of time, where ***t*** implies the transmitted wave, with the corresponding particle velocity of $v_2 = \frac{\sigma_t}{\rho C}$.

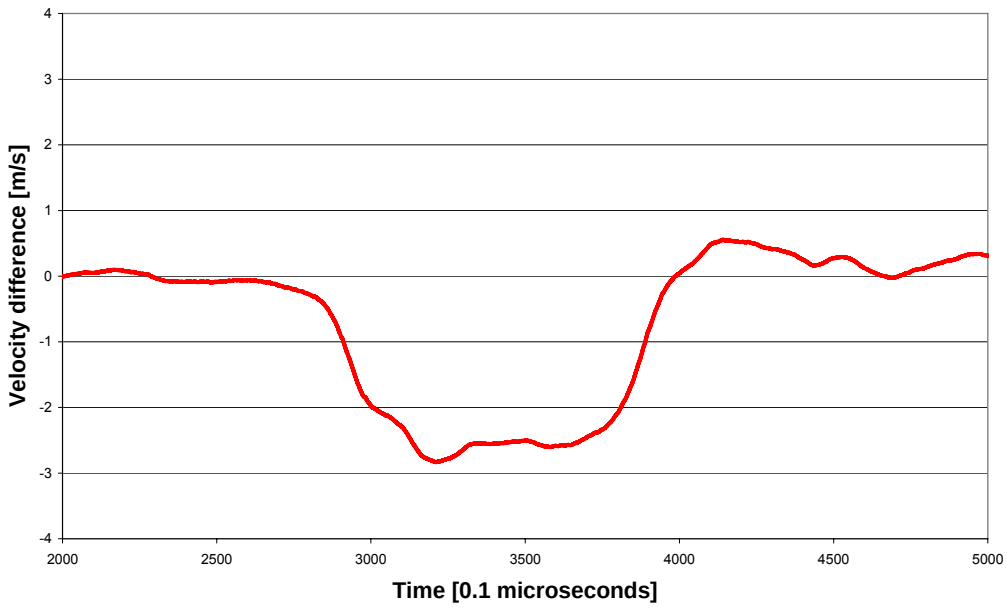

Figure 4.10: Shrinkage velocity as a function of time.

The velocity difference between the end of the input bar and the front of the output bar (back and front of the sample) is $\Delta v = v_2 - v_1$, and can be plotted as shown in figure 4.10. Integrating this velocity over time using the initial length of the sample gives its length as a function of time. From this, the strain as a function of time follow directly from equation 4.6 and a simple derivative leads to the strain rate as a function of time as shown in equation 4.7.

By definition (Askeland, 1998, p 152) the true strain is

$$\varepsilon(t) = \ln \frac{l_0}{l(t)} \tag{4.6}$$

thus

$$\dot{\varepsilon}(t) = \frac{d}{dt}\left(\ln \frac{l_0}{l(t)}\right) = \left(\frac{l_0}{l(t)}\right)^{-1} \frac{d}{dt}\left(\frac{l_0}{l(t)}\right) = \left(\frac{l(t)}{l_0}\right) l_0 \frac{-1}{\left[l(t)\right]^2} \frac{d}{dt}\left(l(t)\right)$$

and subsequently the strain rate is given by

$$\dot{\varepsilon}(t) = \frac{-v(t)}{l(t)}. \tag{4.7}$$

The true stress in the sample is obtained by equating the forces between the sample and the output bar i.e. $\sigma A = \sigma_t A_b$, where the unsubscripted values refer to the sample. From this it follows that the sample stress is

$$\sigma(t) = \frac{A_b}{A(t)} \sigma_t(t). \tag{4.8}$$

To compute the stress history, the area of the sample over time is needed. This is computed by assuming the sample remains cylindrical with unchanging volume as it is compressed, and using the changing sample length to compute its changing cross-sectional area. Using the strain, strain rate and stress histories of equations 4.6, 4.7

and 4.8, one can plot the strain rate and stress as a function of strain as shown in figures 4.11 and 4.12.

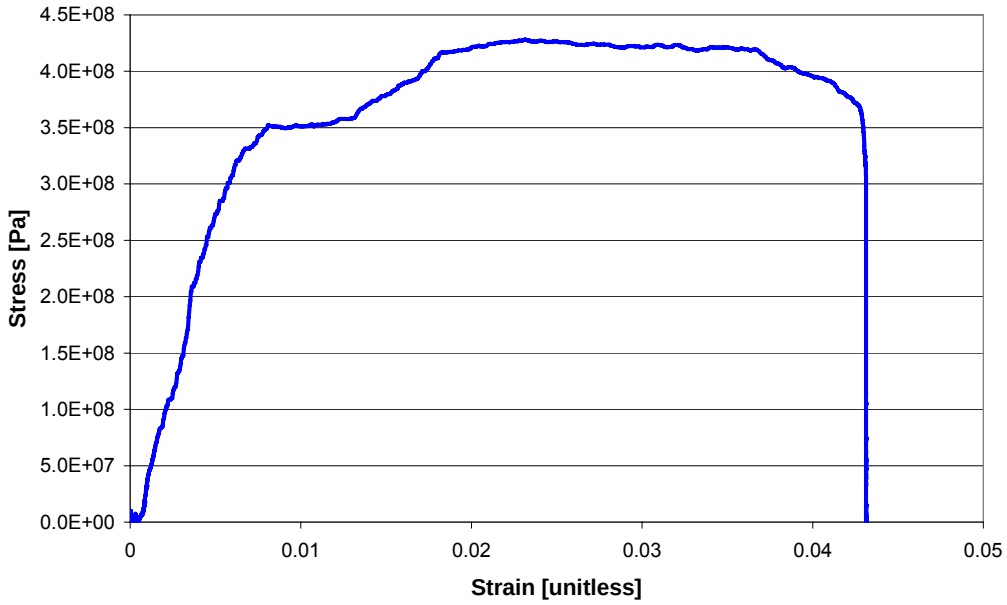

Figure 4.11: Stress-strain graph

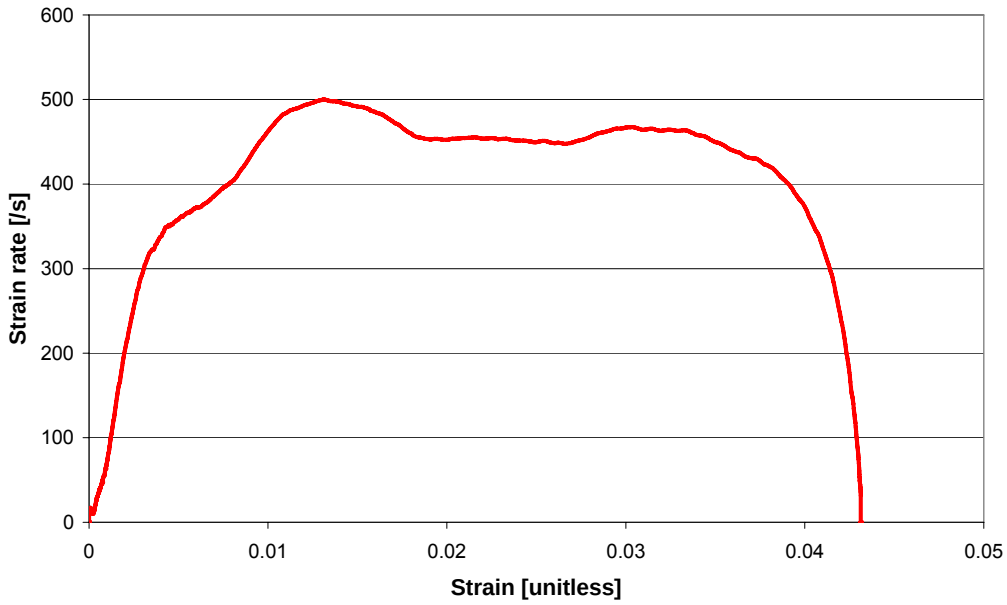

Figure 4.12: Strain rate-strain graph.

4.5 Scanning Electron Microscopy

A Scanning Electron Microscope (SEM) was used to obtain images that were used to determine the size and nature of the grain structure of the various samples. Although an optical microscope was also used, it is assumed that the reader is well versed in the physical characteristics of an optical microscope, and subsequently only the SEM will be discussed.

Scanning electron microscopy is capable of producing high resolution images of a sample surface with an excellent depth of field. Electrons are emitted from a tungsten or lanthanum hexaboride (LaB_6) filament and accelerated towards an anode. The electron beam, typically having energies from a few keV to about 30 keV, is focused by two condenser lenses into a beam with a very fine spot size. The beam then passes through the objective lens, where pairs of scanning coils deflect the beam either linearly or in a raster fashion over a rectangular area of the sample surface. As the primary electrons strike the surface, they are inelastically scattered by atoms in the sample. Through these scattering events, the primary beam effectively spreads and fills a teardrop-shaped volume, known as the interaction volume, extending about 1 to 10 μm into the surface (Exner, 1983, p599).

The most important interactions (see figure 4.13) in this region pertaining to the SEM lead to:

- The emission of secondary electrons is caused by an incident electron imparting some of its energy to a lower energy electron (usually in the K-shell) of a specimen atom. This causes a slight energy loss and path change in the incident electron and the ionization of the specimen atom. The ejected electron leaves the specimen atom with a very small kinetic energy (~5 eV) and is called a “secondary electron”. Each incident electron can produce many secondary electrons.

- Backscattered electrons i.e. primary electrons that are reflected due to an incident electron colliding with an atom in the specimen which lies almost directly in the incident's path. The incident electron is then scattered "backward" 180 degrees. These electrons have almost the same energy as the incident electrons.

- The emission of X-rays caused by the relaxation of the specimen atom after a secondary electron is produced. Since a low energy (usually K-shell) electron was emitted from the atom during the secondary electron process, an inner (low energy) shell now has a vacancy. A higher energy electron can make a transition into the lower energy shell, filling the vacancy. As this happens, the electron can emit an X-ray to balance the total energy.

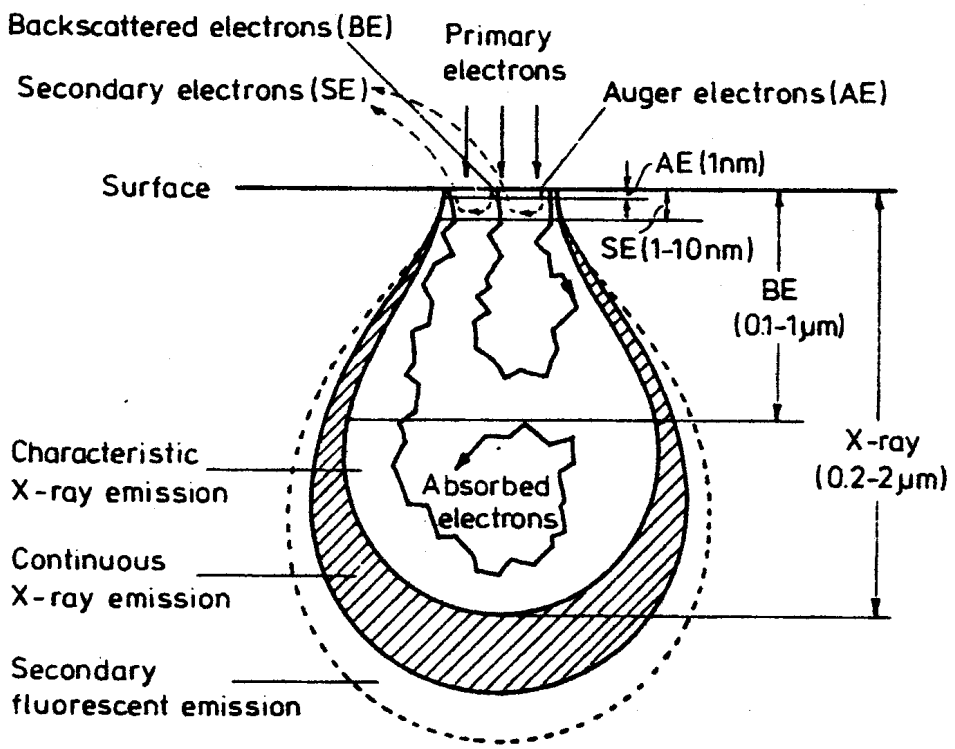

Figure 4.13: Electron interactions with the sample when using SEM (Exner, 1983, p599.

Of the above the most important interactions for the purpose of this study is the emission of the secondary electrons, and the backscattered electrons. Detectors for both these types of emissions are housed in the SEM unit. The electrons are detected by their relevant detector, and converted to a voltage. This signal is then amplified to produce an image. Emission of secondary electrons is very topography related. Due to their low energy, only secondaries that are very near the surface (<10 nm) can exit the sample and be examined. In materials with a high atomic number, a large number of electrons are backscattered by atoms close to the surface, with little change in energy. As the atomic number of the sample material decreases, a smaller number of electrons are backscattered, and more energy is lost. Thus yield, energy spectrum and depth of escape of backscattered electrons are directly related to the atomic number of the material. In general backscattered electrons gives topographic as well as pronounced material contrast from a much larger depth and width and therefore a reduced resolution when compared to secondary electrons (Exner, 1983, p599; www.unl.edu/CMRAcfem/interact.htm). Emitted X-rays may also be detected in a SEM equipped with Energy Dispersive X-ray Spectroscopy (EDS), and are useful for elemental analysis of samples.

4.6 Transmission Electron Microscope

The basic Transmission Electron Microscope (TEM) consists of an electron source (electron gun) and an assembly of magnetic lenses arranged in a vertical column which is evacuated to about 10^{-5} Torr or better (Loretto and Smallman, 1975, p.1.). The electron gun produces a coherent beam of electrons, which can be varied in spot size at the specimen surface by means of a condenser lens system. The specimen is mounted in a special holder which fits into the bore of the objective lens. A double tilt holder enables the specimen to be tilted through angles greater than 30˚ about two orthogonal axes so that appropriate crystallographic analyses can be carried out Although some inelastic scattering does occur, of most importance in the TEM are elastically scattered electrons which pass all the way through the sample and then produce an image on a fluorescent screen (or on a CCD camera). The incident electron beam can be considered as a plane wave having wavelength (Ding, 2006)

$$\lambda = \frac{h}{\sqrt{2m_0 eV(1+\frac{eV}{2m_0 c^2})}}, \tag{4.9}$$

where h is Planck's constant, m_0 is the rest mass of an electron, e is the charge of an electron, V is the accelerating voltage of the electrons and c is the speed of light interacting with the specimen. Diffraction of the incident wave can occur when the Bragg condition (Kittel, 2005, p.25)

$$\lambda = 2d\sin\theta \tag{4.10}$$

is satisfied, where d is the interplanar spacing of the lattice planes and θ is the diffraction angle between the lattice plane and incident beam. The wavelength λ of the incident electron plane wave for an accelerating voltage of 100 kV can be calculated using equation 4.9 above and is 3.7 pm, which is two orders of magnitude smaller than typical interplanar spacings which are in the order of Ångstroms. Hence diffraction angles of the electron beam from crystal planes are also small.

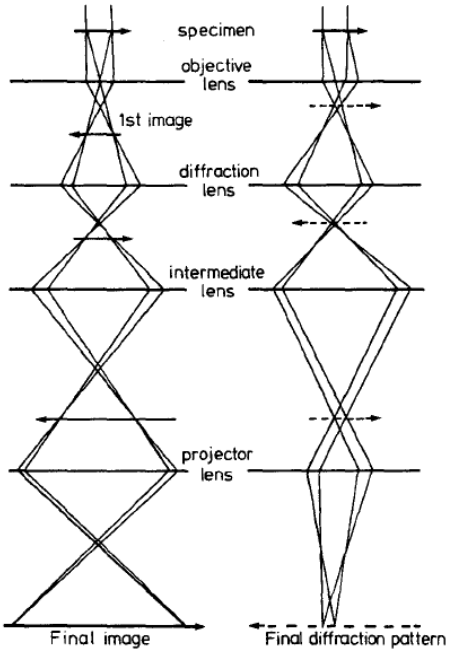

Figure 4.14: TEM configuration to obtain **(a)** a direct magnified image of the specimen and **(b)** a diffraction pattern from the specimen (Loretto and Smallman, 1975, p.3). The actual detailed workings differ from instrument to instrument.

Figure 4.14 illustrates the TEM being used in two possible configurations, based on the strengths of the lenses. After passing through the sample, the electron beam is in both cases focused by the objective lens. On the left (figure 4.14a), the focused image from the objective lens forms a new object for the diffraction lens, which is further magnified to give a picture of the electron density at the bottom surface of the sample. On the right (figure 4.14b), however, the diffraction lens takes as its object the focal plane of the objective lens. At this plane all electron waves exiting the sample at the same angle are focused to a point. Thus, this image consists of a series of bright spots, each spot corresponds to an electron wave exiting the sample in a certain direction. There is a central spot for the incident beam, as well as many spots all around it, each corresponding to different diffracted beams.

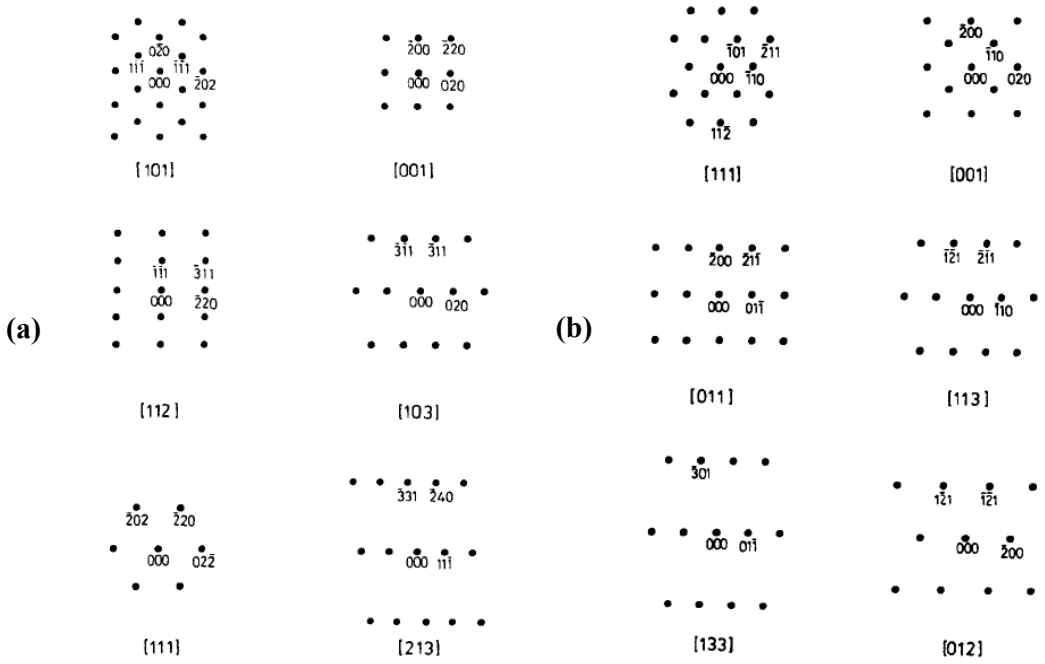

Figure 4.15: Diffraction patterns for materials with **(a)** FCC and **(b)** BCC structures (Loretto and Smallman, 1975, pp. 116 and 121).

The allowed angles for this diffraction pattern depend on the interplanar spacings of the sample through Bragg's law (equation 4.10), and so the pattern gives information on the crystal structure and orientation of the sample. For instance, consider a material with a simple cubic crystal structure oriented with the electron beam very close to the [100] crystal direction. This incident electron beam makes very small angles with the (010), (001), (011), (002) planes etc., which may then diffract the

beam. For thin samples, as in the case with TEM, Bragg's law is relaxed somewhat and all of the above planes can be in an orientation sufficient to diffract strongly, resulting in a square diffraction pattern of spots. If the sample had an FCC crystal structure (but in the same orientation) the structure factor implies that only planes having all-even or all-odd indices can diffract (Hook and Hall, 1991, p.326), and although the square diffraction pattern is retained, there are no diffraction spots from the (010), (001), (011) planes etc., but there is diffraction from the (020), (002), (022) planes etc. For the BCC lattice the structure factor implies that diffraction only occurs from planes for which the sum of the indices is even (Kittel, 2005, p.40), meaning that the (010) plane still cannot diffract, but that diffraction can occur from the (011) plane. If the sample is oriented differently, other crystal planes making very small angles with the beam will be candidates for diffraction: some standard diffraction patterns for FCC and BCC crystals are shown in figure 4.15.

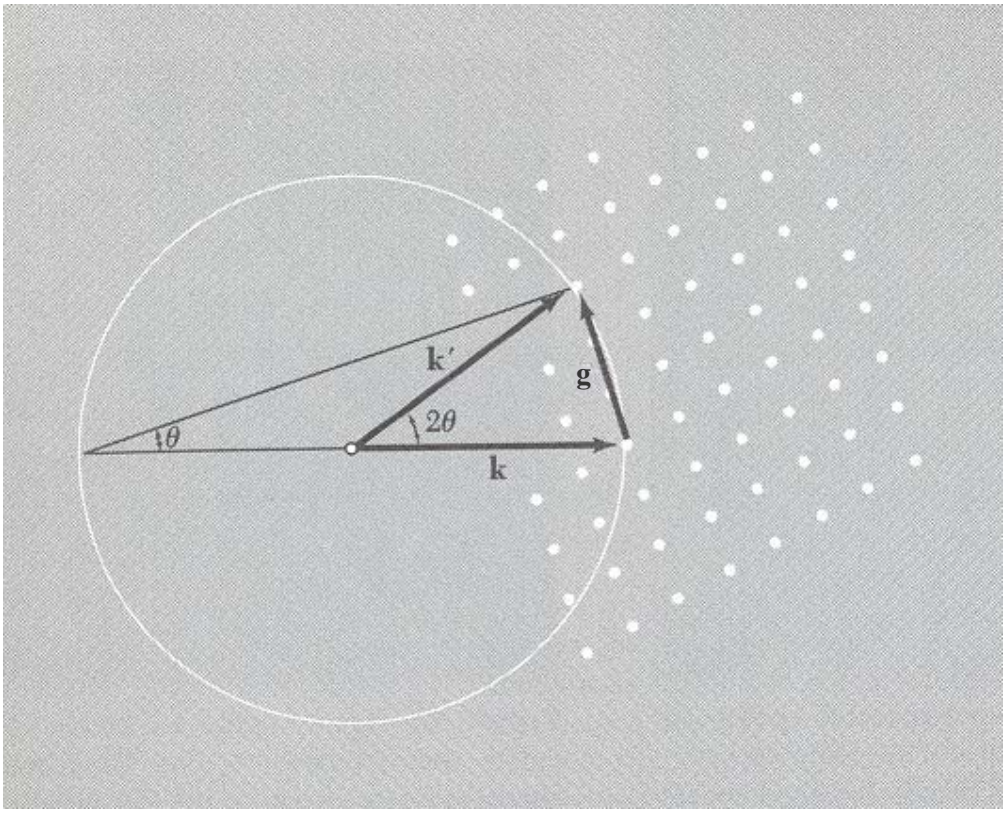

Figure 4.16: Diffraction occurs in directions where the Ewald sphere intersects a reciprocal lattice point (Kittel, 2005, p.33).

Another way to consider diffraction is in terms of reciprocal space, where Bragg's condition can be expressed as (Kittel, 2005, p. 31)

$$\boldsymbol{k}' = \boldsymbol{k} + \boldsymbol{g} \qquad \textbf{(4.11)}$$

where $\boldsymbol{k}$ is the incident electron wave-vector, $\boldsymbol{k}'$ is the diffracted electron wave-vector and $\boldsymbol{g}$ must be some reciprocal lattice vector of the sample crystal. The so-called Ewald sphere may be drawn in reciprocal space with radius $|\boldsymbol{k}|$ and passing through the origin of the reciprocal lattice. Then, whenever the Ewald sphere touches a reciprocal lattice point, one can draw a diffracted wave-vector to that point such that Bragg's condition is satisfied. These diffracted beams occur in directions where the Ewald sphere intersects the reciprocal lattice (figure 4.16). Because the sample is thin (and hence not a perfect infinite crystal), the reciprocal lattice does not consist of points, but rather each point is elongated into a spike perpendicular to the thin crystal direction.

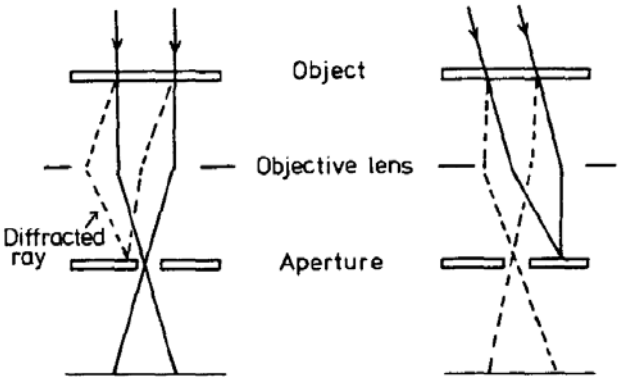

Figure 4.17: Selecting **(a)** the transmitted beam for a bright field image and **(b)** a diffracted beam for a dark field image (Loretto and Smallman, 1975, p.13).

Virtually all analyses of crystal defects are carried out by inserting an aperture in the focal plane of the objective lens, so that only one of the diffracted beams contributes to the formation of the sample image, which gives rise to so-called diffraction contrast. Generally the central undiffracted beam is chosen, as in figure 4.17 (a), and the resulting image is called a bright field image. Alternatively, a diffracted beam may be selected as in figure 4.17 (b), which gives a dark field image. To maximize

contrast, this is best done by tilting the incident beam so that the diffracted spot is aligned with the microscope axis, as shown in the figure. However, it is generally much easier to shift the aperture itself, despite some loss of contrast.

For ease of interpreting the TEM images, it is standard practice to orient the sample until the transmitted and a single diffracted beam are much more intense than any others: this is the so-called two-beam condition (Williams and Carter, 1991, p.361). Under these circumstances, one may regard the image as forming due to diffraction from only a single lattice plane. If the sample were uniform, viewing either the bright field or dark field image would not give any information. However, if a defect such as a dislocation occurs in the sample, the diffracting lane will be distorted near to it due to the defect stress field (see figure 4.18). This may cause the lattice planes to be tilted closer or further from the exact orientation for Bragg diffraction, and so change the electron intensities in the transmitted and diffracted direction relative to the region far away from the defect. If the diffraction of the electron beam is not very strong, because Bragg's condition is not well satisfied i.e. under so-called kinematical conditions, the dark field image will be relatively dark everywhere and the bright field image will be relatively bright everywhere, except over the projected area of the defect. Here, the rotation/tilting of the lattice planes near the defect will result in a region where Bragg's condition is well satisfied, and so enhanced diffraction in this region will result in a bright area in the dark field image and a corresponding dark area in the bright field image. It is, in fact, the strains in the crystal that provide the diffraction contrast of the dislocation, not the core of the dislocation itself. The above explanation of diffraction contrast is a useful way of considering the image formation in the TEM, but in reality the process is more complicated, since even with two-beam conditions the diffraction from the incident beam is usually strong. Under such dynamical conditions the diffracted beam can soon become more intense than the incident beam, but then diffraction occurs back to the incident beam from the diffracted beam. In this way the electron intensity in the incident and diffracted beams oscillate as a function of depth from the top surface of the specimen (Loretto and Smallman, 1975, p.41). This effect is clearly seen near the edge of samples next to a hole, where the contrast oscillates from bright to dark in the form of thickness fringes (Williams and Carter, 1991, p.369). Nevertheless, the strain field of any

defects influence this process and they appear as regions of different contrast on the background.

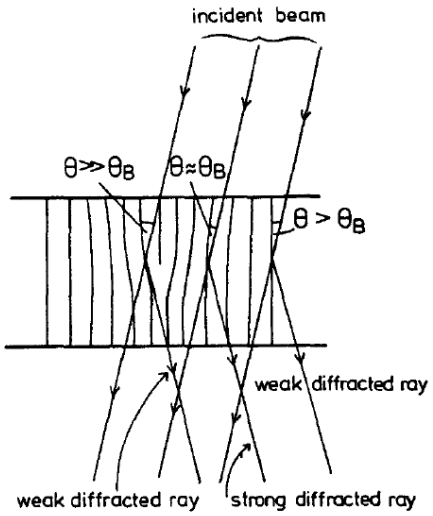

Figure 4.18: Diffraction contrast effect in a TEM: a defect (in this case an edge dislocation) rotates the crystal planes due to its strain field, changing the deviation from the exact Bragg condition and therefore the electron intensities in the transmitted and diffracted beams (Loretto and Smallman, 1975, p.14).

To effect the diffraction process, the strain field of a defect must tilt the diffracting plane i.e. a defect causing atoms to shift in, and not normal to, the diffracting plane will not result in any contrast. Under two-beam conditions the defect contrast is determined by $\boldsymbol{g}\bullet\boldsymbol{R}$, where $\boldsymbol{g}$ is the reciprocal lattice point corresponding to the diffracting plane and $\boldsymbol{R}$ is the strain field of the defect. For a screw dislocation the strain field is given by (Williams and Carter, 1996, p.405)

$$\boldsymbol{R} = \frac{\phi}{2\pi}\boldsymbol{b} \qquad \textbf{(4.12)}$$

where ϕ is the angle taken around the screw dislocation. The strain field is in the direction of the Burgers vector, and so if $\boldsymbol{g}\bullet\boldsymbol{b} = 0$, then $\boldsymbol{g}\bullet\boldsymbol{R} = 0$ everywhere and the screw dislocation will therefore not show any diffraction contrast i.e. it will be invisible, because it does not rotate the diffracting planes. The same dislocation, imaged with a different set of diffracting planes ($\boldsymbol{g}$-vector), may become visible. For

an edge dislocation the strain field is more complicated, and has components in the direction of the Burgers vector as well as in the direction normal to both the Burgers vector and the dislocation line. Nevertheless, the first component is generally more important, and so this explains the well-known *invisibility criterion*: $\boldsymbol{g}\bullet\boldsymbol{b} = 0$ for dislocations. In fact, dislocations are generally invisible if $\boldsymbol{g}\bullet\boldsymbol{b} < {}^{1}/_{3}$, but may be visible even if $\boldsymbol{g}\bullet\boldsymbol{b} = 0$ when $\boldsymbol{g}\bullet(\boldsymbol{b}\times\boldsymbol{u}) = 0$ (Williams and Carter, 1991, p.406).

4.7 Chemical testing

As discussed in section 3.3.6, the impurity concentration present in shaped charge liner material has a large impact on the ductility of the material. It is thus of great importance that chemical analysis had to be performed on both the copper and molybdenum supplied.

From the literature study done on previous research concerning this issue, it was found that the most important impurity elements are H, O, C, S, N and Fe (Schwartz *et al.,* 1998).

Discussions with Prof Purcell at the Department of Chemistry, University of the Free State revealed that:

- Specialty techniques would have to be used due to low concentrations (parts per millions (ppm)) that would have to be measured.
- The commonly used techniques all use an acidic solution to dissolve the samples before actual analysis takes place. However, most of the elements being tested for are present in the acids used to make the solution. For this reason other techniques would have to be used.

The decision was made to contact the CSIR (in particular Martin van Staden, and Retha Rossouw) on the matter, and to enquire if their Glow Discharge Optical Spectroscopy (GDOS) apparatus would be able to perform the analysis needed. Unfortunately the CSIR did not possess the necessarily standards needed to perform

the analysis. It was also suggested that a combustion method would also be more appropriate for the testing, and that Sandra Graham at MINTEK should be contacted on the matter. Again MINTEK did not possess the necessarily standards needed to perform the analysis. The LECO company was also contacted via the CSIR. This company manufactures and distributes chemical analysis apparatus. It was indicated by them that none of their South African clients performs analysis for outside companies.

Adam Schwartz at the Lawrence Livermore National Laboratory in the United States was contacted. This researcher, who has done extensive work on impurity concentrations in shaped charge liner material, recommended that contact should be made with Northern Analytical Laboratories in the United States. Contact was subsequently made with Northern Analytical Laboratories concerning chemical testing of the samples. Although they did not provide H analysis, C, S, N, and O could be tested using the Vial Combustion and Inert Gas Fusion methods, while Fe could be tested by means of Inductively Coupled Plasma Mass Spectrometry (ICPMS).

Another technique that was considered is Glow Discharge Mass Spectrometry (GDMS) (http://www.shivatec.com/new/gdmsdesc.php4). In GDMS the sample, in the shape of a pin, is the cathode for a DC glow discharge. Atoms sputtered from the sample surface into the plasma are ionised, and ions exiting the source are analysed by a double focusing mass spectrometer. Elemental concentrations are determined from the mass separated ion beam currents. Each isotopic ion beam current is divided by the appropriate isotopic fraction to obtain the part of the total ion beam current due to that element. Since each element has a different probability for ionisation, each elemental ion current is multiplied by a Relative Sensitivity Factor (RSF) to obtain a uniform basis for comparison. The elemental ion currents are then summed to obtain the total ion current from the sample (excluding plasma ions). Each element concentration tabulated is determined by taking the ratio of the corrected element current to the total sample ion current. Determination of impurities at the parts per billion level in the solid is possible.

A formal quote and further information was requested from the following companies:

- Northern Analytical Laboratories, United States of America. (www.northernanalytical.com)
- CSMA Ltd., United Kingdom (www.csma.ltd.uk)
- NRC Institute for National Measurement Standards, Canada (www.inms-ienm.nrc-cnrc.gc.ca/en/gdms/pricing_e.php)
- Shiva Technologies Inc, United States of America. (www.shivatec.com)

After correspondence with the various companies, it was decided to send samples to CSMA Ltd. This company would then test each of the samples for 75 different impurity elements from Lithium (Li) to Uranium (U) using GDMS. Unfortunately due to practical reasons this excluded H, but the test still gives a useful indication of the purity of each material used. These results could also be compared to the specifications required by Denel Land Systems. Samples were requested in the form of 5 mm^3 cubes. Samples were extracted from the original liners by cutting squares of the material with a band saw. The samples were water cooled during cutting to ensure that no segregation of any impurities to the surface occurred.

Unfortunately on arrival of the samples at the analyst in France, that would perform the analysis, it was decided that the samples were too small for full GDMS analysis, and that a indium binder would have to be used. This made it difficult to quantify the C, N and O, because of the elements contained in the binder. Subsequently as these elements were deemed essential, the results were considered incomplete, as only semi-quantitative results for these elements were received. On correspondence with CMSA is was learned that for fully quantified analysis of C, N and O samples of at least 20 mm x 20mm x 20mm would be required. Failing these requirements, Interstitial Gas Analysis (IGA) could be used. This is a technique where the sample is combusted, and the relevant element detected with Non-Dispersive Infrared Spectroscopy. As it was impossible to extract samples with the required dimensions for further GDMS testing from the liners, it was decided to use IGA. A comparison of

the semi-quantitative results obtained with GDMS and the fully quantified analysis with IGA of C, N and O is shown in tables 4.5 and 4.6 for copper and molybdenum respectively.

Table 4.5: Results of IGA analysis for copper (weight ppm).

	GDMS	IGA
C	5	3.5
N	5	<1
O	45	30

Table 4.6: Results of IGA analysis for molybdenum (weight ppm).

	GDMS	IGA
C	10	16
N	170	<5
O	120	24

Although the results for copper are comparable, there are some serious doubts regarding the initial GDMS results for molybdenum. As an example, consider that the initial GDMS estimate for the N content in molybdenum is 170 ppm, but the IGA results indicates a content smaller than 5 ppm.

The major impurities present in copper are listed in table 4.7.

Table 4.7: Most prolific impurities in copper.

Impurity	Concentration (ppm)
P	45
O	30
Ag	12
S	6.3
Ni	2.2

The complete results are shown in table 4.8 for copper.

Table 4.8: Complete chemical analysis results for copper.

Trace chemical analysis of copper (ppm weight)

H																He
Li < 0.001	Be < 0.001											B < 0.005	C 3.5	N <1	O 30	F < 0.05	Ne
Na < 0.005	Mg < 0.005											Al 0.01	Si 0.35	P 41	S 6.3	Cl 0.12	Ar
K < 0.01	Ca < 0.01	Sc < 0.001	Ti < 0.005	V < 0.001	Cr 0.01	Mn 0.02	Fe 0.83	Co 0.007	Ni 2.2	Cu Matrix	Zn < 0.01	Ga < 0.05	Ge < 0.05	As 0.54	Se 0.61	Br < 0.005	Kr
Rb < 0.005	Sr < 0.005	Y < 0.005	Zr < 0.005	Nb < 0.005	Mo 0.05	Tc	Ru < 0.005	Rh < 1	Pd 0.12	Ag 12	Cd < 0.01	In < 0.005	Sn 0.12	Sb 0.85	Te < 0.05	I < 0.05	Xe
Cs < 0.005	Ba < 0.005	La < 0.005	Hf < 0.005	Ta < 1	W < 0.005	75 Re < 0.005	Os < 0.005	Ir < 0.005	Pt < 0.005	Au < 0.01	Hg < 0.01	Tl < 0.001	Pb 0.34	Bi 0.08	Po	At	Rn
Fr	Ra	Ac															

Ce < 0.005	Pr < 0.005	Nd < 0.005	Pm	Sm < 0.005	Eu < 0.005	Gd < 0.005	Tb < 0.005	Dy < 0.005	Ho < 0.005	Er < 0.005	Tm < 0.005	Yb < 0.005	Lu < 0.005
Th < 0.0001	Pa	U < 0.0001											

A comparison between the impurity concentrations present in the copper supplied by Denel Land Systems and impurity concentrations as measured by Schwartz *et al.,* (1998) for Hitachi C10100 stock high purity copper is shown in table 4.9.

Table 4.9: A comparison of impurities present in copper.

	Concentration (weight ppm)	
Impurity	**Denel Land Systems**	**Hitachi C10100**
C	3.5	5.0
N	<1	<0.1
O	30	6.0
Si	0.35	0.2
P	41	0.4
S	6.3	4.0
Fe	0.83	2.0
Ni	2.2	1.0
As	0.54	0.4
Se	0.61	0.3
Ag	12	6.4
Sb	0.85	0.3
Pb	0.34	0.2
Bi	0.08	0.2
Total	99.6	26.5

The copper used by Denel Land Systems does not compare well to the Hitachi stock. This is obvious if the total amounts of impurities present in the two copper samples are compared. Special attention should be given to the O, P and Ag content.

The impurity concentration results for molybdenum are shown in table 4.10.

Table 4.10: Complete results chemical analysis results for molybdenum.

Trace chemical analysis of molybdenum (ppm weight)

H																He
Li < 0.005	Be < 0.005											B 0.88	C 16	N <5	O 24	F < 0.01	Ne
Na 4.4	Mg 1.5											Al 5.1	Si 9.5	P 1.7	S 0.59	Cl 0.14	Ar
K 8	Ca 5.3	Sc < 0.005	Ti < 10	V 0.22	Cr 24	Mn 1.7	Fe 39	Co 4.0	Ni 10	Cu 2.2	Zn < 0.05	Ga < 0.05	Ge < 0.05	As 0.24	Se < 0.05	Br < 0.01	Kr
Rb < 0.05	Sr < 0.1	Y 0.17	Zr < 0.8	Nb 0.35	Mo Matrix	Tc	Ru < 0.05	Rh < 0.05	Pd < 0.05	Ag < 0.5	Cd < 0.1	In Binder	Sn < 0.05	Sb 1.2	Te < 0.01	I < 0.01	Xe
Cs < 0.01	Ba < 0.5	La < 0.01	Hf < 0.01	Ta < 10	W 140	Re 0.25	Os < 0.005	Ir < 0.005	Pt < 0.01	Au < 0.05	Hg < 0.005	Tl < 0.005	Pb < 0.005	Bi < 0.005	Po	At	Rn
Fr	Ra	Ac															

Ce < 0.01	Pr < 0.01	Nd < 0.01	Pm	Sm < 0.01	Eu < 0.01	Gd < 0.01	Tb < 0.01	Dy < 0.01	Ho < 0.01	Er < 0.01	Tm < 0.01	Yb < 0.01	Lu < 0.01
Th 0.033	Pa	U 0.20											

The major impurities present in the molybdenum are listed in table 4.11. It can easily be seen that the molybdenum is not nearly as pure as the copper, and that some urgent attention to this matter is needed if optimal shaped charge liner performance is desired.

Table 4.11: Most prolific impurities in molybdenum.

Impurity	Concentration (weight ppm)
W	140
Fe	39
Cr	24
O	24
Ni	10
Ta	<10
K	8
Ca	5.3

4.8 References

Askeland D.R. **[1998]** *The Science and Engineering of Materials*, Stanley Thornes Ltd.

Ding. Y. **[2006]**. Fundamental Theory of Transmission Electronic Microscopy (http://www.nanoscience.gatech.edu/zlwang/research/tem.html, accessed 14 Nov 2006).

Exner H.E. **[1983]** *Qualitative and Quantitative Surface Microscopy* in *Physical Metallurgy*, 3nd Ed, Elsevier Science Publishers

Gray G.T. **[1985]** *ASM Handbook, Vol 8, Mechanical testing and Evaluation,* ASM international.

Hedberg C.L. **[1995**] *Handbook of Auger Electron Spectroscopy*, 3rd Ed, Physical electronics inc.

Hook J.R. and Hall H.E., **[1991]**. *Solid sate Physics*, 2nd Ed , Wiley.

Kaiser M.A. **[1998]** *Advancements in Split Hopkinson Bar test*, M.Sc Dissertation (Unpublished).

Kittel C., **[2005]**. *Introduction to solid state physics*, 8th Ed., John Wiley and Sons.

Loretto M.H. and Smallman R.E., **[1975]**. *Defect analysis in electron microscopy* (Chapman and Hall).

Marais S.T., Tait R.B., Cloete T.J. and Nurick G.N. **[2004]** *Latin American Journal of Solids and Structures* **1** p319

Meyers M.A., Andrade U.R. and Chokshi A.H. **[1995]** *Metallurgical and Materials transactions* **26A** p2881

Schwartz, A.J., Lassila D.H. and Baker E.L **[1998]** *17th International Symposium on Ballistics*, Midrand, South Africa. p439

Williams D.B. and Carter C.B., **[1996]**. *Transmission electron microscopy: a textbook for materials science* , Plenum Press.

Viljoen P.E., Bezuindenhout F., Berning G.L.P. and Myburg G. **[1989]** *Review of Scientific Instrumentation* **60(11)** p3552

http://www.shivatec.com/new/gdmsdesc.php4 accessed 16 Nov 2006 (Author anonymous)

www.unl.edu/CMRAcfem/interact.htm accessed 16 Nov 2006 (Author anonymous)

http://www.omega.com/literature/transactions/volume3/strain.html accessed 4 May 2007 (Author anonymous)

http://www.omega.com/literature/transactions/volume3/strain.html accessed 4 May 2007 (Author anonymous)

Chapter 5

Deformation of samples by means of the Split Hopkinson Pressure Bar

5.1 Introduction

The Split Hopkinson Pressure Bar (SHPB) is a technique used for deforming metals at high strain rates, and is commonly used in research regarding shaped charges (Meyers *et al.,* 1995). As such an apparatus was not available at the University of the Free State, all work pertaining to the subject was performed at the Blast Impact and Survivability Research Unit (BISRU) at the University of Cape Town hosted by Prof. G. Nurick and assisted by Mr. T. Cloete. The apparatus used at BISRU is shown in figure 5.1. See section 4.4 for a complete discussion concerning the theory and experimental setup of this technique.

Figure 5.1: Photo of SHPB at BISRU (Marais *et al*., 2004).

5.2 Experimental

5.2.1 Experimental procedure

Cylindrical samples to be tested were extracted from the original copper and molybdenum shaped charge liners by means of Electric Discharge Machining (see section 4.2). These samples had a diameter and length of approximately 5 mm, which complies with the required length/width ratio of 0.5 to 1.0 which is necessary to reduce frictional effects, as well as radial and longitudinal inertia effects, during SHPB measurements (Gray, 1985, p471). The original molybdenum liner and a sample are shown in figure 5.2.

Figure 5.2: Molybdenum liner used, with sample extracted from the liner using spark erosion. Images do not have the same scale.

Several dummy samples, cut from an industrial copper rod and from a different molybdenum shaped charge liner were also strained. This was done firstly to gain experience with the apparatus, and secondly to determine appropriate experimental parameters that would be used for the straining of the actual samples. In this case the samples had to be strained at two strain rates, the lower rate to be approximately half of the higher strain rate, and with ideally a fixed amount of strain. This would make

all the results for each material comparable to the other. All straining was performed at room temperature.

The experimental procedure for straining the samples was as follows:

1) The correct input bar and output bar is selected. This is done by comparing the yield strength of the bar to that of the material that is to be deformed. By choosing a bar material with an higher yield strength than that of the sample material, the possibility of damage occurring to the bar during straining that might lead to false readings is reduced. The bars used are made of 'silver steel', which is essentially a tool steel with alloy composition: 1%C, 0.3%Si, 0.4%Cr and 0.35%Mn (personal communications with Mr. T. Cloete). A comparison between the yield strength of the bar material and values for the sample materials from the literature is shown in table 5.1. These values are of course only an indication of the sample properties, as these properties might vary from those stated in the literature due to pre-straining history, and chemical impurities. It would of course be wise to determine the yield strength of each sample before straining by means of quasi-static testing. Unfortunately such facilities were not directly available.

Table 5.1: Material yield strength at room temperature of the materials tested as well as the input and output bars (Askeland, 1998, p416; Lichtenberger *et al*., 1996).

	Bars	**Copper**	**Molybdenum**
Yield strength (MPa)	1000	35-365	600-950

2) The rails are aligned horizontally and checked to ensure that the bars move with the least amount of friction.

3) By experimentation an appropriate striker bar is selected to ensure that the correct strain and strain rate is achieved. The seating depth of the bar in the gas gun barrel is also chosen. Similarly an appropriate pressure for the nitrogen gas gun was selected. This pressure depended on the amount of strain required.

4) Electronics are switched on. This included the striker velocity speed trap system*, amplifier, power source, oscilloscope and computer. Settings are checked. This included the bridge voltage and amplifier voltage. The data capturing program is also initialized. It should be noted that the oscilloscope card inside the computer which records this data is set to record data from 100 μs before triggering (pre trigger time), or 1000 data points.

5) A single bar calibration is performed. A single bar is placed in the rails. The appropriate striker bar is loaded, and the gas gun is pumped to the chosen pressure. The data capturing program is activated and the striker velocity oscilloscope is set to trigger. This oscilloscope records the time that it takes the front end of the striker bar to traverse two speed traps that are placed at the front of the gas gun barrel. By pressing a safety button, the firing mechanism is activated. After firing, the data is saved, and the time registered on the striker velocity oscilloscope is noted. This time will later be used to determine the striker velocity.

6) A double bar calibration is performed. It is done exactly as the single bar calibration, except that both bars are used, the ends pushed together with a thin film of grease applied between them.

7) A dummy run is performed. Procedure is as per double bar calibration, except that a dummy sample is placed between the bars, with a thin film of grease on both interfaces. This keeps the sample in place, and reduces frictional effects. A sample cage is used for safety and to catch the sample after the bar ends separate. The data is then analysed to ensure that the results are satisfactory for the given batch of samples to be strained.

8) The samples are strained as in step 7.

* This consists of a double infrared diode system mounted on the SHPB barrel connected to an oscilloscope. When each of the two beams is intercepted by the front of the striker bar, this is registered by the oscilloscope. The time difference between these two signals, and the distance between the diodes can then be used to determine the striker velocity.

Tables 5.2 and 5.3 show some of the experimental parameters that were used for the SHPB apparatus.

Table 5.2: Physical parameters of input, output and striker bars.

	Length (cm)	Mass (kg)	Diameter (mm)	Density ($kg.m^{-3}$)
Input Bar	200.6	4.97	19.95	7926
Output Bar	209.6	5.14	20.20	7652
Striker 1 (Lower Strain Rate)	24.800	0.54650	19.03	7748
Striker 2 (Higher Strain Rate)	10.116	0.22264	19.03	7738

Table 5.3: Settings used with the SHPB during testing.

		Copper	Molybdenum
Striker Bar 1 (Lower Strain Rate)	**Gas gun pressure (kPa)**	250	700
	Bridge voltage (V)	2.5	2.5
	Pulse shaping	No	Yes
Striker Bar 2 (Higher Strain Rate)	**Gas gun pressure (kPa)**	400	700
	Bridge voltage (V)	1.5	1.3
	Pulse shaping	Yes	Yes

Although all the bars were reported to be made of 'silver steel', their densities differ by up to 3%. Although their physical parameters were carefully measured, the uniformity of the diameter along the bar was not checked, which could account for the difference. The origin of the bars is unknown, so it is also possible that they do actually differ slightly in density. In calculating the striker rebound velocities (section 4.4.2) it was assumed that the striker and input bars are made of the same material (with the same density and wave speed). Thus the calculated rebound velocity might be slightly inaccurate. This is not considered to be a serious issue since the rebound velocity was only used in the theoretical calibration (section 4.4.3), whereas the data analysis takes into account the density differences.

5.2.2 Data analysis

A Microsoft Office Excel spreadsheet, as shown in figure 5.3, was compiled to perform the data analysis using the theory discussed in section 4.4.

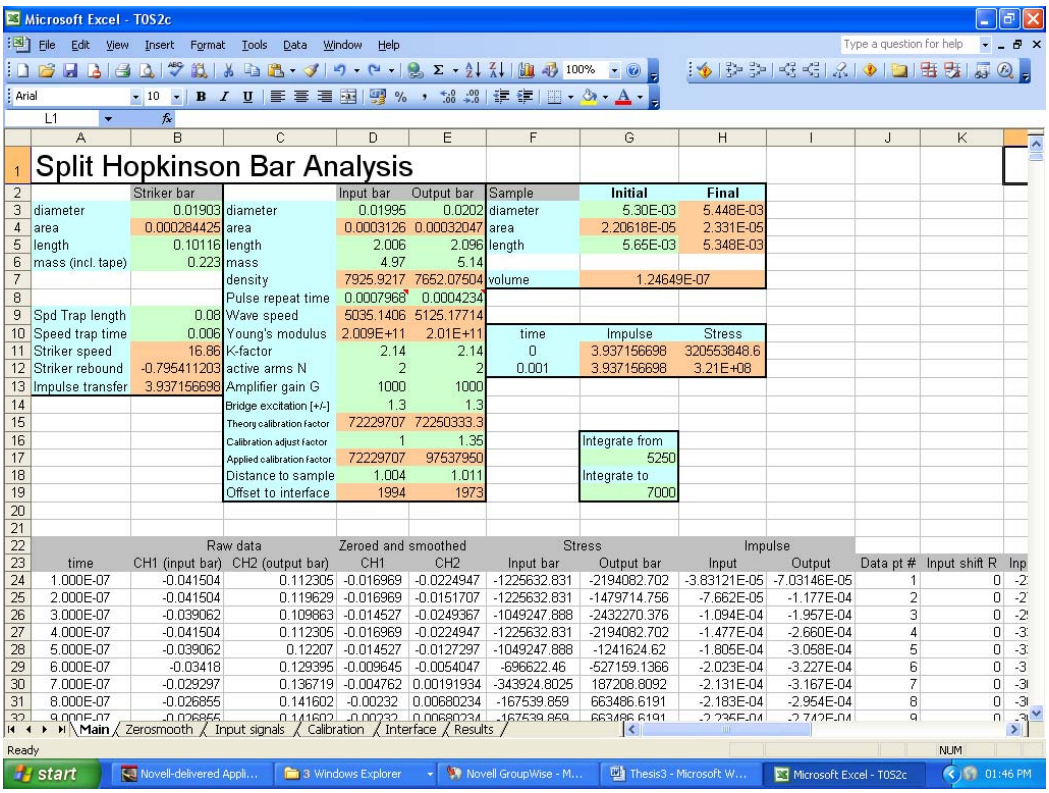

Microsoft Excel - T0S2c

Split Hopkinson Bar Analysis

	Striker bar		Input bar	Output bar	Sample	Initial	Final
diameter	0.01903	diameter	0.01995	0.0202	diameter	5.30E-03	5.448E-03
area	0.000284425	area	0.0003126	0.00032047	area	2.20618E-05	2.331E-05
length	0.10116	length	2.006	2.096	length	5.65E-03	5.348E-03
mass (incl. tape)	0.223	mass	4.97	5.14			
		density	7925.9217	7652.07504	volume	1.24649E-07	
		Pulse repeat time	0.0007968	0.0004234			
Spd Trap length	0.08	Wave speed	5035.1406	5125.17714			
Speed trap time	0.006	Young's modulus	2.009E+11	2.01E+11	time	Impulse	Stress
Striker speed	16.86	K-factor	2.14	2.14	0	3.937156698	320553848.6
Striker rebound	-0.795411203	active arms N	2	2	0.001	3.937156698	3.21E+08
Impulse transfer	3.937156698	Amplifier gain G	1000	1000			
		Bridge excitation [+/-]	1.3	1.3			
		Theory calibration factor	72229707	72250333.3			
		Calibration adjust factor	1	1.35	Integrate from		
		Applied calibration factor	72229707	97537950	5250		
		Distance to sample	1.004	1.011	Integrate to		
		Offset to interface	1994	1973	7000		

	Raw data			Zeroed and smoothed		Stress		Impulse				
time	CH1 (input bar)	CH2 (output bar)	CH1	CH2	Input bar	Output bar	Input	Output	Data pt #	Input shift R	Inp
1.000E-07	-0.041504	0.112305	-0.016969	-0.0224947	-1225632.831	-2194082.702	-3.83121E-05	-7.03146E-05	1	0	-2
2.000E-07	-0.041504	0.119629	-0.016969	-0.0151707	-1225632.831	-1479714.756	-7.662E-05	-1.177E-04	2	0	-2
3.000E-07	-0.039062	0.109863	-0.014527	-0.0249367	-1049247.888	-2432270.376	-1.094E-04	-1.957E-04	3	0	-2
4.000E-07	-0.041504	0.112305	-0.016969	-0.0224947	-1225632.831	-2194082.702	-1.477E-04	-2.660E-04	4	0	-3
5.000E-07	-0.039062	0.12207	-0.014527	-0.0127297	-1049247.888	-1241624.62	-1.805E-04	-3.058E-04	5	0	-3
6.000E-07	-0.03418	0.129395	-0.009645	-0.0054047	-696622.46	-527159.1366	-2.023E-04	-3.227E-04	6	0	-3
7.000E-07	-0.029297	0.136719	-0.004762	0.00191934	-343924.8025	187208.8092	-2.131E-04	-3.167E-04	7	0	-3
8.000E-07	-0.026855	0.141602	-0.00232	0.00680234	-167539.859	663486.6191	-2.183E-04	-2.954E-04	8	0	-3
9.000E-07	-0.026855	0.141602	-0.00232	0.00680234	-167539.859	663486.6191	-2.236E-04	-2.742E-04	9	0	-3

Main | Zerosmooth | Input signals | Calibration | Interface | Results

Ready

Figure 5.3: Main page of data analysis spreadsheet.

Some of the important steps in the analysis of the data as illustrated for the molybdenum sample T0S2c are as follows:

1) The raw data consisting of 10000 data points gathered over 1 ms is copied into the main spreadsheet, and is shown in figure 5.4. This data consists of amplified voltage signals from the strain gauges recorded every 10^{-7}s. This spreadsheet contains all the experimental parameters that are necessary to calculate the final stress strain curves.

2) Next the raw data is zeroed. This is necessary due to the offset introduced by the electronics in the original voltage signal received by the data capturing

program*. By taking an average over the first 200 data points for a given signal during the pre trigger time, and then subtracting this value from each data point in the signal, the whole signal is zeroed as show in figure 5.5.

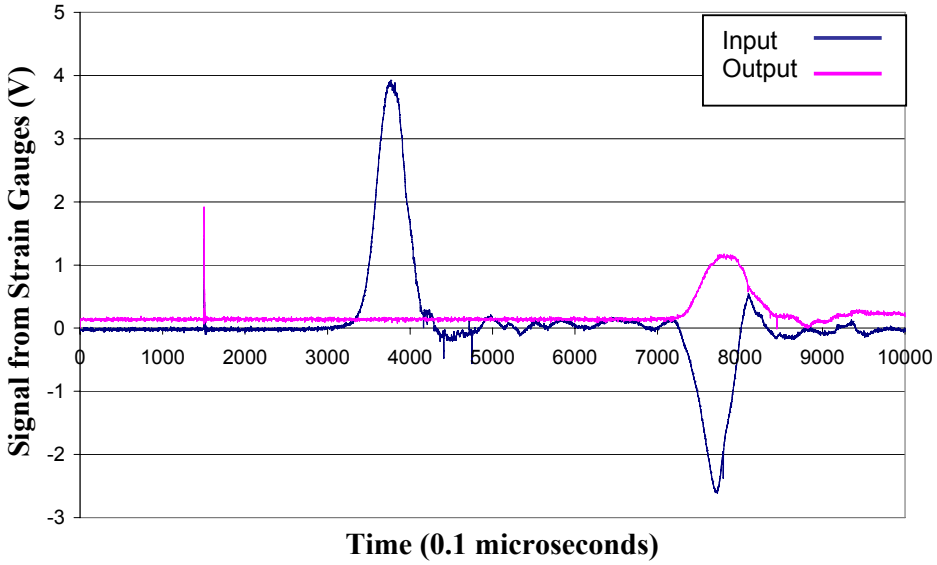

Figure 5.4: Raw SHPB data for the input and output bars.

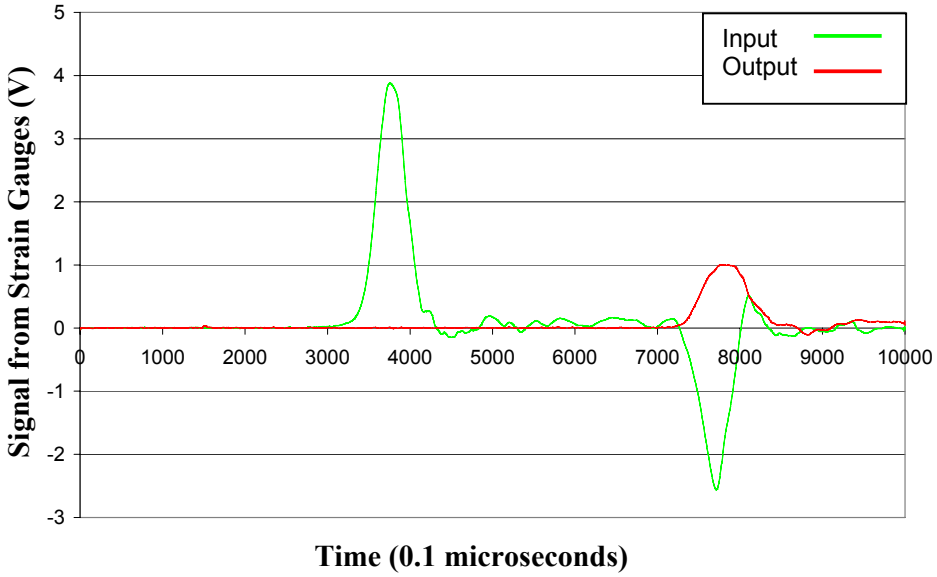

Figure 5.5: Zeroed and smoothed data for the input and output bars.

* It is possible to remove this offset using the electronics, but this causes the signal from the input bar and output bar strain gauges to fall on top of each other when viewed on the oscilloscope which can lead to confusion.

3) Due to spikes in the raw data, it is also necessary to smooth the signal (compare figures 5.4 and 5.5). These spikes are due to electronic noise during the measurements, and contribute nothing meaningful to the data. Firstly the difference in magnitude between each two consecutive data points is determined. The maximum spike from the data set is then identified, and the unwanted data points are defined as data points where a spike larger than 5% of the maximum spike occurs. In essence data points which lead to an unnaturally high gradient are identified and discarded, being replaced by taking a running average of remaining data points adjacent to the removed data point. The number of data points used in calculating this average is chosen to be equal to the maximum number of adjacent data points that were removed. It was of course possible to simply take a running average over a fixed number of data points for the whole data set, and smooth the signal in this manner. This, however, would not totally remove the unwanted data points, and would factor them in the smooth signal leaving a small spike or bump in the final signal.

4) This zeroed and smoothed data is multiplied by a calibration factor to determine the stress in both bars. This calibration factor is determined theoretically using the method described in section 4.4 and then refined using the momentum method and the experimental parameters in the main spreadsheet.

5) As described in section 4.4, the pulses need to be shifted so that the data captured represents the pulses at the sample-bar interfaces. This is done by using the calibration runs to calculate the sound wave speed of every bar, which is in the order of 5000 ms^{-1} (see figure 5.3). Using these values and the measured distances from each strain gauge to the sample interface, the number of data points each pulse needs to be shifted can be determined.

6) Using these shifted stresses and the theory described in section 4.4, the stress-strain, and strain rate-strain history can be determined.

5.3 Results and Discussion for copper

The strain rate-strain response of copper tested is shown in figure 5.6, and corresponds to the stress-strain responses showed in figure 5.7. In the case of sample T2S1c the striker velocity oscilloscope did not record the time, and thus analysis of this sample was not possible. From figure 5.6, it can be seen that the lower strain rate (S1) was in the order of 700 s^{-1}, while the maximum higher strain rate (S2) was in the order of 1550 s^{-1}. This corresponds to the objective that the higher strain rate should be roughly double that of the lower strain rate. The samples deformed at the lower strain rate experienced a trapezoidal type of strain rate–strain curve in which much of the straining occurred at a constant strain rate. When the samples were deformed at a higher strain rate, a shorter striker bar was used with a larger impact velocity. The shorter compressive pulse acting on the samples gave rise to a strain rate–strain curve in the form of a parabola, rising to a maximum and then decreasing, with no plateau region of constant strain rate. Pulse shaping techniques have been employed in the past by other researchers to try and obtain more constant strain rates. This involves the placing of a soft ductile material between the striker and input bar during impact. For a full description of pulse shaping the reader may consult Gray (1985, p466). Although some experimentation with pulse shaping techniques were done with some of the sample sets, the resulting effect is not considered to be relevant, and is beyond the scope of the current project.

The repeatability of the results is satisfactory in the case of the annealed samples (T1 and T2), but is very poor in the case of the as-received samples (T0). This is most likely due to the fact that samples were removed from the shaped charge liner at random locations and had undergone different amounts of deformation during manufacturing resulting in different microstructural properties. Annealing of samples resulted in a much larger degree of homogeneity. This uniformity of results after annealing indicates that the stress-strain properties of the copper after annealing are not strongly dependent on its prior straining history. Also, the results obtained for the two different annealing procedures (T1 and T2) are very similar, indicating that annealing at different temperatures has no significant influence on the SHPB testing results.

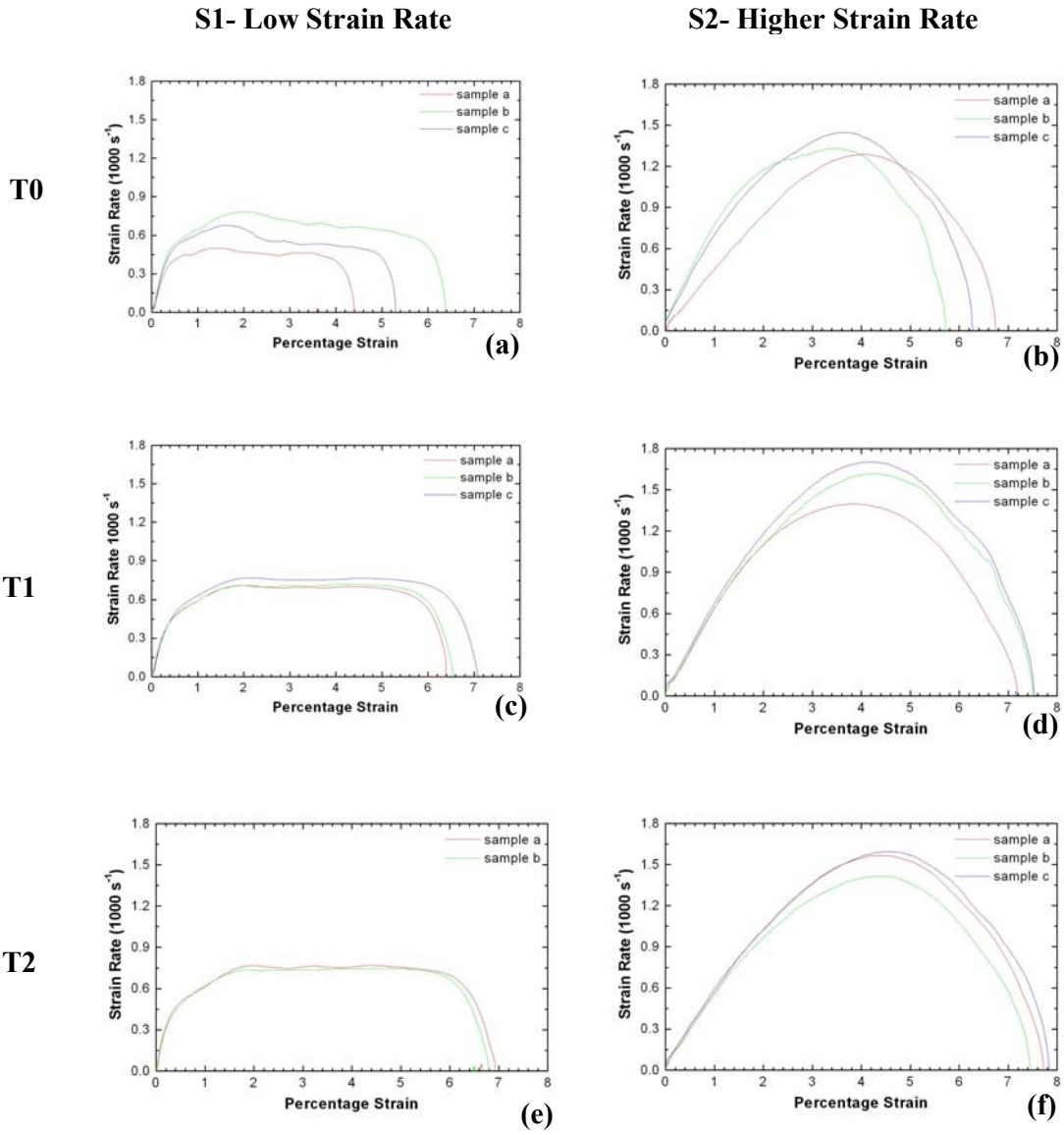

Figure 5.6: Strain rate-strain results of deformed copper **(a)** Sample T0S1, **(b)** Sample T0S2, **(c)** Sample T1S1, **(d)** Sample T1S2, **(e)** Sample T2S0, **(f)** Sample T2S2.

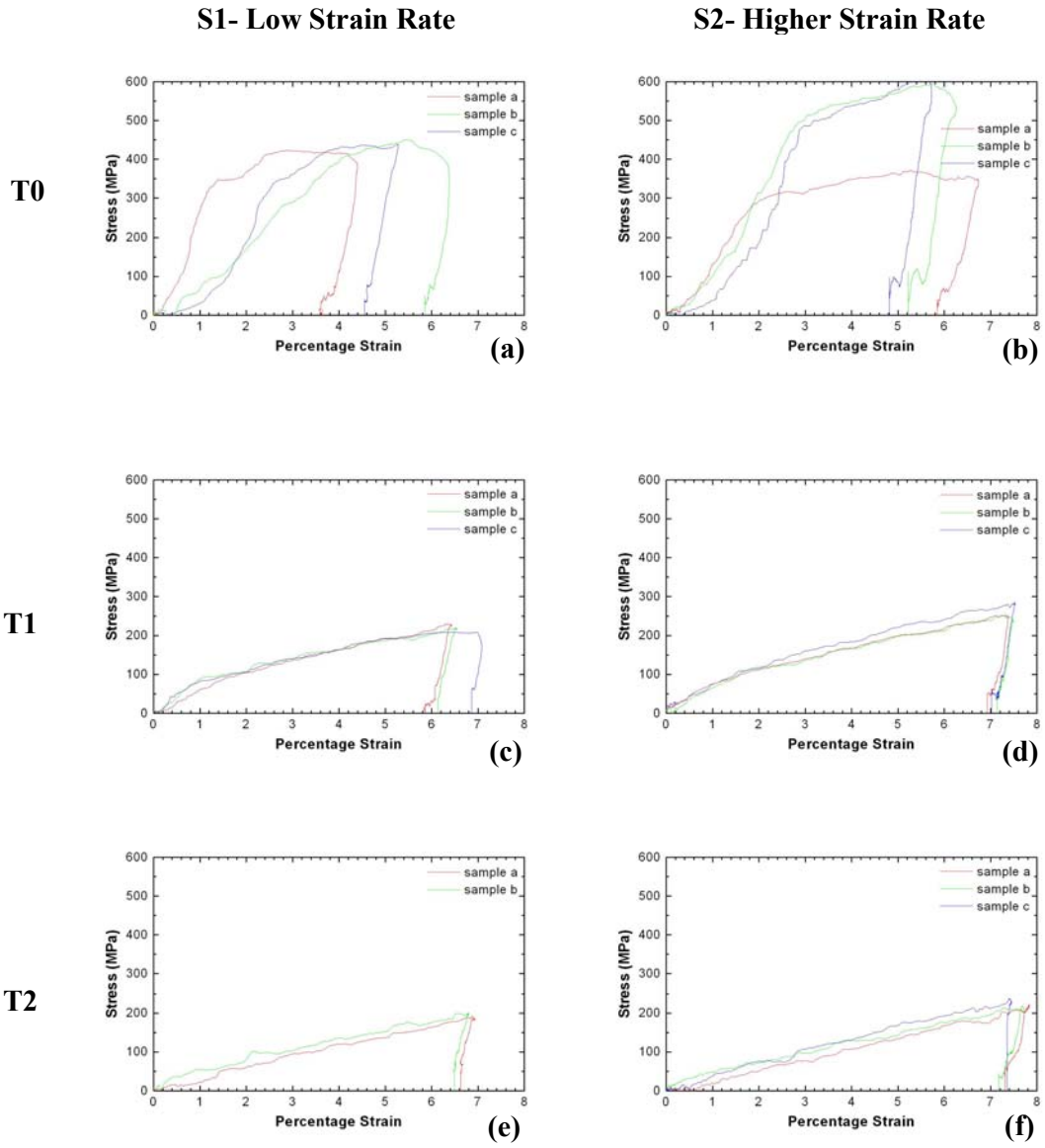

Figure 5.7: Stress-strain results of deformed copper **(a)** Sample T0S1, **(b)** Sample T0S2, **(c)** Sample T1S1, **(d)** Sample T1S2, **(e)** Sample T2S0, **(f)** Sample T2S2.

Table 5.4: Average stress reached at 5% strain in the case of copper.

	Average Stress at 5% strain (MPa)	
	S1	**S2**
T0	433	504
T1	190	197
T2	141	147

Table 5.4 shows the average stress in the various samples at 5% strain, as from figure 5.7. As the stress was lower in the annealed samples it is evident that the annealed samples are much softer and thus more ductile than the unannealed samples, as was expected. It must be noted that although the stress obtained in samples annealed at 500˚C was lower than that of the samples that was annealed at 300˚C, the difference was slight when compared to the difference in annealing temperature (see figure 5.8). This difference was much less than for instance the difference overall between the annealed and unannealed samples. This should be considered when deciding on the annealing procedure for manufacturing copper shaped charges, as the gain in penetration performance might be offset by manufacturing cost. The samples strained at the higher strain rate appear to show a slight increase in the magnitude of stress experienced when compared to the equivalent samples strained at the lower strain rate (see table 5.4). This increase, however, is very small.

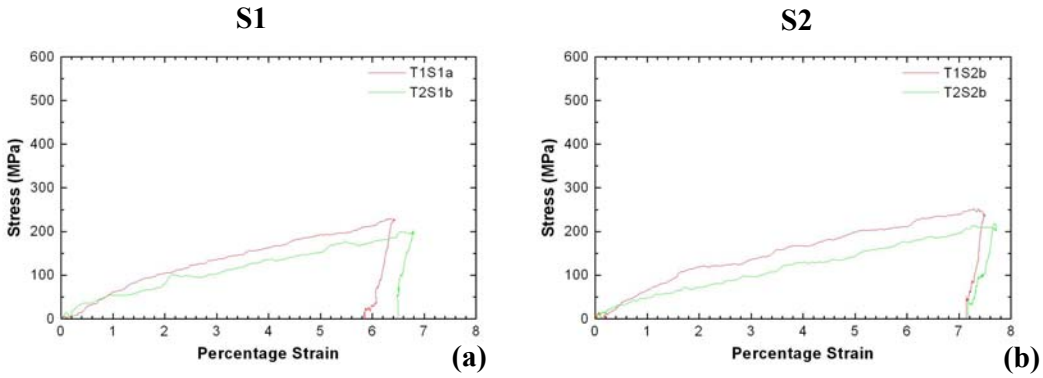

Figure 5.8: Comparison of copper stress-strain response to different annealing conditions **(a)** Lower strain rate, **(b)** higher strain rate.

Since the stress–strain curve of a sample is dependent on the materials heat treatment and impurity concentrations, it may be of limited value to compare the stress–strain curves obtained here to stress–strain curves in the literature. However, if these conditions are kept in mind, certain trends can still be observed. Comparative stress-strain graphs are shown in figures 5.9 and 5.10.

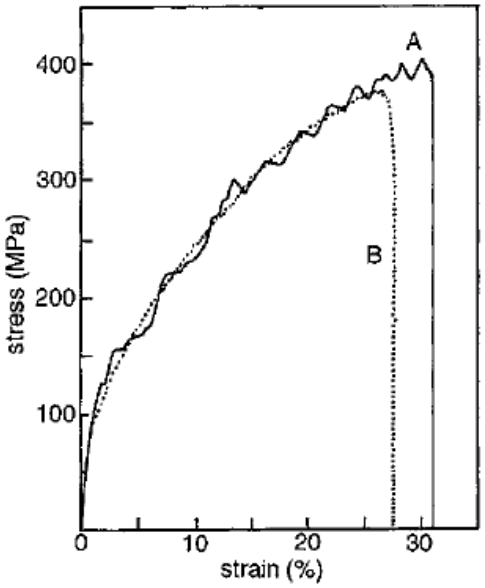

Figure 5.9: Stress–strain graph of OFHC copper (Parry *et al*., 1995)

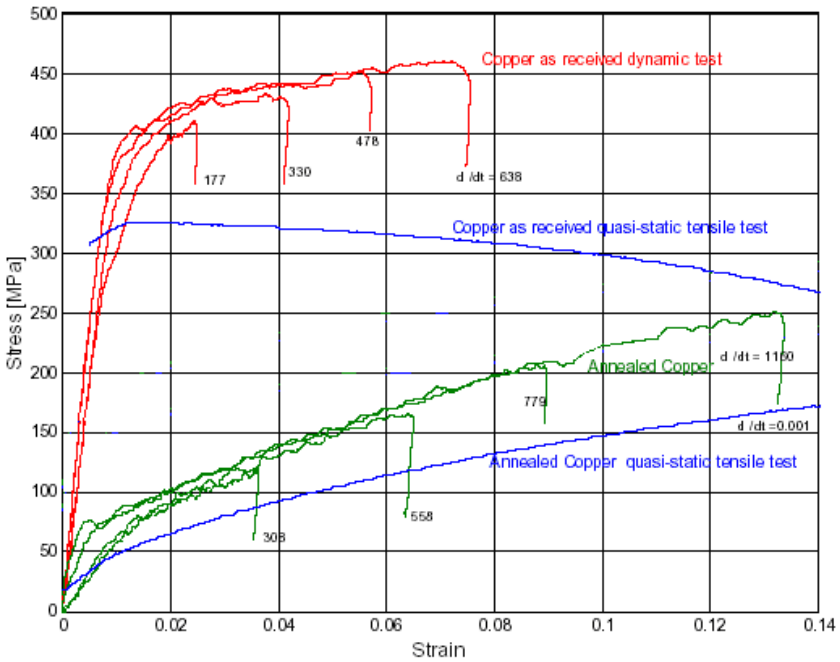

Figure 5.10: Stress–strain graph of as-received and annealed copper (Marais *et al*., 2004).

Firstly, comparing the figures themselves and taking note of the different scales on the strain axes, it is seen that the stress–strain curve in figure 5.9 corresponds roughly to the data for the annealed samples in figure 5.10. Figure 5.10 shows the same very large difference in the behaviour of annealed copper compared to unannealed (as-received) samples as also found in this work, although the history of the as-received samples for figure 5.10 is not known. The stress–strain data obtained in this study is in fact very similar to that in figure 5.10, except for the variability in the results for the unannealed samples. It is interesting to note that although the data obtained in figure 5.10 was recorded at different strain rates, the material response does not appear to be influenced by the strain rate, both for annealed and unannealed samples. As can be seen in figure 5.11(a,b), the results of this study also do not show a strain rate dependence, although it should be mentioned that the strain rate could not be varied considerably e.g. an order of magnitude. The results of this study do, however, show an influence from the annealing temperature, with the samples annealed at 500°C being slightly softer. This is shown in figure 5.11(b).

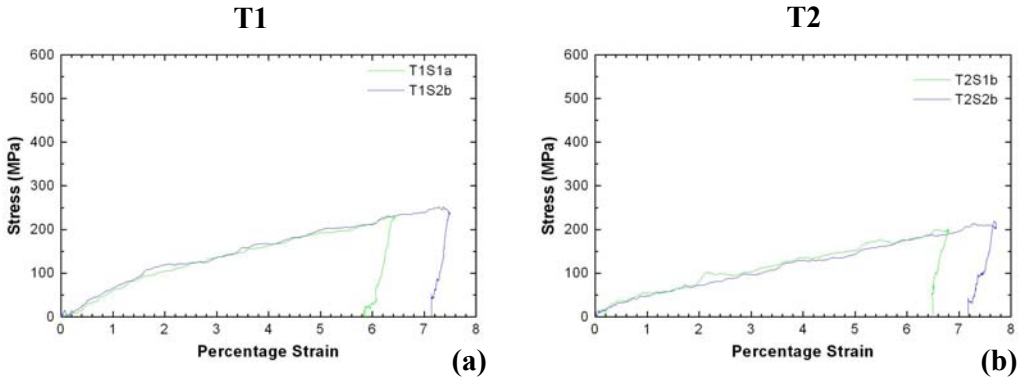

Figure 5.11: Comparison of copper stress-strain response to different strain rates **(a)** T1: annealed at 300 °C for 30 min , **(b)** T2: annealed at 500 °C for 30 min.

Figure 5.12 gives the theoretically predicted stress-strain curves using the Johnson-Cook constitutive model (Meyers, 1992, p328)

$$\sigma = (\sigma_0 + \beta\varepsilon^n)(1 + C\ln\dot{\varepsilon}) \qquad \textbf{(5.1)}$$

were $\sigma_0 = 90$ Mpa, $\beta = 292$ MPa, $n = 0.31$ and $C = 0.025$. Three strain rate values of 10^{-4} s^{-1} (quasi-static), 700 s^{-1} and 1550 s^{-1} were used. The full Johnson-Cook model includes a term for temperature which has been excluded as the test was performed at room temperature. The Johnson-Cook model results are in good agreement with the experimental results for the samples annealed at the higher temperature (T2) (see figure 5.11(b)), and show that for the two strain rates achieved no significant difference in stress-strain curves is to be expected.

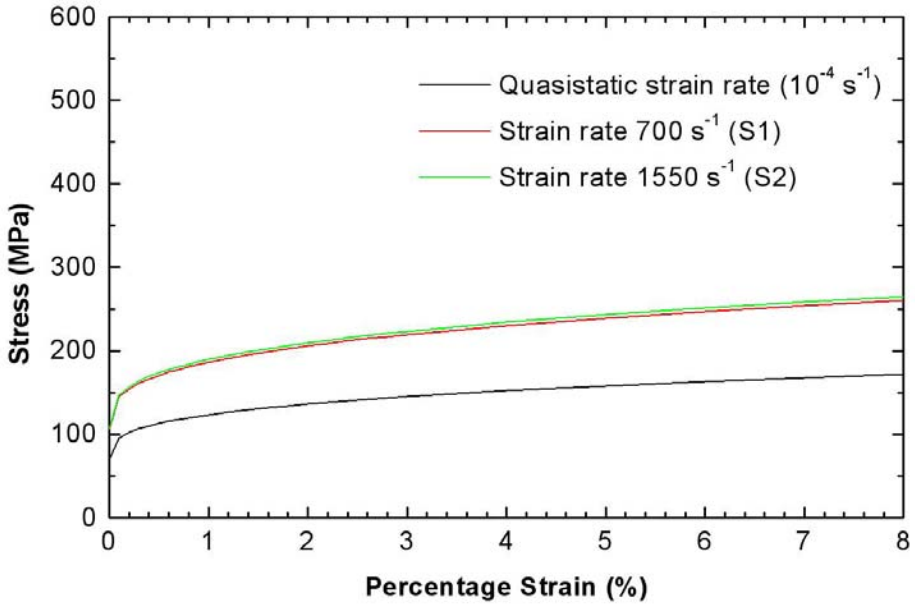

Figure 5.12: Results of Johnson Cook constitutive model.

An observation was made that the total sample strains predicted by the analysis of the SHPB results did not always correspond to the actual measured values of the samples, calculated using equation 4.6. These strains are compared for the different annealing conditions in table 5.5. The measured strain values indicated that more deformation took place than was predicted by the model, particularly in the case of the annealed samples. One possible explanation is that the annealed samples experienced two compressive pulses in the SHPB instead of only one, as suggested by a measured/predicted ratio of strains of about two (see table 5.5). The annealed samples were much softer than the unannealed samples, which resulted in most of the pulse in

the Hopkinson input bar being reflected, and only a small fraction being transmitted. The lack of transmitted momentum may have prevented the output bar from disengaging with the sample before the reflected pulse in the input bar returned to act on the sample for a second time. Nemat-Nasser (1985, p477) provides a full description of double straining, and ways to prevent it in future work.

Table 5.5: Measured and predicted strain of copper samples. The striker velocity of T2S1c could not be determined due to equipment failure, hence the analysis could not be completed.

Sample	Measured strain (%)	Predicted strain (%)	Measured/ Predicted ratio
T0S1a	4.27	4.39	0.98
T0S1b	10.08	6.37	1.58
T0S1c	4.33	5.27	0.82
T0S2a	6.47	6.74	0.96
T0S2b	6.49	6.24	1.04
T0S2c	7.78	5.72	1.36
Average for unannealed (T0) samples:			**1.16**
T1S1a	12.75	6.38	1.99
T1S1b	13.15	6.50	2.02
T1S1c	14.82	7.00	2.12
T1S2a	11.51	7.19	1.60
T1S2b	12.45	7.48	1.66
T1S2c	13.81	7.52	1.84
Average for annealed (T1) samples:			**1.87**
T2S1a	16.87	6.90	2.44
T2S1b	12.39	6.77	1.83
T2S1c	-	-	-
T2S2a	13.63	7.70	1.77
T2S2b	14.00	7.82	1.79
T2S2c	13.15	7.43	1.77
Average for annealed (T2) samples:			**1.92**

Although the increased strain in these samples will have increased the number of dislocations in the annealed samples, the results are still considered viable because even if the samples were effectively deformed twice, both events would have been from very similar stress pulses in the input bar (recall that most of the pulse was reflected), and thus have resulted in similar strain rate deformations. Whereas the total strain is affected strongly, the strain rate would be affected weakly. The strain rate calculated using the model is thus still considered relevant. In addition, although the annealed samples will not be directly comparable to the unannealed samples in terms of dislocation densities, the differently annealed samples can still be compared to one another.

5.4 Results and Discussion for molybdenum

The strain rate-strain responses of molybdenum tested are shown in figure 5.13, and correspond to the stress-strain responses shown in figure 5.14. The reader should note that the results of T0S2a and T2S1c are not shown. This was because the striker velocity oscilloscope did not record the time on both occasions, and thus analysis of the samples was not possible. Due to the high pressure used in the gas gun, the diodes of the striker velocity speed trap system would be dislodged during the firing of the previous sample. If this was not noticed (as happened in these two cases), the striker velocity oscilloscope would not record the time of the following sample, and thus analysis of this samples would not be possible. From figure 5.13, it can be seen that the lower strain rate (S1) was in the order of 700 s^{-1}, while the higher strain rate (S2) was in the order of 1650 s^{-1}. The samples deformed at the lower strain rate experienced a trapezoidal type of strain rate–strain curve, while the samples deformed at the higher strain rate with a shorter striker bar showed a strain rate–strain curve in the form of a parabola. Good repeatability of the results was obtained for the annealed samples. This was not the case for the unannealed samples. This was most likely due to the fact that samples were removed from the shaped charge liner at random locations and had undergone different amounts of deformation during manufacturing, resulting in different microstructural properties. Annealing of samples resulted in a large degree of homogeneity indicating that the stress-strain properties of the annealed molybdenum are not strongly dependent on its prior straining history.

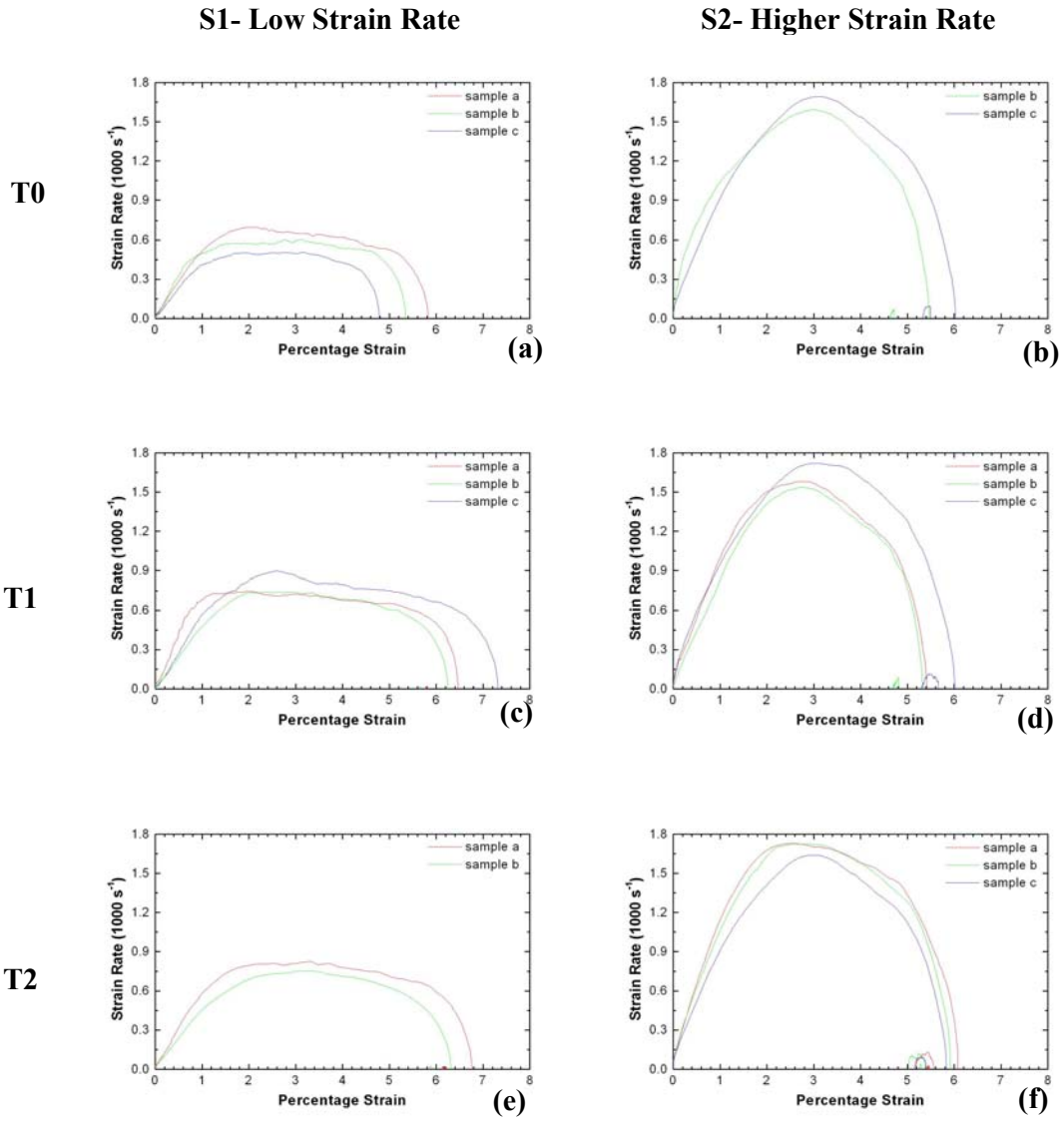

Figure 5.13: Strain rate-strain results of deformed molybdenum. **(a)** Sample T0S1, **(b)** Sample T0S2, **(c)** Sample T1S1, **(d)** Sample T1S2, **(e)** Sample T2S0, **(f)** Sample T2S2.

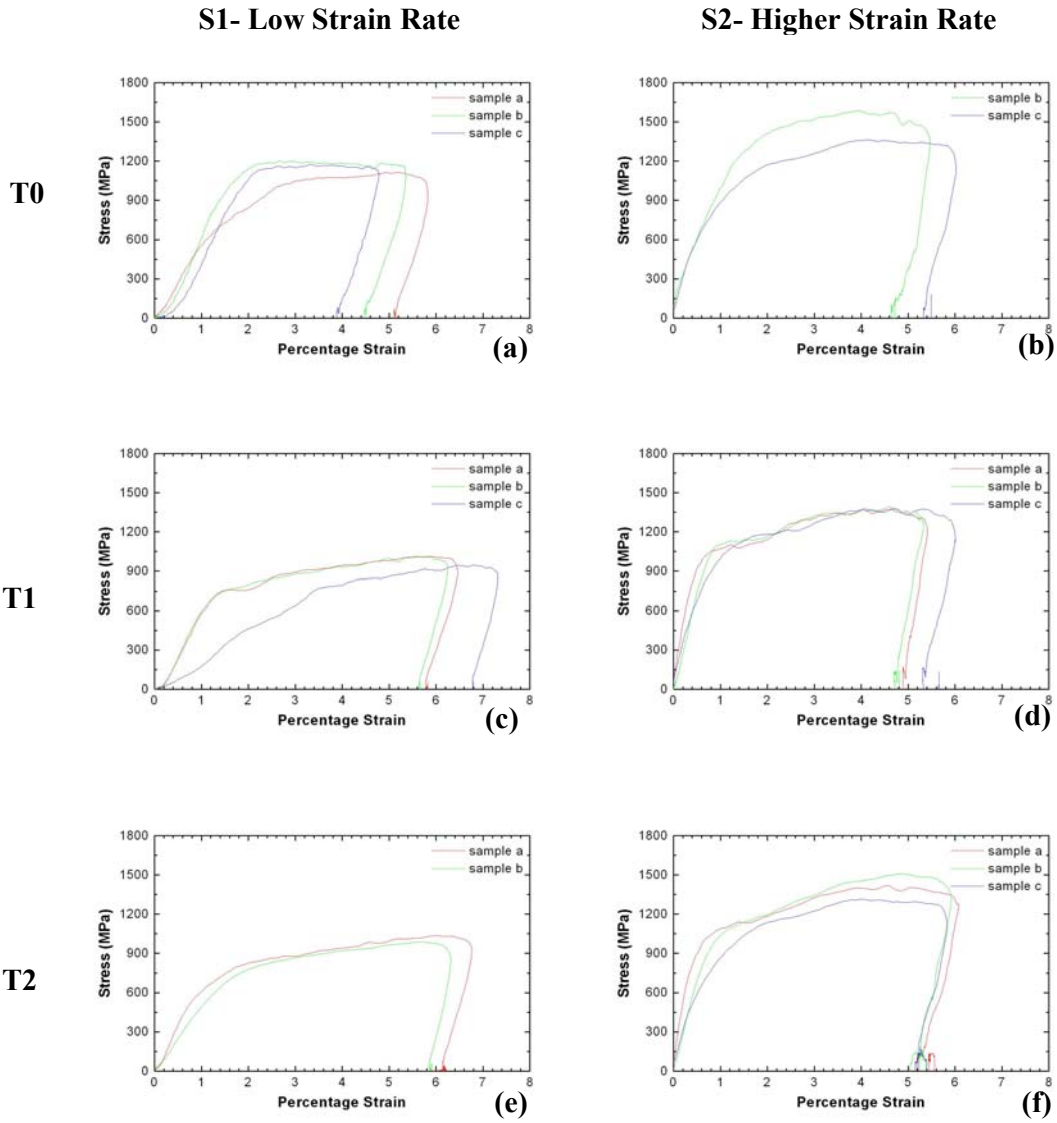

Figure 5.14: Stress - strain results of deformed molybdenum. **(a)** Sample T0S1, **(b)** Sample T0S2, **(c)** Sample T1S1, **(d)** Sample T1S2, **(e)** Sample T2S0, **(f)** Sample T2S2.

Table 5.6 shows the average stresses reached by the molybdenum samples during deformation.

Table 5.6: Average stress reached at 5% strain in the case of molybdenum.

	Average Stress at 5% strain (MPa)	
	S1	**S2**
T0	1140	1421
T1	946	1337
T2	979	1397

Notice that there is not a extremely large decrease in the stress between the annealed and unannealed samples, and between the annealed samples, the difference is neglible (see figure 5.15). This indicates that the samples are of similar hardness and thus have a similar microstructure. This may indicate that sufficient grain growth has not taken place during annealing (see chapter 6). The samples strained at the higher strain rate show a significant increase in the magnitude of stress experienced when compared to the equivalent samples strained at the lower strain rate.

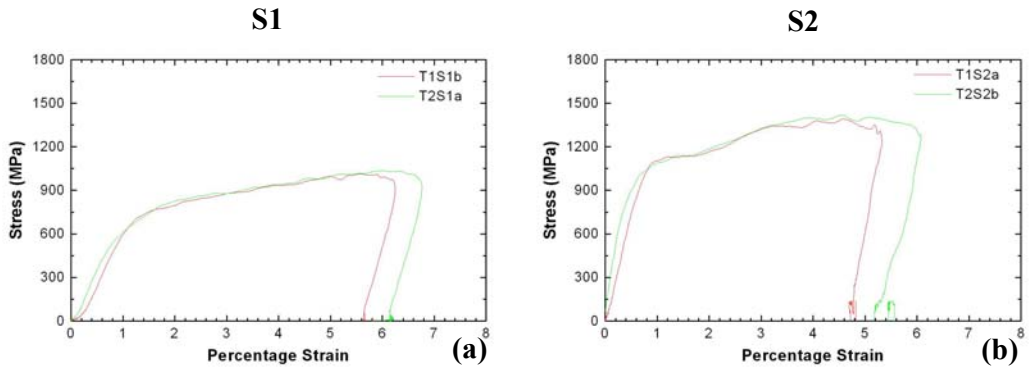

Figure 5.15: Comparison of molybdenum stress-strain response to different annealing conditions. **(a)** Lower strain rate, **(b)** higher strain rate.

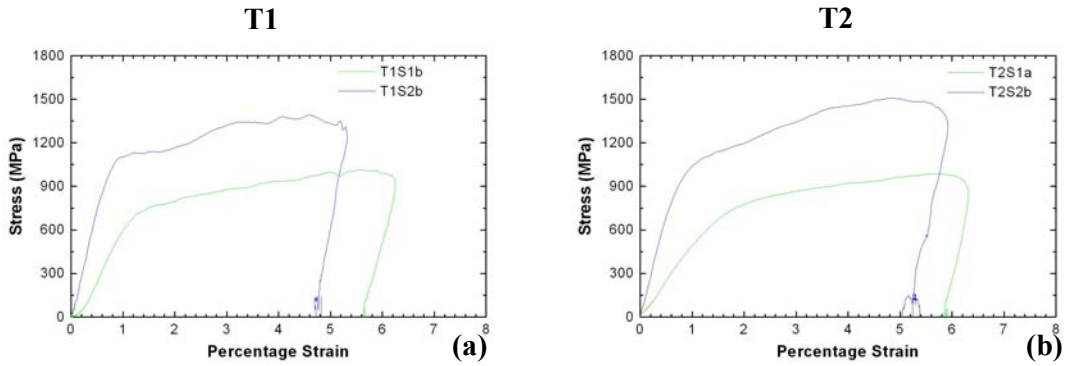

Figure 5.16: Comparison of molybdenum stress - strain response to different strain rates, **(a)** annealed at 1200°C for 30 min, **(b)** annealed at 1200°C for 3h.

Figure 5.16 shows the strong strain rate dependency of the yield strength which is typical of BCC materials (Gray, 1985, p472). This strong strain rate dependency of the yield strength can also be seen in figure 5.17 taken from the literature. The stress-strain curve marked (e) in figure 5.17 compares well to the lower strain rate results in this study, in terms of stresses achieved.

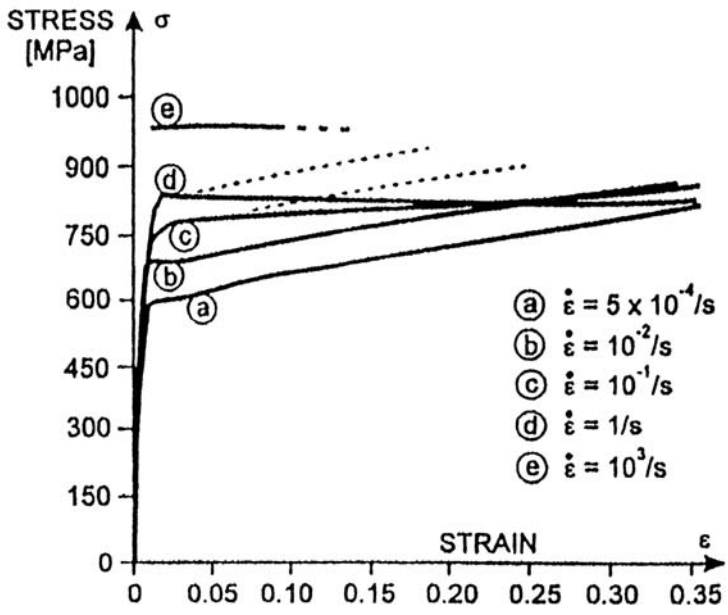

Figure 5.17: An example of a stress-strain curve of molybdenum (Lightenberger *et al.,* 1996).

The measured strain as well as the predicted strain is shown in table 5.7. A ratio between these values is also given. Although the amount of strain experienced by the sample were slightly lower than expected in the case of the unannealed samples, excellent correspondence between the results were obtained for the annealed samples.

Table 5.7: Measured and predicted strain of molybdenum samples. The striker velocity of T0S2a and T2S1c, could not be determined due to equipment failure, hence the analysis could not be completed.

Sample	Measured strain (%)	Predicted strain (%)	Measured/ Predicted ratio
T0S1a	4.36	5.78	0.75
T0S1b	4.13	5.34	0.77
T0S1c	3.51	4.78	0.73
T0S2a	-	-	-
T0S2b	5.01	5.46	0.92
T0S2c	3.85	6.02	0.64
Average for unannealed (T0) samples:			0.76
T1S1a	6.53	6.46	1.01
T1S1b	6.91	6.24	1.12
T1S1c	4.65	7.3	0.64
T1S2a	6.58	5.41	1.22
T1S2b	5.62	5.32	1.06
T1S2c	6.20	5.99	1.04
Average for annealed (T1) samples:			1.02
T2S1a	6.8	6.75	1.01
T2S1b	5.68	6.31	0.90
T2S1c	-	-	-
T2S2a	7.12	6.07	1.17
T2S2b	6.66	5.91	1.13
T2S2c	5.43	5.83	0.93
Average for annealed (T2) samples:			1.03

5.5 Comparison between copper and molybdenum

Both sets of data show the expected behaviour for their respective materials, and compares reasonably well with results that are available in the literature. Even though the materials are fundamentally different due to a different crystal structure there are some similarities in how each material responds to annealing and deformation.

Both materials tested show a difference in repeatability between annealed and unannealed samples. This has been contributed to the fact that samples were removed from the shaped charge liner at random locations and had undergone different amounts of deformation during manufacturing resulting in different microstructural properties. Annealing of samples resulted in a much larger degree of homogeneity. This uniformity of results after annealing indicates that the stress-strain properties of both materials after annealing are not strongly dependent on their prior straining history. It also suggests that a final anneal after forming of the shaped charge liner should be carried out.

It does seem, however, that the difference in repeatability between the annealed and unannealed samples for molybdenum are not as pronounced as in the case of the copper samples. This might indicate that the High Energy Rate Manufacturing (HERF) process used for the molybdenum liners leaves a more homogeneous microstructure when compared to that of the cold worked copper liners. This is, however, of little importance in shaped charge liner performance, seeing that all liners will have undergone heat treatment. The molybdenum samples showed no signs of double straining. This gives credibility to the theory that the annealed copper was too soft to obtain accurate results without using special SHPB techniques (Nemat-Nasser, 1985, p477). In the case of both materials, the different annealing cycles did not make a significant difference. It would thus make economic sense for a manufacturer, to use the lower temperature or time when annealing liners.

One major difference between the copper (FCC) and molybdenum (BCC) results is that the copper showed no strain rate dependency whereas the molybdenum did.

Although standard data analysis techniques were used, the accuracy in the results obtained using the spreadsheet in determining the strain undergone by the samples can be improved upon. This is attributed to irregularities in the shape of the samples. Samples with very close tolerances are required to perform accurate SHPB measurements (Gray, 1985, p471). This was difficult to achieve, because of the very nature of cutting samples from an actual engineering structure or object. It is believed that more accurate results would have been achieved had the samples been stock metal. None the less, the results are considered to be acceptable for the purpose of this study.

5.6 References

Askeland D.R. **[1998]** *The Science and Engineering of Materials*, Stanley Thornes Ltd.

Gray G.T. **[1985]** *Classic Split – Hopkinson Pressure Bar Testing* in *ASM Handbook, Vol 8, Mechanical testing and Evaluation* (Kuhn H. and Medlin D.), ASM international.

Lichtenberger A., Verstraete N., Salignon D., Daumas M.T. and Collard J. **[1996]** *16th International Symposium on Ballistics*, San Francisco, USA. p49.

Marais S.T., Tait R.B., Cloete T.J. and Nurick G.N. **[2004]** *Latin American Journal of Solids and Structures* **1** p319.

Meyers M.A. **[1994]** *Dynamic Behavior pf Materials* , John Wiley and Sons Inc.

Meyers M.A., Andrade U.R. and Chokshi A.H. **[1995]** *Metallurgical and Materials transactions* **26A** p2881.

Nemat-Nasser S. **[1985]** *Recover Hopkinson Bar Techniques* in *ASM Handbook, Vol 8, Mechanical testing and Evaluation* (Kuhn H. and Medlin D.), ASM international.

Parry D.J., Walker A.G. and Dixon P.R. **[1995]** *Measurement Science and Technology* **6** p443.

Chapter 6

Determination of sample grain size

6.1 Introduction

As mentioned in chapters 2 and 3, the size of grains present in shaped charge liner material is of vital importance when considering the penetration potential of the jets. Although different techniques exist to determine the grain size of a particular sample e.g. using X-ray determination (Exner, 1983, p613), the most commonly used method is to first polish and etch the sample surface and then to examine it using an optical microscope (Exner, 1983, p583). For this reason it was decided to examine samples using an optical microscope, and for a comparison, the samples were also examined using a Scanning Electron Microscope (SEM) employing both a Secondary Electron Detector (SED) and a Backscattered Electron Detector (BSED). From these obtained images, the grain size would then be determined. The samples were also briefly examined using Atomic Force Microscopy (AFM), and in a SEM using an Electron Backscattered Diffraction (EBSD) detector.

6.2 Experimental

The experimental procedure to determine the grain size entailed four different process steps:

1. Polishing of the samples
2. Etching of the samples
3. Imaging of the samples

4. Measuring of the average grain size

These procedures are discussed in the following subsections.

6.2.1 Polishing of the samples

Sample surfaces were polished before etching. This was done to prepare a smooth surface for the actual etching process. To gain a reasonable idea of the three dimensional nature of the grains, the samples were sectioned and polished in two directions: one perpendicular to the direction of deformation in the Split Hopkinson Pressure Bar (SHPB), and one parallel to the direction of deformation (see figure 6.1). The surface perpendicular to the direction of the deformation is denoted as surface **x**, and the surface parallel to the deformation direction is denoted as **y**. From now on when referring to a sample the letters **x** or **y** will be added depending from which direction the sample is viewed. So if two images are labelled T2S0**x** and T2S0**y**, they are in fact images of the same sample, but imaged from two different viewing directions.

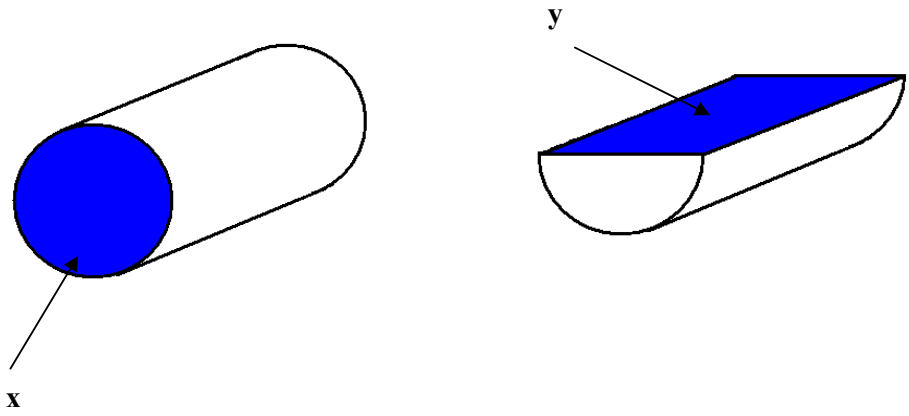

Figure 6.1: Surfaces of samples used to determine average grain size.

Polishing was performed using various grades of sandpaper followed by polishing with diamond suspension. The samples were polished as follows: 220 grit sandpaper was used to remove the surface layer (2-3 mm) of the sample. This was done to ensure that the image obtained was representative of the sample, and not due to some surface irregularity. The surface was then polished using progressively finer grits, ensuring that the surface damage caused by each grit was removed by the following grit. The finest grit used was 1200 grit. The sample was then polished using 6 μm, 3 μm, 1 μm and finally 0.25 μm diamond suspension.

6.2.2 Etching of the samples

Polishing prepared the sample surface for the etching process. The function of the etching solution is to produce contrast between the various grains. Due to the different crystal orientations of the grains, they are eroded at different rates, which causes this contrast. Various etching solutions for copper obtained from the literature, with etching times varying between 5 s and 3 min were tested. These solutions are listed below.

1. 50/50 solution of HNO_3/H_2O (Gurevitch *et al.*, 1993).

2. Equal volumes of H_2O, hydrogen peroxide, ammonium hydroxide (Schmidt *et al*., 1991)

3. 2g $K_2Cr_2O_7$, 1.5g NaCl, 8 ml H_2SO_4, 100ml H_2O (Gurevitch *et al*., 1993).

4. 5g $FeCl_3$, 10 ml HCl, 100 ml H_2O (Lee *et al*., 2002).

Solutions 1 and 3 proved to be the most successful. In addition to these solutions a pre-etch of 50/50 H_3PO_4/H_2O solution was used in an attempt to produce a even smoother surface before the actual etching took place (Tian *et al*., 2003). This, however, did not produce the desired results.

It was finally decided to use solution 1. However the solution described in the literature proved to etch too fast, making the process uncontrollable. It was decided to reduce the amount of acid in the solution. A final solution of 1 part HNO_3 to 2 parts H_2O proved to be satisfactory. The etching process was as follows: The polished sample was cleaned using household dishwashing detergent. Various other types of detergent, as well as acetone and ethanol were tried, but the dishwashing detergent proved to be the most effective cleaning agent. A small drop of the etching solution was placed on the sample surface. A few seconds later a reaction would be noticed on the surface in the form of gas bubbles. This time between the application of the etching solution and the start of the reaction is heavily dependent on the ambient temperature. At an ambient temperature of 25˚C this time is in the order of 20 seconds, but at a temperature of 15˚C it can be as long as two minutes. This reaction is thought to start when the thin oxide film present on the sample surface has been eroded by the solution allowing it to come into contact with the copper. At room temperature this reaction was allowed to continue for approximately 10 seconds, after which the samples surface was rinsed with water to remove any trace of the etching solution. The samples were then dried and stored until the actual examination of the surface took place.

The same basic procedure was used for the molybdenum samples in terms of the cleaning and preparation of the sample surface, but the etching solution consisted of 50 ml $FeCl_3$ solution (1.3g/ml H_2O), 25 ml HCl and 75 ml ethanol (Greaves and Wrighton, 1967, p 660). This solution, known as Hasson's tint etch for molybdenum, colours the grains depending on the grain orientation. Although it was the first solution to be tested for molybdenum it worked so well that it was used for the entire course of the study. A drop of the solution was placed on the sample surface, and washed off after an etching time of 45 seconds. No delay in the start of the reaction was witnessed as in the case of the copper, and no evidence of a chemical reaction in terms of gas bubbles was noticed.

6.2.3 Imaging of the samples

As mentioned in the introduction of this chapter, three main techniques were employed to obtain images of the sample grain structure: optical microscopy and SEM employing both a Secondary Electron Detector and a Backscattered Electron Detector.

Samples were first examined by means of a SEM (JEOL WINSEM JSM-6400) using a SED at the University of the Free State (UFS), but the grain structures were not evident. This was also the case when the samples were examined with a SEM (Philips XL30) at the Nelson Mandela Metropolitan University (NMMU). This failure was most likely due to the poor etching technique used at that time.

Better results were seen using a Reichert metallurgical microscope housed at the UFS. Unfortunately this microscope was not equipped with a camera, and thus images could not be recorded. Excellent images in terms of etching quality were obtained using an optical microscope at the NMMU, but this was marred by a mildew growth on one of the lenses which caused dark rings and spots on the photographs. It was then attempted to fit an old CCD camera on the microscope at the UFS, but unfortunately a large amount of resolution were lost due to the camera. Finally a digital camera (Nikon CoolPix 8400) was fitted to the microscope via an attachment made by the Department of Instrumentation at the UFS. This modification proved to be successful (see figure 6.2).

In the mean time the Microscopy Unit at the UFS obtained a Shimadzu SSX-550 SEM with both a SED and BSED. This SEM was used at 20 keV to obtain all the SEM images of the samples (see figure 6.3).

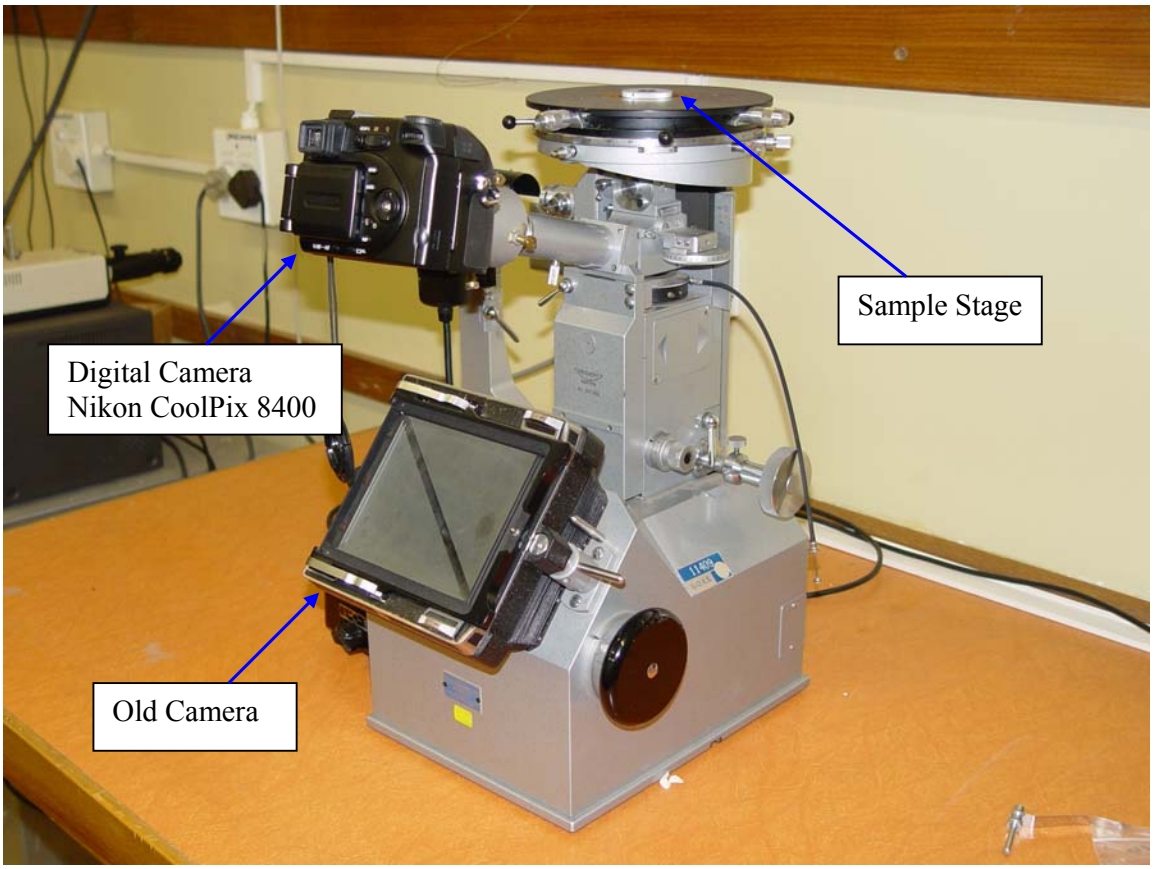

Figure 6.2: Modified optical Reichert metallurgical microscope used for grain size determination.

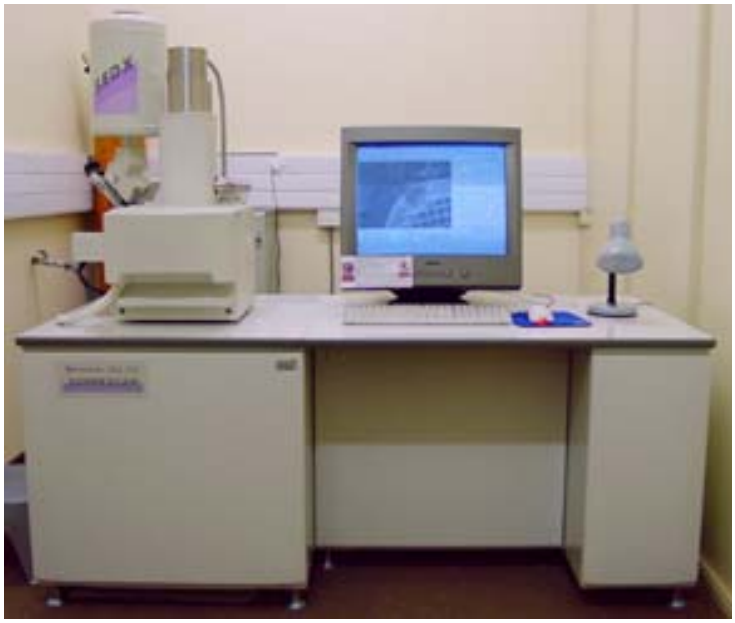

Figure 6.3: Shimadzu SSX-550 SEM used for grain size determination.

6.2.4 Determination of the average grain size per sample

One manner by which the grain size of a sample is defined is the designation of a grain size number index, which is specified in the American Society for Testing and Materials (ASTM). The ASTM grain size number is determined from

$$N = 2^{\eta-1} \qquad \textbf{(6.1)}$$

where N is the number of grains per square inch at a magnification x100 and η is the ASTM grain size number (Askeland, 1998, p99). Also available are comparison charts with different grain sizes printed on transparent screens. These charts are then compared to the image until a suitable match is found. Although this method is very useful for quality control purposes it cannot be used when the grain structure is not uniform, since the charts are based on a uniform structure. Nevertheless a determination of mean grain size is possible using either the Heyn or Jeffries procedure, given that a large number of grains are studied (Dehoff and Rhines, 1968, p243).

Using the Heyn method (see figure 6.4) one or more straight lines are drawn at random across the structural image. The number of points of intersection between these lines and the grain boundaries are counted. The total length of these lines, divided by the number of intersection gives the mean grain intercept length ℓ (Dehoff and Rhines, 1968, p239).

In the Jeffries method a circle of known area is drawn on the structure image. The number of grains which are lying entirely within the circle, and half the number of grains which are intersected by the circumference of the circle are then counted. The total area divided by the number of grains counted gives the average grain area A with the square root of this value $\sqrt{A}$ is denoted as grain size.

When comparing the two methods it is in practice easier to measure ℓ than $\sqrt{A}$, but due to the greater scattering in ℓ, a larger number of intercepts than grain areas have to be counted to attain the same level of accuracy. Despite this the Heyn method is still faster to perform. Another consideration that favour the Heyn method is that $\sqrt{A}$ is a quantity that lacks any direct physical significance. During the literature study for this project, it was also noted that the Heyn method was the method of choice for most researchers.

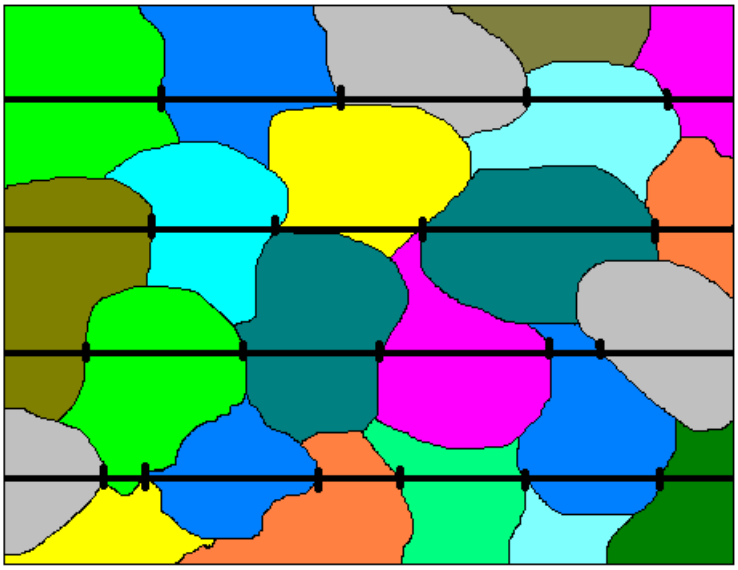

Figure 6.4: Heyn method for determining the number of grain intercepts.

In the case of nonequiaxed grains, usually caused by rolling or drawing, the standard Jeffries or Heyn method cannot be used. To gain a true representation of the grain size and shape, the measurements must be made in three mutually perpendicular directions, which form a orthogonal triplet. In the case of the Jeffries method it is necessary to obtain images of three mutually perpendicular surfaces of the sample. To perform the Heyn method only two such sections are necessary. This is because three mutually perpendicular directions must be considered, and it is possible to complete measurements in two orthogonal directions from one surface. The average grain size is calculated from the numbers of grains per unit of length in these three directions. By stating the results in these directions, some idea is gained of the grain shape (Dehoff and Rhines, 1968, p246).

6.3 Results and Discussion for copper

As mentioned in section 6.2, the samples were examined using a Scanning Electron Microscope (SEM) employing both a Secondary Electron Detector (SED) and a Backscattered Electron Detector (BSED), as well as using an optical microscope. Some differences in the quality of the images, and the information gained from them were noticed when using the different techniques. An example of all three techniques as applied on sample T2S0**y** is shown in figure 6.5.

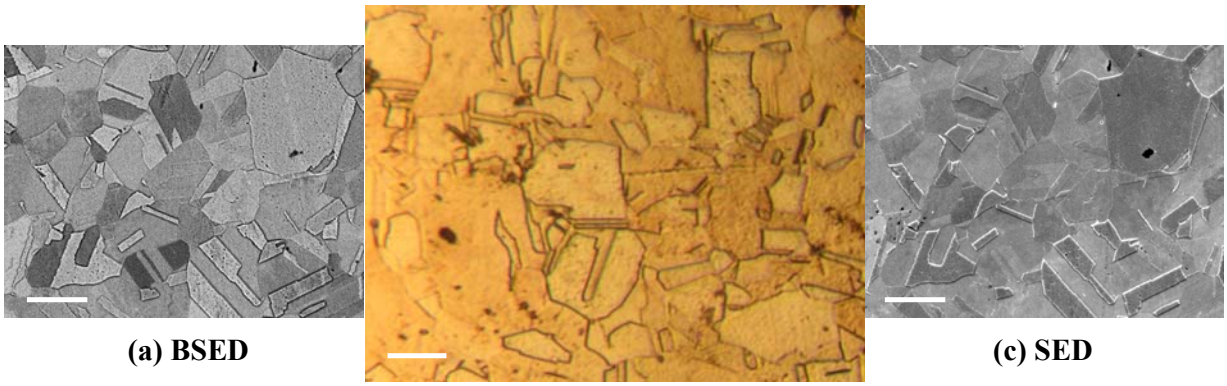

(a) BSED **(c) SED**

(b) Optical Microscope

Figure 6.5: Images of T2S0**y** using all three experimental techniques. (The scale bar is 20 μm in each case). **(a)** BSED: Backscattered Electron Detector in Shimadzu SSX-550 SEM. **(b)** Reichert metallurgical microscope with Nikon CoolPix 8400 digital camera. **(c)** SED: Secondary Electron Detector in Shimadzu SSX-550 SEM.

It can be clearly seen in figure 6.5 that the best images were obtained when using the BSED on the Shimadzu SSX-550 SEM. The BSED provides stronger contrast in the image than is the case when using the SED. This results in an image that contains more information regarding the grain structure. This can be clearly seen by comparing the lower left quadrant of the BSED and SED images and noticing that they are images of the same area on the sample surface. Although the image obtained using the modified optical microscope gives adequate information regarding the grain structure of the sample, it is believed that images of greater quality would have been obtained had a purpose built, modern metallurgical microscope been available. Some regions of the images obtained using the optical microscope has a mediocre focus. This is due to the fact that the optical microscope has a depth of focus that is smaller than that of

the SEM. Figure 6.6 shows BSED images of each copper sample investigated using the **x**-surface, or the surface perpendicular to the direction of deformation in the SHPB.

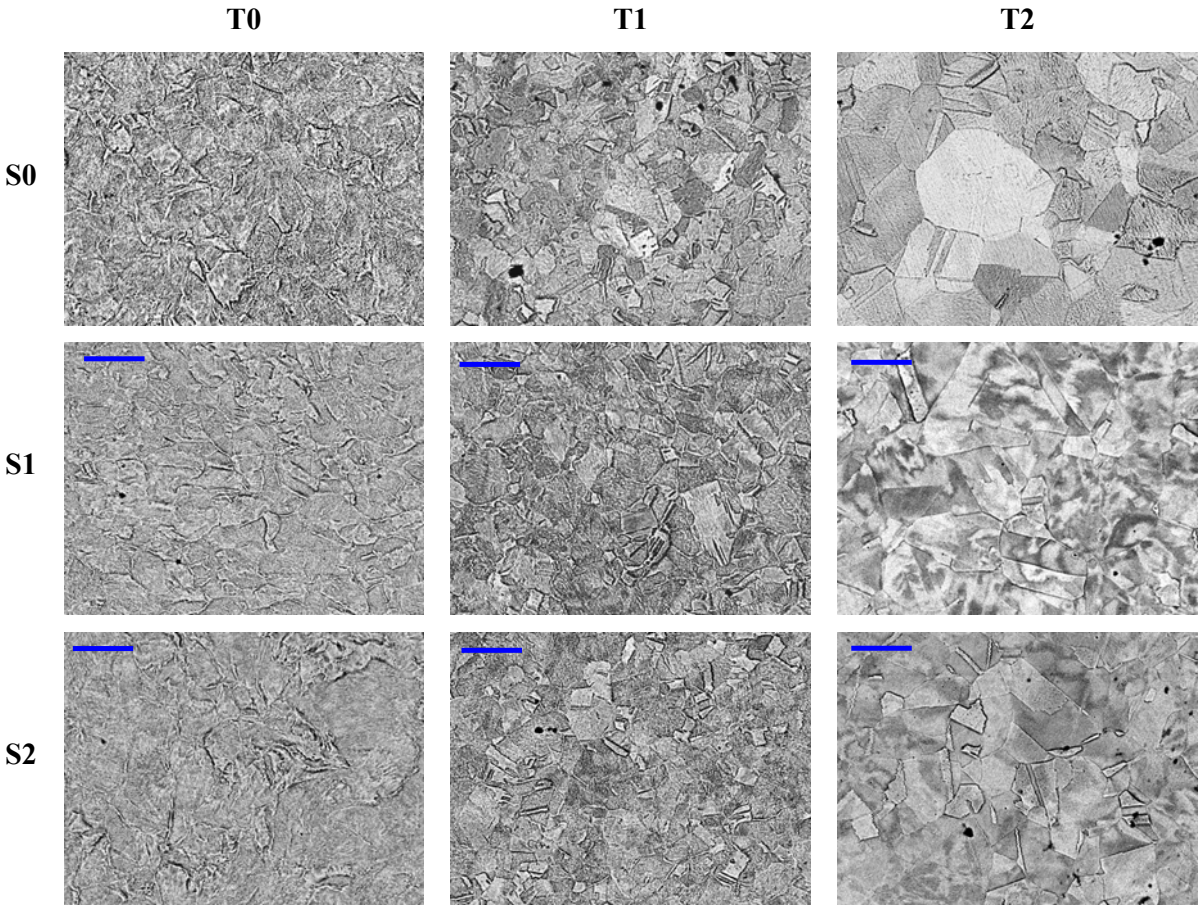

Figure 6.6: BSED images of copper samples viewed on the **x**-surfaces. (The scale bar is 20 μm in each image.)

When considering the evolution of the samples microstructure due to annealing, it is observed that the objective of this study to produce a small, recrystallised grain structure was met. The image of T0S0**x** shows the mangled microstructure caused by the forging of the shaped charge liner. T1S0**x** shows that the sample annealed at 300˚C has undergone recrystallisation, where as the sample that was annealed at 500˚C, T2S0**x** shows that some grain growth has taken place, but that the annealing time was too short or the temperature too low to produce a uniform grain structure (Dehoff and Rhines, 1968, p243). Annealing twins, discussed in section 3.1.3, can also be observed in some of the grains.

Similar observations can be made regarding the **y**-surface, or surface parallel to the direction of deformation in the SHPB. In figure 6.7 representative images of these surfaces are shown. Together with figure 6.6, an idea of the three dimensional nature of the copper samples grain structure can be established.

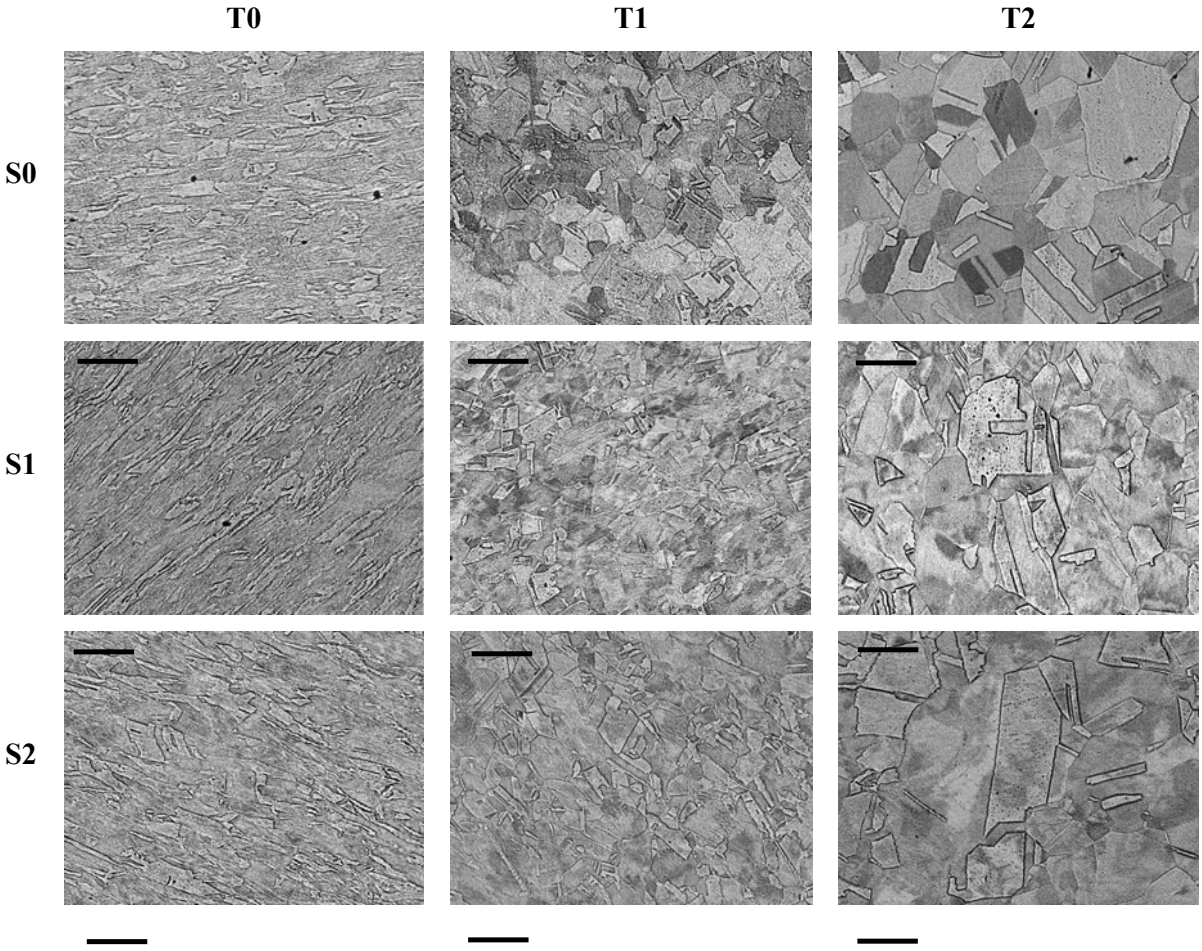

In T0S0**y** the same mangled microstructure can be seen as was observed in T0S0**x**, the only difference being that T0S0**y** shows a distinct grain orientation. This orientation of the grains indicates in which direction deformation of the liner material took place when the liner cone was manufactured as illustrated in figure 6.8.

Figure 6.7: BSED images of copper samples viewed on the **y**-surfaces (The scale bar is 20 μm in each image).

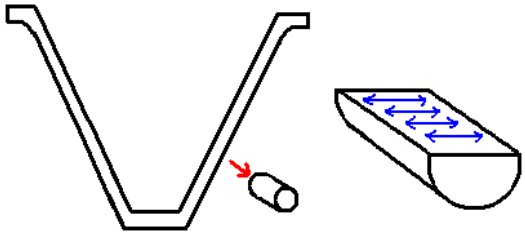

Figure 6.8: Direction of grain orientation in cone.

All three samples that were left unannealed show this grain orientation. Since there is no noticeable difference in the length, width and shape of these grains when comparing the T0S0**y**, T0S1**y** and T0S2**y** samples, this indicates that the amount of deformation that took place with the SHPB is substantially less than the amount of deformation that took place during the manufacturing of the liner. The other Y-images show similar traits than their corresponding X-images. The grain sizes for each sample obtained using the Heyn method is shown in table 6.1. For each sample two images from different areas on the sample surface with an area of 23000 μm^2 each were analysed. Six equally spaced lines were drawn across each surface, resulting in twelve lines per sample from which the number of grain boundary intercepts, and thus the grain size could be determined. From these twelve measurements, an average grain size for the sample was then calculated.

Table 6.1: Average grains size of copper samples calculated using the Heyn method.

Sample	Grain Size on X plane (µm)	Grain Size on Y plane (µm)
T0S0	Undetermined	Undetermined
T0S1	Undetermined	Undetermined
T0S2	Undetermined	Undetermined
T1S0	5	5
T1S1	5	5
T1S2	5	4
T2S0	8	7
T2S1	9	8
T2S2	9	10

Table 6.2 shows the minimum and maximum grain sizes obtained from each twelve number data set per sample.

Table 6.2: Minimum and maximum grain sizes obtained from each twelve number data set per sample.

Sample	Grain Size on X plane (µm)		Grain Size on Y plane (µm)	
	Min	**Max**	**Min**	**Max**
T1S0	4.0	6.6	4.4	7.5
T1S1	4.1	7.1	4.2	6.0
T1S2	4.3	6.2	3.3	4.4
T2S0	5.8	12.0	4.8	9.0
T2S1	6.4	10.8	5.8	10.0
T2S2	7.3	11.4	6.4	15

Due to the mangled structure of the unannealed samples, an accurate calculation of the grain size could not be made. It should be noted that certain factors influenced the accuracy, or the perceived accuracy of the measurements. The fact that the image quality is influenced by the amount of straining that took place decreases the ease and accuracy by which measurements can be made. This can be clearly seen when comparing the images of T2S0**y** and T2S2**y** in figure 6.7. The fact that the samples annealed at the lower temperature, or the T1 samples have not undergone grain growth or in some areas even complete recrystallisation also presents problems. These areas of mangled structure, left over from the as received material leads to a grain size larger than expected when the images are just examined. Similarly the presence of annealing twins in the samples annealed at the higher temperature or the T2 samples leads to a smaller average grain size than expected.

6.4 Additional techniques

In addition to the techniques shown in figure 6.5, two additional techniques were tested on the copper samples. In the first case sample T2S0**x** was examined using a Shimadzu SPM – 9600 Scanning Probe Microscope housed at the UFS to obtain an Atomic Force Microscopy (AFM) image. This image is shown in figure 6.9, and is of a mediocre quality when compared to the images already discussed.

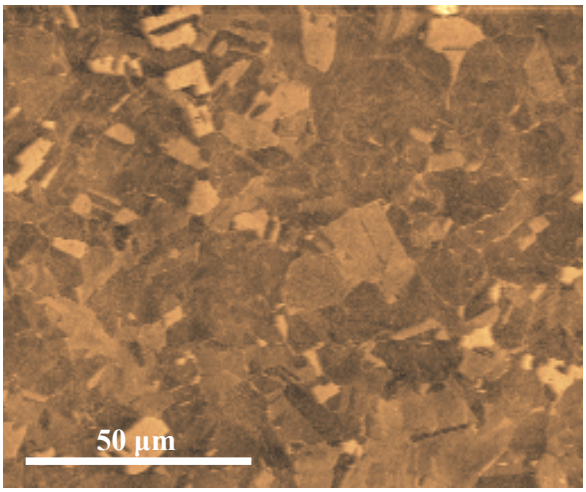

Figure 6.9: AFM image of T1S2**x**.

In the second case, Electron Backscattered Diffraction (EBSD) analysis of the copper samples was done using a LEO 1525 FE-SEM housed at the Council for Scientific and Industrial Research (CSIR) in Pretoria assisted by Ms. Sara Prins and Ms. Retha Rossouw. In EBSD, crystallographic information can be obtained from a sample examined using a SEM. A stationary electron beam strikes the tilted sample, and the diffracted electrons form a pattern on a fluorescent screen. This pattern can then be used to measure the crystal orientation, measure grain boundary misorientations and to distinguish between different materials or phases in the region from which it was generated. If this electron beam is then scanned across the sample, the resulting map will show the grain structure of the sample (Oxford Instruments Analytical, 2004). An EBSD map of T2S2**x** is shown in figure 6.10.

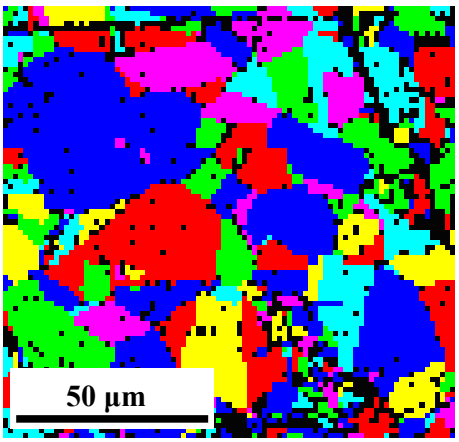

Figure 6.10: EBSD map of T2S2**x.** Black spots are orientations that could not be identified.

EBSD might prove useful if a more in-depth study of the grain structure is required. The technique does, however, have some drawbacks. Firstly the sample surface must be free of any oxide layer (which was found difficult to achieve) and secondly a quality scan can take a number of hours to complete, as at each data point a diffraction pattern must be collected and analysed. In favour of this technique, is that no etching of the sample is required

6.5 Results and Discussion for molybdenum

The samples were examined using a Scanning Electron Microscope (SEM) employing both a Secondary Electron Detector (SED) and a Backscattered Electron Detector (BSED). The samples were also examined using an optical microscope. Some differences in the quality of the images, and the information gained from them were noticed when using the different techniques. An example of all three techniques as applied on sample T2S2**x** is shown in figure 6.11. It is clear that the best results were obtained using the optical microscope.

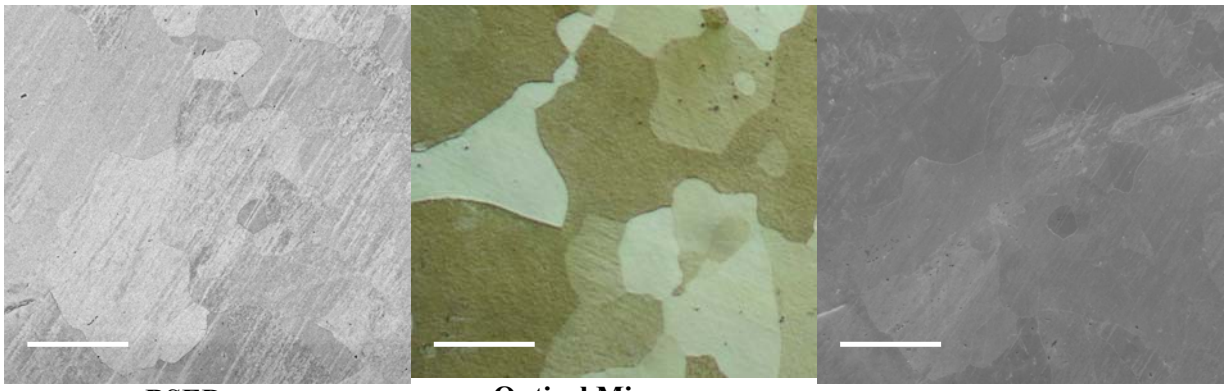

BSED **Optical Microscope** **SED**

Figure 6.11: Images of T2S2**x** using all three experimental techniques (The scale bar is 100 μm in each image.) **(a)** BSED: Backscattered Electron Detector in Shimadzu SSX-550 SEM. **(b)** Reichert metallurgical microscope with Nikon CoolPix 8400 digital camera. **(c)** SED: Secondary Electron Detector in Shimadzu SSX-550 SEM.

Figure 6.12 shows an image of each molybdenum sample investigated using the **x**-surface, or the surface perpendicular to the direction of deformation in the SHPB by means of the optical microscope. Only five of the samples were analysed, which show the general trend of the results. These samples correspond to those for which TEM was performed (see chapter 7). It can be seen that the original material (T0S0**x**) had a large, mangled grain structure. The annealing produced a recrystallised and significantly smaller grain structure (T2S0**x**), but no grain growth took place. To produce a structure where significant grain growth took place, a much higher annealing temperature would have to be used. A significantly longer annealing time could also be attempted, but seeing that T2 (3 hours) was already much longer than T1 (30 minutes) it is thought that this action will not give the desired results. No significant difference can be noticed between T1S1x, T2S0x and T2S2x. This indicates that the amount of strain achieved when the samples were strained using the Split Hopkinson Pressure Bar (SHPB) was too low to produce any significant difference in the resultant microstructure. The fact that the structure of T1S1x and T2S2x is similar further confirms that only recrystallisation took place and that the temperature used during annealing (1200˚C) was too low to produce different microstructures. This also explains the almost identical SHPB results for different annealing cycles in figure 5.15.

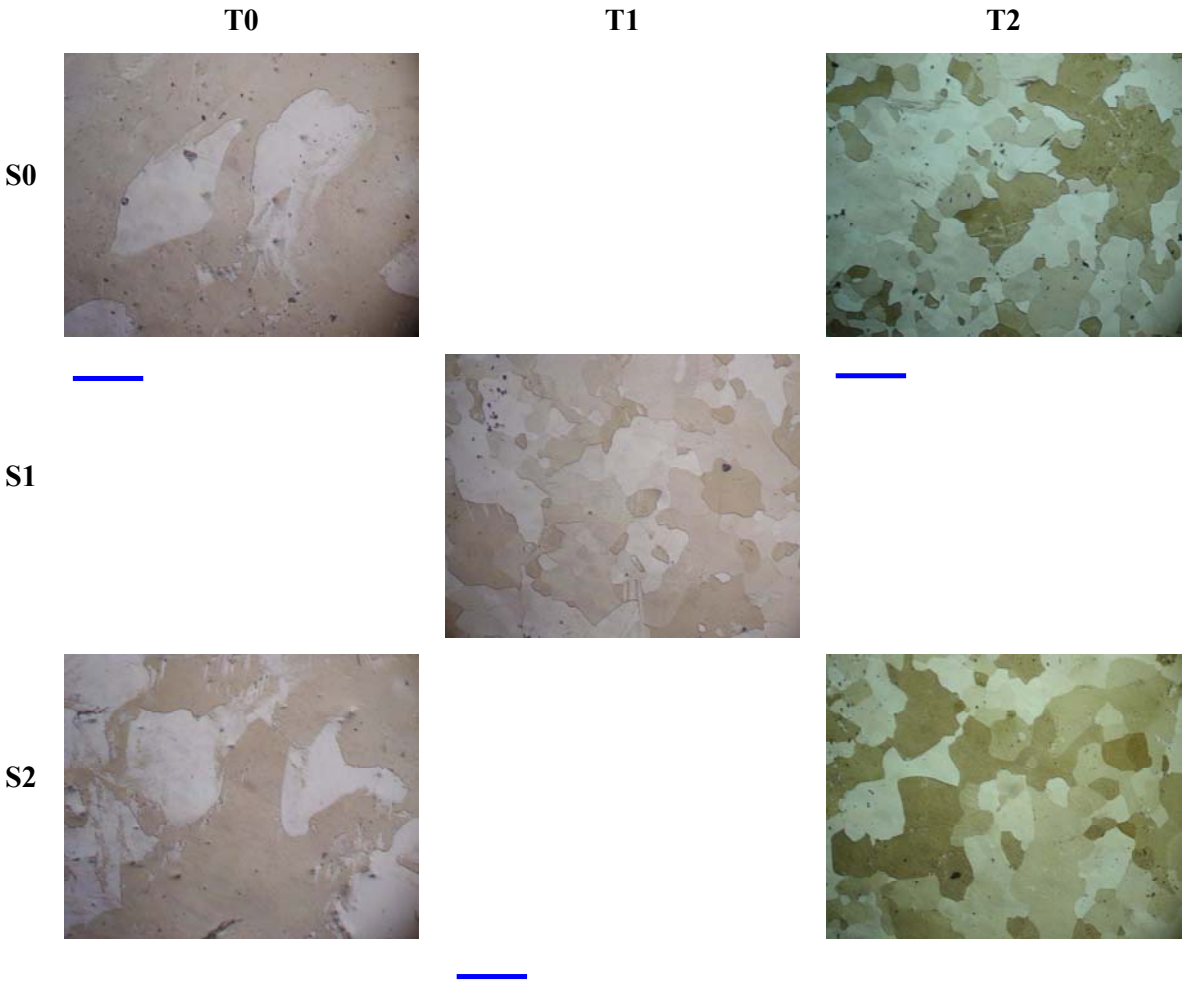

Figure 6.12: Optical microscope images of molybdenum samples viewed in the **x**-direction (scale bar is 200 μm in each image).

Figure 6.13 shows an image of each molybdenum sample investigated using the **y**-surface. Similar traits are observed on the Y-sample surfaces. However, the unannealed samples exhibit a distinct grain orientation. This orientation of the grains indicate in which direction deformation of the liner material took place when the liner cone was manufactured (see figure 6.8). Although the grains in the unannealed samples are not as defined as in the case of the annealed samples, the images are sufficiently clear to be able to determine a grain size from them.

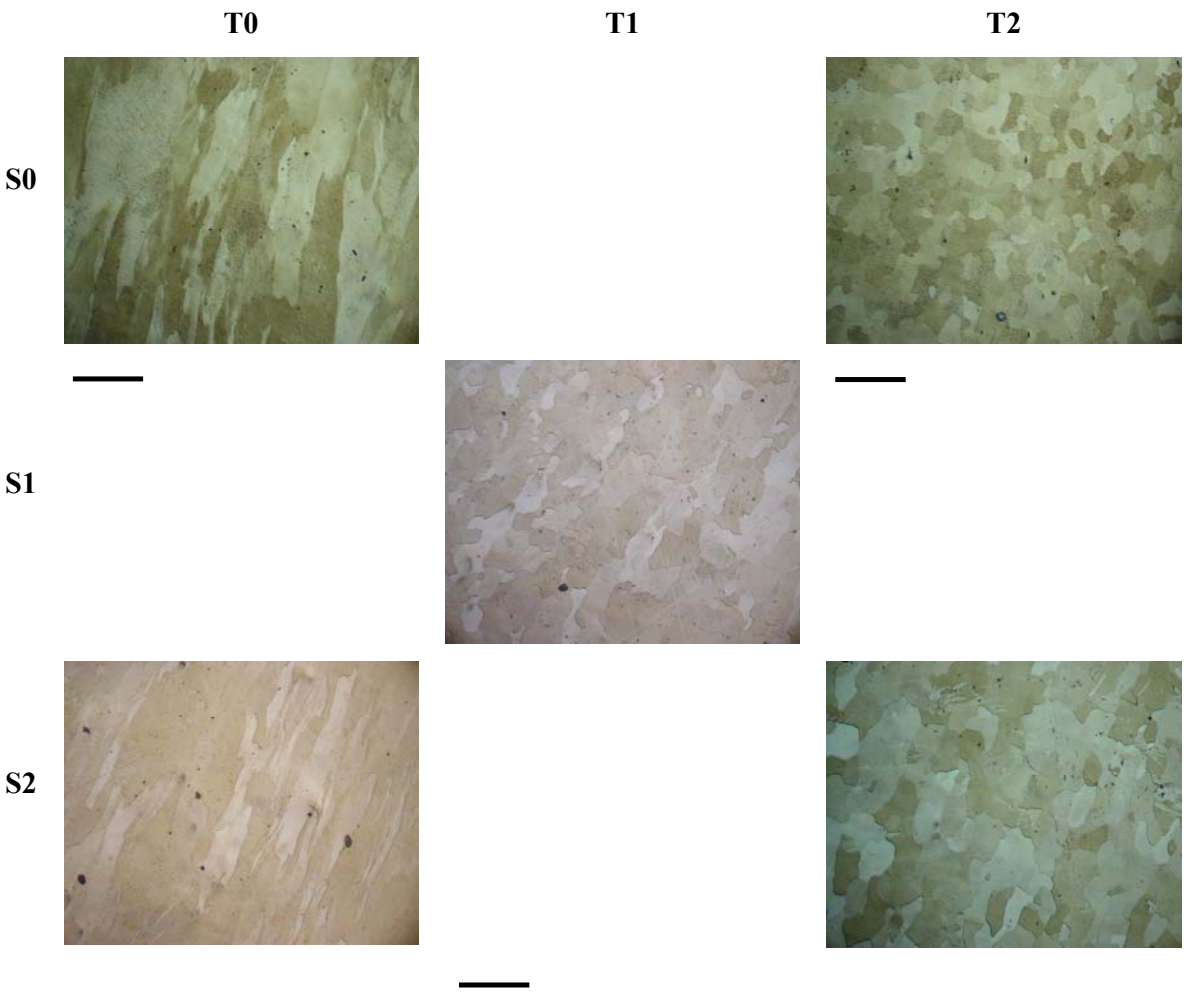

Figure 6.13: Optical microscope images of molybdenum samples viewed in the **y**-direction (scale bar is 200 μm in each image).

Table 6.3 shows the average linear intercepts lengths for the samples obtained using an image with an area of 800000 μm^2. Seven equally spaced lines were used per sample. In the case of the samples showing a distinct grain orientation, an additional measurement was made. One measurement was made along the long axis of the grains, and one along the short axis. This information is shown in that order in table 6.3 and table 6.4 which shows minimum and maximum grain sizes obtained from each 7 number data set per sample.

Table 6.3: Average grains size of molybdenum samples calculated using the Heyn method.

Sample	Grain Size on X plane (µm)	Grain Size on Y plane (µm)
T0S0	236	215 ; 67
T0S2	159	236 ; 50
T1S1	92	59
T2S0	80	47
T2S2	78	61

Table 6.4: Minimum and maximum grain sizes obtained from each 7 number data set per sample.

Sample	Grain Size on X plane (µm)		Grain Size on Y plane (µm)	
	Min	Max	Min	Max
T0S0	111	500	95 ; 39	285 ; 108
T0S2	83	333	112 ; 35	432 ; 64
T1S1	77	111	48	71
T2S0	53	111	40	56
T2S2	63	111	50	77

When comparing the grain sizes of the annealed and unannealed samples, further confirmation is obtained that recrystallisation took place during annealing. It can also be seen that both the annealing temperature and the amount of strain used were insufficient to create significant differences in the grain structure of samples T1S1, T2S0 and T2S2.

6.6 Discussion and Conclusions

Different techniques provided images of different quality for each material type. In the case of copper the BSED gave images of excellent quality when the unstrained samples were viewed. The reason why the image quality decreased for the strained

samples is unclear at this stage, but can be related to the increase in dislocation density. No such decrease in quality was observed in the case of the images taken with the optical microscope. Very poor images of the molybdenum samples were obtained in the SEM. The reason for this seems that the etchant used for the molybdenum was a lot less aggressive in terms of its acidic nature when compared with the etchant used for copper. This resulted in a shallower etch which in turn resulted in less contrast in the SEM images. It can be said that if only one apparatus were to be used, the standard optical microscope would be the first choice for all work pertaining to grain size determination. Although the Heyn technique proved satisfactory when used to determine the various grain sizes, it must be noted that this as well as the other techniques mentioned are better suited for samples with a uniform and equiaxed grain structure. Furthermore, despite the fact that different techniques are available, very few researchers quote the method used when stating grain sizes. This can only lead to confusion, and false conclusions for the reader of such a report.

The object of the annealing procedures was to obtain two different microstructures for each material, with one grain size approximately double that of the other. This was achieved in the case of the copper samples, and thus the times and temperatures used can be considered a good starting point for a study of this nature. Unfortunately in the case of the molybdenum samples the annealing temperature proved to be too low to ensure adequate grain growth. An annealing temperature of at least 1500˚C would be recommended to obtain two different microstructures. Nevertheless, it should be noted that for shaped charge liners, a fine grain structure without grain growth is desirable (section 3.3.2). To achieve this, annealing at 1200˚C for 30 minutes is appropriate. Two distinct magnitudes of grain sizes were noticed between the copper and molybdenum samples, the copper having a very fine structure when compared to that of the molybdenum.

In the case of both the copper and molybdenum samples, but especially in the case of the molybdenum, very little evolution of the microstructure can be noticed due to the straining that took place. This indicates that the amount of deformation that took place during the SHPB was too low to give clear effects on the grain structure level.

6.7 References

Askeland D.R. **[1998]** *The Science and Engineering of Materials*, Stanley Thornes Ltd.

Dehoff R. and Rhines F. **[1968]** *Quantitive Microscopy*, McGraw - Hill Ltd.

Exner H.E. **[1983]** *Qualitative and Quantitative Surface Microscopy* in *Physical Metallurgy*, 3nd Ed, Elsevier Science Publishers

Greaves R.H. and Wrighton H. **[1967]** *Practical Microscopical Metallography*, Chapman and Hall Ltd.

Gurevitch A.C., Murr L.E., Shih H.K., Niou C-S., Advani A.H., Manuel D. and Zernow L. **[1993a]** *Materials Characterization* **30** p201.

Gurevitch A.C., Murr L.E., Fisher W.W., Varma S.K and Advani A.H. **[1993b]** *Journal of Material Science* **28** p2795.

Lee S., Hong M., Noh J. and Baek W.H. **[2002]** *Metallurgical and Material Transactions* **33A** p1069.

Oxford Instruments Analytical, **[2004]** *Electron Backscattered Diffraction Explained – Technical Briefing,* Oxford Instruments Analytical Limited.

Schmidt C.G., Caligiuri R.D., Giovanola J.H. and Erlich D.C. **[1991]** *Metallurgical Transactions* **22A** p2349.

Tian W.H., Fan A.L., Gao H.Y., Luo J. and Wang Z. **[2003]** *Materials, Science and Engineering* **A350(1-2)** p160

Chapter 7

Transmission Electron Microscopy investigation of samples

7.1 Introduction

Transmission electron microscopy (TEM) was used to investigate the microstructure of the copper and molybdenum samples. A description of the technique and theory behind TEM is given in section 4.6. In order to easily view the different crystal orientations, use is made of a double tilt holder which allows the user to tilt the sample in perpendicular planes. This allows the user to view a grain using different orientation and diffraction vectors ($\boldsymbol{g}$). This ability is imperative if dislocation analyses are to be performed. As the Philips CM100 transmission electron microscope available at the University of the Free State only has a single tilt sample holder (typical of a TEM used mainly for biological work), most of the TEM work had to be performed at another location. Prof J.H. Neethling from the Nelson Mandela Metropolitan University (NMMU) in Port Elizabeth kindly made their TEM facilities available for use. For this and his assistance in the TEM work, myself and my supervisors are highly appreciative. Special thanks must also be given to Dr P.R. Berndt for her assistance and advice in regards to sample preparation and rotation calibration of the two TEM microscopes (Philips CM20 and Philips EM420) used. Later a rotation holder become available at the UFS and was used to examine some of the molybdenum samples. Although the two degrees of freedom of this holder theoretically allows the user to tilt the sample arbitrarily, the rotation is tedious as large rotations are necessary during which sample position shifts must be tracked. In addition, sample and diffraction imagers are rotated, which increases the complexity of the analysis.

Unfortunately due to the cost and practical limitations involved in working at a different location, a limited amount of time was available for TEM analysis of the samples. A decision was made to only do an overview of the sample microstructures,

instead of an in-depth study of one single aspect. This however does leave a broad base for any future work.

7.2 Experimental

TEM work involves several important aspects, most importantly sample preparation. Other aspects include determination of the camera length and rotation calibration of the images.

7.2.1 Sample preparation

The objective when preparing a TEM sample is to produce a round sample with a diameter such that it will fit into the sample holder, in this case 3 mm, that is electron transparent (see chapter 4.6), and that has an unaltered microstructure, i.e. the sample must not be damaged during sample preparation.

To do this involves several steps:

- Cutting sample slices from the original samples.
- Polishing the sample to at least 100 μm or thinner.
- Extracting a round sample with a diameter of 3 mm from this sample slice.
- Ion milling, chemical etching or electro-chemical etching of samples to obtain electron transparency.

The cutting of sample slices from the original cylindrical samples used for straining proved to be much more difficult than initially anticipated. A diamond wire saw used by staff at NMMU to cut samples proved to be useless for cutting copper, probably due to its ductility. After twenty minutes of cutting, a brand new wire broke, after hardly making any impression on the sample. Similar results have been experienced by NMMU staff for aluminium. A small motor driven saw was then tried as an alternative using a diamond impregnated cutting wheel. Although the process was extremely slow, reasonably good results were initially obtained. It however became

clear that the motor of the saw was not sufficiently strong to cut the copper. After the motor was damaged, and repaired it was used again in an attempt to cut the copper, but this proved to be a futile effort. Staff at NMMU offered the use of a more powerful saw, but due to the size of the blade and strength of the motor it was deemed inappropriate because of possible microstructural damage that would be imparted to the samples. It was finally decided that wire Electric Discharge Machining (EDM) of both the copper and molybdenum samples would be the most appropriate method to cut the samples. This cutting was performed by TK Manufacturing, and ensured cutting of the samples in a reasonable time, and minimized microstructural damage to the samples. To further ensure that the microstructure remains unchanged at the actual region where TEM work took place the slices were cut 500 μm thick. This ensured that any surface damage would be removed by polishing.

The copper and molybdenum samples were then polished as follows: sandpaper was used to remove the surface layer of the sample. This was done to ensure that the image obtained was representative of the sample, and not due to some surface irregularity or surface damage due to the cutting process. The surface was then polished using progressively finer grits, ensuring that the surface damage caused by each grit was removed by the following grit. The finest grit used was 1200 grit. The sample was then polished using 9 μm, 6 μm and 3 μm diamond suspension.

At this stage the copper samples were in the region of 70 μm thick. Using a punch designed for the use of TEM sample preparation, disks with a diameter of 3 mm were punched out of the polished material. When this was done with the molybdenum samples with a similar thickness, several samples were lost due to the samples fracturing during punching. It seemed that the molybdenum was too brittle. Further molybdenum samples were thinned to a thickness of about 30 μm. This made the successful punching of the samples possible.

These samples were then reduced to electron transparency using a Gatan Model 961 precision ion polishing system (see figure 7.1).

Figure 7.1: Gatan Model 961 precision ion polishing system (Photo by Mr. W.E. Goosen).

Ion milling was performed with both the right and left ion guns set at an incidence angle of 6˚ and an ion energy of 5 keV. Ar^+ ion milling was used instead of chemical or electro-chemical etching solely because of equipment availability. The milling process was stopped as soon as the sample was milled through. After this step the samples were ready to be examined in a TEM.

7.2.2 Indexing of diffraction patterns

The first step in analyzing any TEM images obtained from a crystalline material is the indexing of the diffraction pattern. This can be done by comparing a diffraction pattern taken at the zone axis to a theoretical diffraction pattern from any number of references on TEM analysis (e.g. Loretto and Smallman, 1975, p116, 121). Figure 7.2(a) shows such an image of the [001] zone axis of molybdenum taken on the CM100 TEM. By measuring the angles between various directions in the diffraction pattern, and then comparing this with the theoretical angles as shown in figure 7.2(b),

the zone axis can be identified. Furthermore this identification can be verified by comparing the ratio between the distances of the diffraction spots for two different directions. These measurements are linked to the interplanar spacing in that direction for the material. This can be extended by drawing concentric rings on the diffraction pattern as can be seen in figure 7.2(a), each ring indicating the distance from the centre spot on which a certain reflection must occur. It can be verified whether each spot does indeed occur on the correct distance from the centre spot. Using the above mentioned procedure the zone axis can be identified, and by using the theoretical diffraction pattern the indexing can be completed.

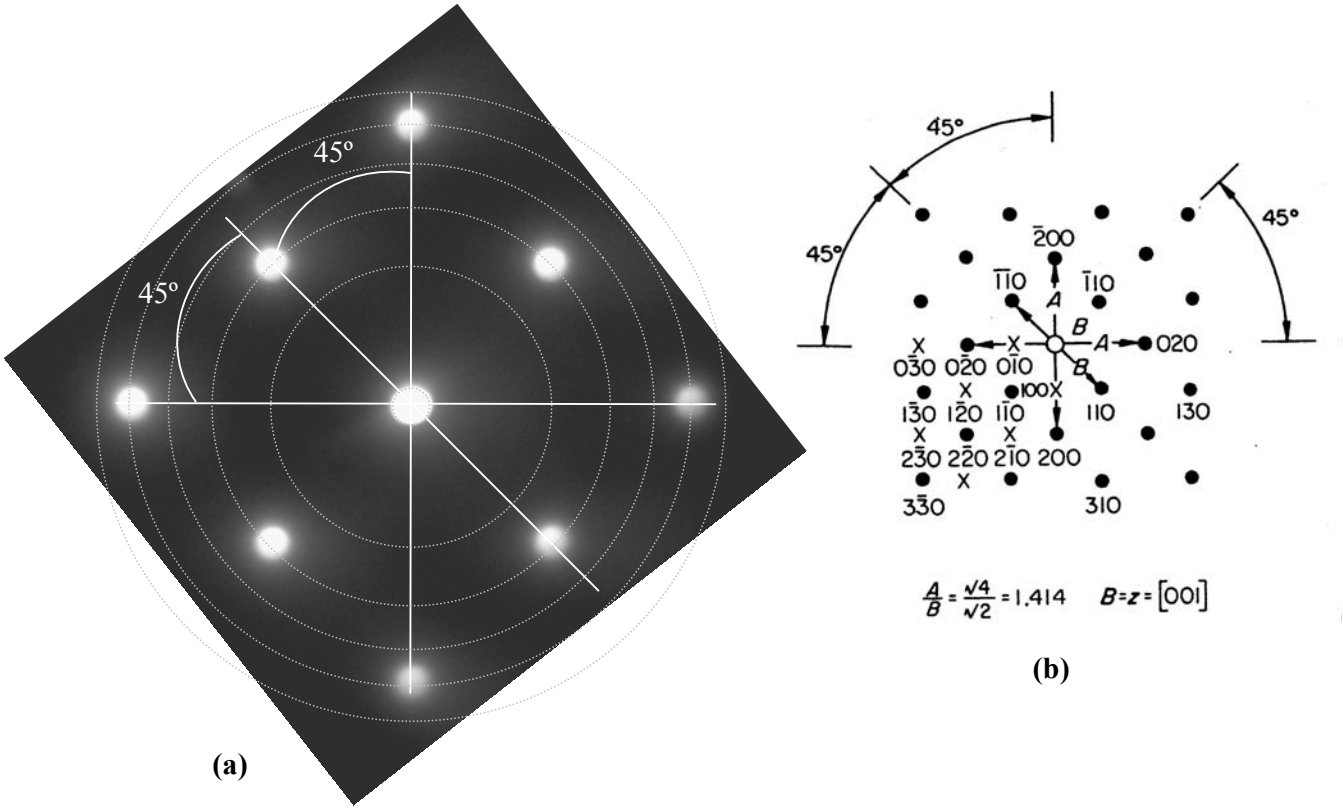

Figure 7.2: (**a)** Diffraction pattern of molybdenum, **(b)** theoretical diffraction pattern of the [001] zone axis in BCC materials (Edington, 1975, p98).

It should of course be kept in mind that not all reflections are allowed. In the case of FCC materials no reflections can occur for which the plane indices are partly even or partly odd. In the case of BCC materials h + k + l must be even (Kittel, 1966, p63-65). The reflections that are not allowed are indicated figure 7.2(b) as an X.

7.2.3 Camera lengths

For certain diffraction pattern analyses it is important to know the exact camera length used. Figure 7.3 shows the primary electron beam in a TEM microscope being diffracted by a sample, and the diffracted and transmitted beam incident on the photographic plate.

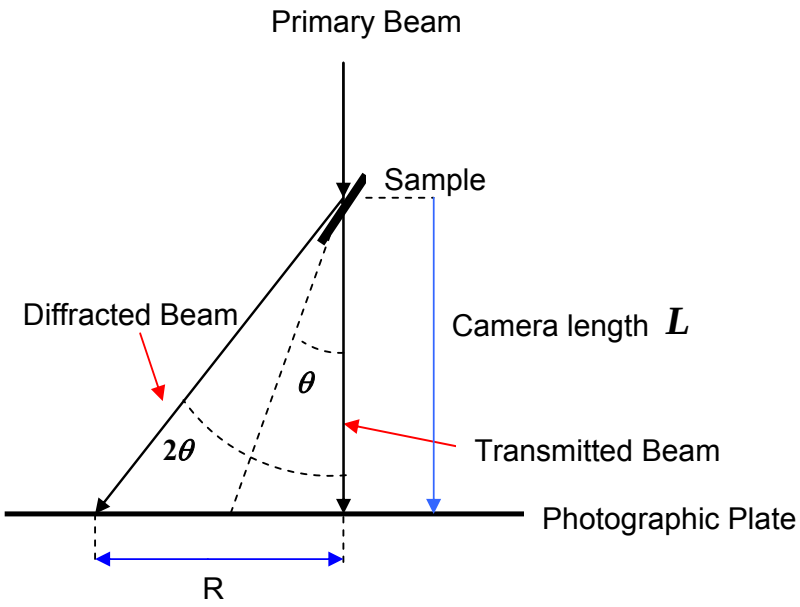

Figure 7.3: Simplified beam paths in a TEM (Adapted from Von Heimendahl, 1980).

Note that the incident and diffracted beams are separated by an angle 2θ. From this figure it can be seen that

$$\tan 2\theta = \frac{R}{L} \qquad \textbf{(7.1)}$$

where R is the distance between the transmitted beam and a diffraction spot as measured along the photographic plate, and L is the camera length or the distance between the sample and photographic plate. Since the angles in question are small, (see section 4.6) $\sin\theta \approx \theta$ and $\tan 2\theta \approx 2\theta$, and it follows from equation 7.1 and Bragg's law (equation 4.10) that

$$\lambda L = Rd\,. \tag{7.2}$$

The interplanar spacing d of the lattice planes can be calculated for cubic materials using

$$d = \frac{a}{\sqrt{h^2 + k^2 + l^2}} \tag{7.3}$$

where a is the lattice constant, and h, k and l are the Miller indices of the plane (Kittel, 1966, p44).

Figure 7.4 shows the measurements done on a [110] zone axis diffraction pattern of a copper sample (T2S2), for the $\pm 1\bar{1}1$ spots, and table 7.1 shows the results of the camera length calculations for the CM20 operating at 200 kV using equations 7.2 and 7.3 and the above diffraction pattern as well as a similar pattern taken at a different camera length. The electron wavelength and lattice constant used for the calculations were 2.5 pm (using equation 4.9) and 0.3615 nm (Askeland, 1980, p830), respectively.

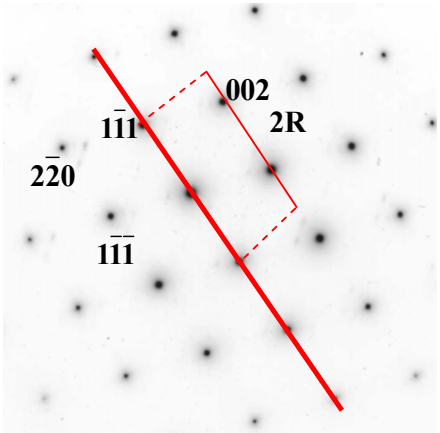

Figure 7.4: Diffraction pattern of copper sample (T2S0) with $\boldsymbol{B}$ = [110] used for determination of camera length.

Table 7.1: Results and calculations of the camera length for the CM20 microscope at 200 keV for two camera lengths.

Displayed L (m)	hkl	$2R$ (mm)	d (Å)	L (m)	Average Measured L (m)
0.7	$\pm 1\bar{1}1$	16.7	2.08	0.69	0.683 ± 0.006
	$\pm 1\bar{1}\bar{1}$	16.5	2.08	0.68	
	± 002	19.0	1.80	0.68	
1	$\pm 1\bar{1}1$	23.0	2.08	0.95	0.953 ± 0.006
	$\pm 1\bar{1}\bar{1}$	23.2	2.08	0.96	
	± 002	26.5	1.80	0.95	

This indicated that although the CM20 TEM displays the camera length as 0.7 m and 1 m, the average camera length from table 7.1 indicate that the true camera lengths used are 0.68 m and 0.95 m.

7.2.4 Rotation Calibration

In modern TEM microscopes electron beams are deflected and focused by means of electromagnetic lenses. If electrons with a charge e and velocity $\boldsymbol{v}$ approach the lens nearly parallel to the optical axis, the force exerted on the electron by the magnetic field $\boldsymbol{B}$ is the Lorentz force $\boldsymbol{F} = e(\boldsymbol{v} \times \boldsymbol{B})$. The force $\boldsymbol{F}$ acts normal to the direction of the magnetic field and normal to the velocity of the electrons and, therefore, forces the electrons out of the axial direction and into a helical path. Therefore, the image is rotated when the magnification or accelerating voltage is changed. It is thus necessary to rotate the image and diffraction pattern against each other to determine the correct relationship between the two.

This rotation angle is a function of the magnification and accelerating voltage used, and must be determined empirically for each electron microscope (Von Heimendahl, 1980). Figure 7.5 shows two images of a twin in copper (T2S2) taken at 50 000 and

88 000 times magnification on a Philips CM20 TEM microscope at 200 keV. The effect of the magnetic rotation is clearly visible.

The calibration can be done by taking a series of images of a sample with a well defined crystalline cleavage plane or direction, or a structure with a known direction at different magnifications and at a constant accelerating voltage. By then comparing a diffraction pattern of the area with the image, one can quickly establish what the degree of rotation must be.

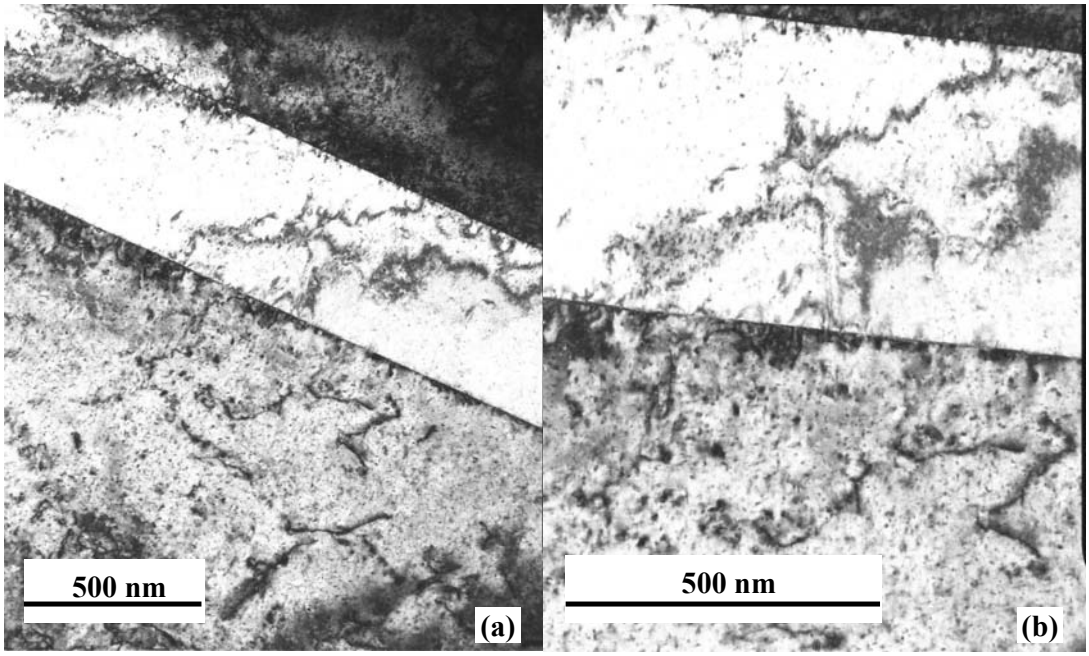

Figure 7.5: Magnetic rotation of twin image taken at different magnifications, **(a)** taken at 50k and **(b)** at 88k.

Figure 7.6 shows an image taken at 34000 times magnification of GaAs with a $[1\bar{1}0]$ direction along the interface and **B** = [110]. By placing the diffraction pattern and image next to each other, both emulsion side up, and then rotating the diffraction pattern in an anticlockwise direction relative to the image, the appropriate rotation angle value can be determined. The direction of rotation, and whether the diffraction pattern or image rotated is not important, but it does simplify the process if uniformity is kept through out the calibration process. By repeating this process with every magnification, camera length and accelerating voltage used, the rotation calibration for the microscope can be completed.

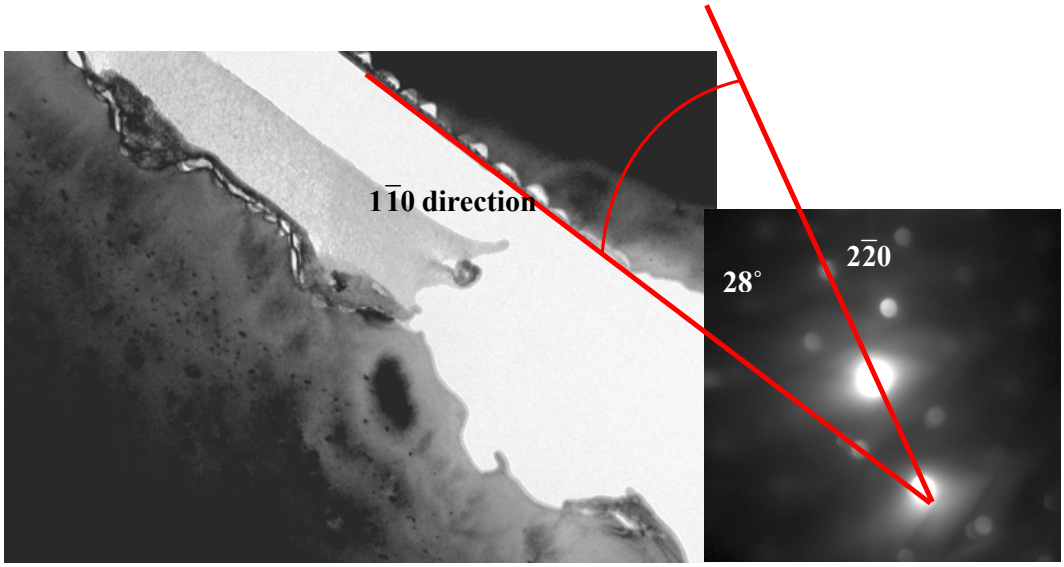

Figure 7.6: Figure showing rotation calibration method performed with a GaAs sample, investigated on the CM100 at 100keV, using a magnification setting of 34k.

Table 7.2 shows the completed rotation calibrations for all the TEM microscopes used in this study. In all cases the diffraction pattern was rotated anticlockwise relative to the image.

Table 7.2: Rotation calibration of TEM microscopes used during study. The angle X° gives the anticlockwise rotation necessary for the diffraction pattern. The distance given next to the accelerating voltage is the camera length.

EM420	
100 keV , 950 mm	
Magnification	**X°**
36000	37.5
49000	40.7
60000	43.5
82000	48.0
105000	52.2
135000	58.0
175000	66.7
230000	77.5
300000	92.7

CM20	
200 keV , 1000 mm	
Magnification	**X°**
6610	-46.0
8800	-49.0
27500	-6.0
38000	-13.0
50000	-12.0
66000	0
88000	6.0
115000	24.5
150000	36.5

CM100	
100 keV , 1100 mm	
Magnification	**X°**
13500	-18.0
19000	7.0
25000	20.0
34000	28.0
46000	29.0
64000	39.0
92000	55.0
130000	84.0
180000	122.0

7.3 Results for copper

A brief overview of the most important features found in copper will be given, after which these as well as other features will be discussed in detail.

The most important features found in copper included twins on the {111} planes and dislocations. Examples of these features can be seen in figure 7.7. Table 7.3 gives a summary of these features in the different samples. All the images were taken with **B** = [110]. The diffraction vectors for the two beam conditions are indicated on the images.

Table 7.3 Summary of primary features found in copper by TEM investigation

T0S0	**T1S0**	**T2S0**
Twins: No twins were found. **Dislocations**: Low density with very few well defined dislocation segments.	**Twins:** No twins were found. **Dislocations:** High density with long dislocation segments.	**Twins:** No twins were found. **Dislocations:** Very low density, but with well defined dislocation segments.
T0S1	**T1S1**	**T2S1**
Twins: No twins were found. **Dislocations:** Low density with very few well defined dislocation segments.	**Twins:** A high density of twins was found. Twin bands ranged in width from 60 nm to 650 nm. **Dislocations:** Low density with very few well defined dislocation segments.	**Twins:** Twin bands ranging in width from 60 nm to 130 nm were found. Low density. **Dislocations:** Low density with very few well defined dislocation segments.
T0S2	**T1S2**	**T2S2**
Twins: No twins were found. **Dislocations:** Low density with very few well defined dislocation segments.	**Twins:** Various twin bands were recorded. Widths ranged from extremely narrow to 300 nm **Dislocations:** High density with long dislocation segments.	**Twins:** Low density of twins. The presence of a twin band with a width of 440 nm was recorded. **Dislocations:** High density with long dislocation segments.

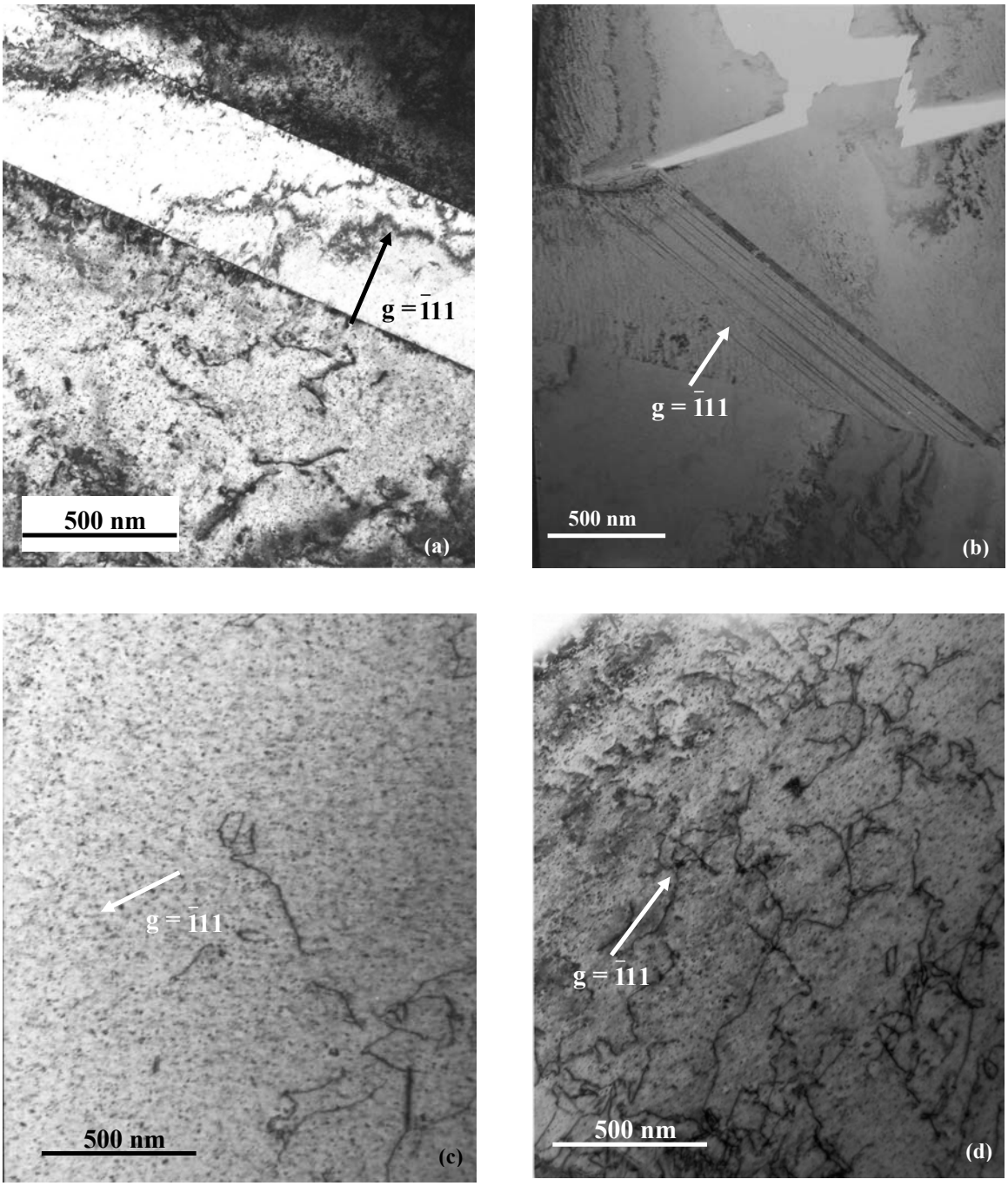

Figure 7.7: (a) Large twin in T2S2, **(b)** Small twin bands in T2S1, **(c)** Low dislocation density in T2S0 **(d)** High dislocation density in T1S0.

7.3.1 Dislocations

It is generally accepted that the slip system of FCC metals is {111}<110>, i.e. slip occurs on the {111}-type planes and in the <110>-type directions (Askeland, 1998, p84). The Burgers vector associated with such slip is $\mathbf{b} = {}^{a}/_{2}\langle 110\rangle$ and corresponds to the nearest-neighbour directions in the lattice. Figure 7.8 shows Thomson's tetrahedron, which is useful for analyzing such dislocations. When the three outside triangles are folded up to join all the points D, it shows each of the six possible ${}^{1}/_{2}\langle 110\rangle$ vectors, lying on the intersections of the {111}-type planes.

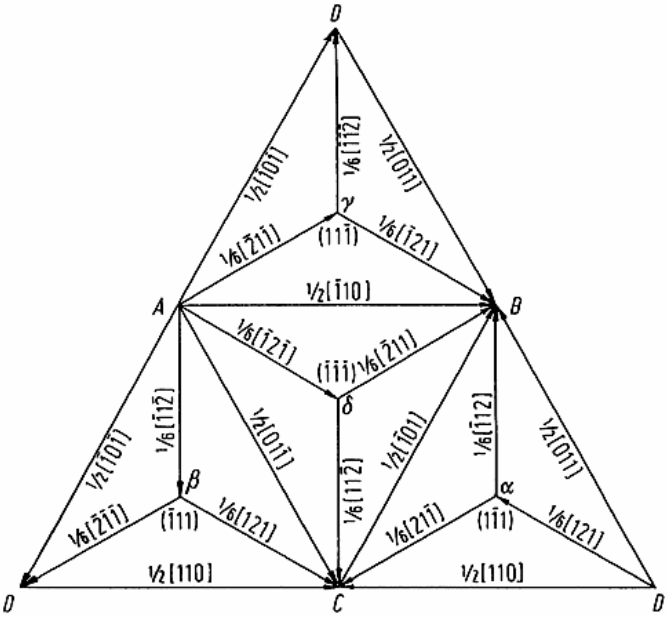

Figure 7.8: Thomson's tetrahedron (www.tf.uni-kiel.de/matwis/amat/def_en/index.html).

Table 7.4 lists the possible Burgers vectors, as well as their projections onto the (110) plane. The projections are calculated using

$$\mathbf{b}_{proj} = \mathbf{b} - (\mathbf{b} \cdot \hat{\mathbf{n}})\hat{\mathbf{n}} \qquad (7.4)$$

where $\hat{\mathbf{n}}$ is the unit vector in the [110] direction. This is useful if TEM is carried out with the beam direction **B** = [110]. From table 7.4 it can be seen that one of the six possible orientations for the Burgers vector will never result in TEM contrast when viewed in the **B** = [110] zone axis since its projection is zero, while the others will display contrast when the diffracting vector has a component along their projected directions. It can be noted that if $\mathbf{g} = 2\bar{2}0$, all of these others will display contrast,

and that certain dislocations should become invisible when the 111- and 004-type reflections are used.

Table 7.4: Possible Burgers vectors projected onto (110) plane.

Burgers vector	Burgers vector projected on (110) plane
$^{a}/_{2}[110]$	Zero
$^{a}/_{2}[1\bar{1}0]$	$^{a}/_{2}[1\bar{1}0]$
$^{a}/_{2}[101]$	$^{a}/_{4}[1\bar{1}2]$
$^{a}/_{2}[10\bar{1}]$	$^{a}/_{4}[1\bar{1}\bar{2}]$
$^{a}/_{2}[011]$	$^{a}/_{4}[1\bar{1}\bar{2}]$
$^{a}/_{2}[01\bar{1}]$	$^{a}/_{4}[1\bar{1}2]$

Directions of pure edge dislocations

If one assumes that the dislocations are pure edge in nature, then they must extend in a direction on their slip plane perpendicular to their Burgers vector. The dislocation direction can then be calculated from the cross product of the Burgers vector and slip plane normal. The possibilities for the directions of the dislocation lines are given in table 7.5, as well as the projected directions when such dislocations are viewed from the **B** = [110] zone axis.

Table 7.5: Directions of pure edge dislocations. The first two rows are in blue because such dislocations have zero projected Burgers vector on the (110) plane and are therefore never visible from the [110] zone axis.

Burgers vector	Slip plane	Dislocation direction	Dislocation direction projected on (110) plane
$^{a}/_{2}[110]$	$(1\bar{1}1)$	$[1\bar{1}\bar{2}]$	$[1\bar{1}\bar{2}]$
	$(1\bar{1}\bar{1})$	$[1\bar{1}2]$	$[1\bar{1}2]$
$^{a}/_{2}[1\bar{1}0]$	(111)	$[11\bar{2}]$	[001]
	$(11\bar{1})$	[112]	[001]
$^{a}/_{2}[101]$	$(11\bar{1})$	$[1\bar{2}\bar{1}]$	$[3\bar{3}\bar{2}]$
	$(1\bar{1}\bar{1})$	$[12\bar{1}]$	$[1\bar{1}2]$
$^{a}/_{2}[10\bar{1}]$	(111)	$[1\bar{2}1]$	$[3\bar{3}2]$
	$(1\bar{1}1)$	[121]	$[1\bar{1}\bar{2}]$
$^{a}/_{2}[011]$	$(11\bar{1})$	$[2\bar{1}1]$	$[3\bar{3}2]$
	$(1\bar{1}1)$	$[21\bar{1}]$	$[1\bar{1}\bar{2}]$
$^{a}/_{2}[01\bar{1}]$	(111)	$[2\bar{1}\bar{1}]$	$[3\bar{3}\bar{2}]$
	$(1\bar{1}\bar{1})$	[211]	$[1\bar{1}2]$

Dislocations of this nature, with Burgers vectors of the type $\mathbf{b} = {}^{a}/_{2}\langle 110\rangle$ and lying in the <112>-type directions, were identified in copper electrodeposits by Lee and Lee (2000) using TEM.

Other orientations of dislocations

Hornstra (1958) discussed dislocations in the diamond lattice, which is actually an FCC lattice having a basis of two atoms. He suggested that the dislocation lines should lie in the <110> directions, just as the Burgers vectors do. Considering the six possible <110> directions, the dislocation line and Burgers vector may in one case be parallel (yielding a screw dislocation), in another case perpendicular (yielding an edge dislocation), and in four cases make an angle of 60° (mixed dislocation). The edge-type is called a Lomer-lock, since the dislocation line and Burgers vector are contained in a {100} plane, which is not the slip plane, so these dislocations are immobile (sessile). The 60° dislocations are contained in {111} planes and may therefore slip. The thirty-six possible dislocations in this scheme are too many to enumerate, but are easily imagined if one considers for each possible Burgers vector in table 7.4, the screw dislocation with parallel dislocation line as well as the edge and four other 60° dislocations with their various line orientations along <110> directions. Another way to consider these dislocations is to notice that, in the [110] projection, they can lie projected along the $[1\,\bar{1}0]$ direction, or the $[1\,\bar{1}2]$ or $[1\,\overline{12}]$ directions (or lie parallel to the electron beam, having zero projection). For each of these possibilities, the dislocations may be edge, screw, or 60° mixed dislocations. For the edge-type lying along $[1\,\bar{1}0]$ in this sample orientation, it should be noted that $\mathbf{b} = {}^{a}/_{2}[110]$ (parallel to the electron beam) and so this dislocation will not show contrast. Thus visible dislocations of all three types lie along the $[1\,\bar{1}2]$ and $[1\,\overline{12}]$ directions, but visible dislocations lying along the $[1\,\bar{1}0]$ direction must be screw or 60° mixed dislocations.

Dislocations in ultra-high purity FCC aluminium samples were observed by Mizuno *et al.* (2002) to always lie along the <110> orientations, and were therefore identified as 60° type dislocations. Niewczas (2002) studied the dislocations in pure copper deformed at 78 K, and found that for low strains the density of screw and 60° dislocations was small in comparison to bundles of edge dislocations oriented along a

<112>-type direction. However, after further straining it was found that Lomer-lock dislocations, which are edge dislocations running along the <110> directions, were created.

Analysis of dislocations found in this study

Figure 7.9 shows a TEM image of dislocations in the T1S0 copper sample in a grain viewed with the electron beam in the **B** = [110] direction, using the **g** = $00\bar{2}$ diffraction vector.

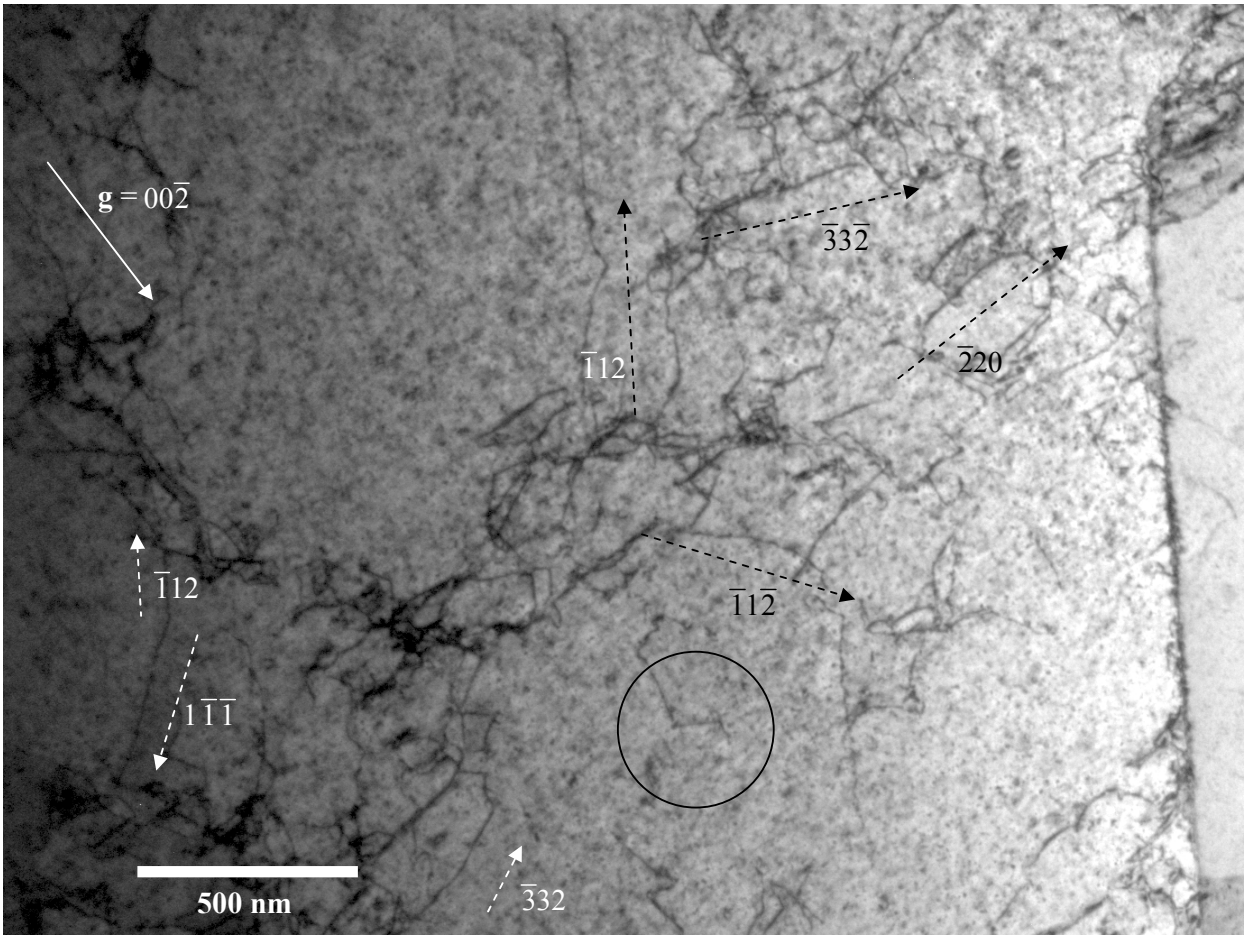

Figure 7.9: Dislocations in T1S0 copper sample viewed with the electron beam in the **B** = [110] direction, using the **g** = $00\bar{2}$ diffraction vector. The circled region is displayed for various diffraction vectors in Figure 7.10.

The dislocations are not uniformly distributed, but occur in entangled networks separated by regions with no dislocations. In order to analyse the dislocations, the TEM images formed using various diffraction vectors must be compared. Figure 7.10

shows the circled region viewed using several different diffraction vectors, obtained by rotating the sample slightly but always remaining near the [110] zone axis.

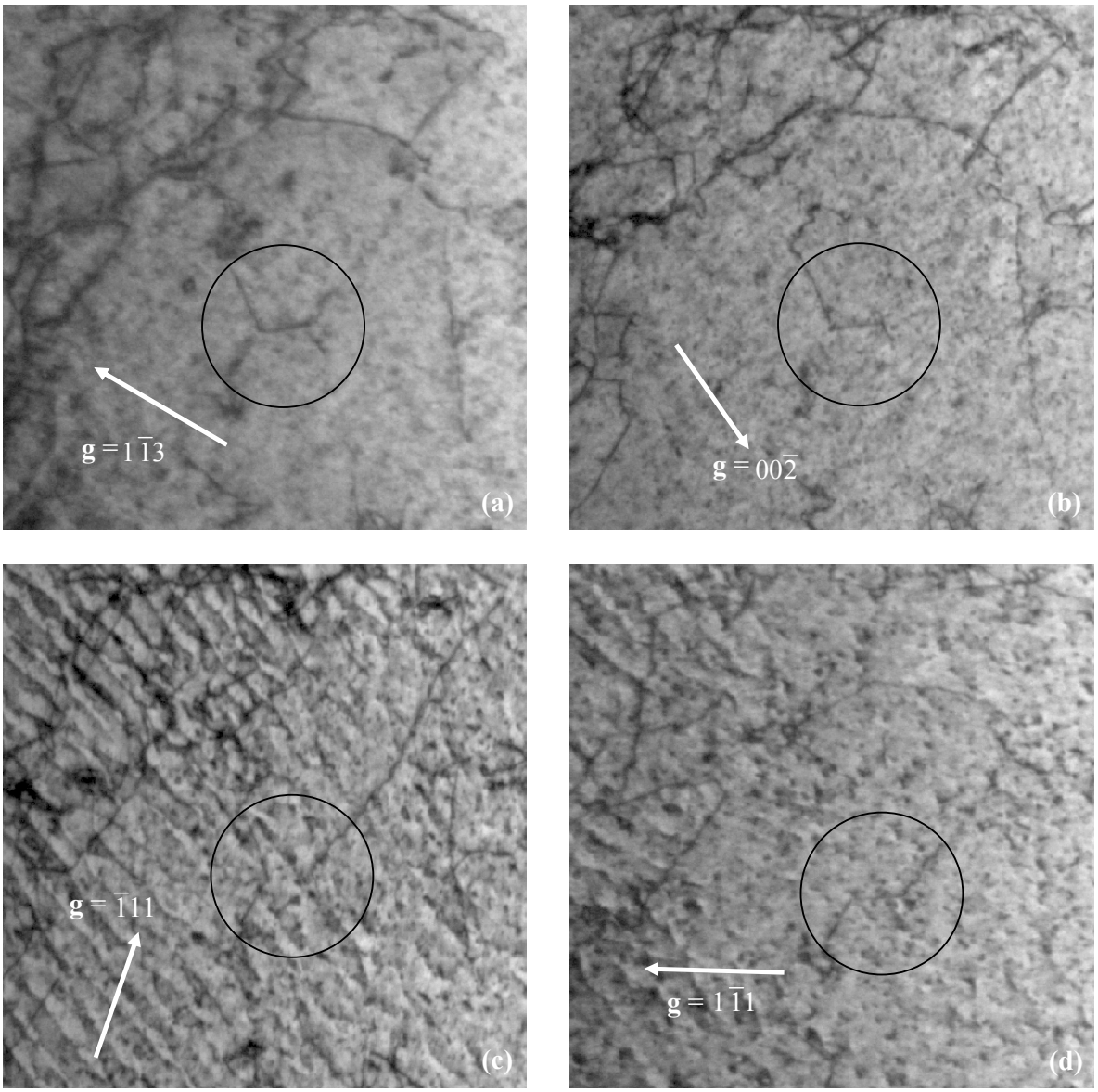

Figure 7.10 Views of a dislocation network in copper sample T1S0 copper sample viewed with the electron beam in the **B** = [110] direction and with various diffraction vectors (a) **g** = 1 $\bar{1}$3 (b) **g** = 00$\bar{2}$ (c) **g** = $\bar{1}$11 (d) **g** = 1 $\bar{1}$1 (e) projected directions of dislocation segments and their Burgers vector in the circles region.

Figure 7.10(a) was obtained using the $\mathbf{g} = 1\bar{1}3$ diffraction vector. All dislocations with Burgers vector of the type $\mathbf{b} = {}^{a}/_{2}\langle 110\rangle$ are expected to be visible according to the $\mathbf{g}\bullet\mathbf{b}$ criterion (see section 4.6) with this diffraction vector, except the one with Burgers vector $\mathbf{b} = {}^{a}/_{2}[110]$ which lies parallel to the electron beam and would thus be invisible for any **g**-vector. The image shows a ⟩—⟨ shaped pattern of dislocations, of which segments are labelled in figure 7.10(e).

Dislocation segment **A** is generally visible, except in figure 7.10(b) for $\mathbf{g} = 00\bar{2}$, where it is invisible implying $\mathbf{g}\bullet\mathbf{b} = 0$. Considering the possible Burgers vectors in table 7.4, excluding the first one, it is possible to deduce that this dislocation corresponds to a Burgers vector $\mathbf{b} = {}^{a}/_{2}[1\bar{1}0]$, which lies in the plane of the image. This Burgers vector corresponds to the line of intersection of the (111) and $(11\bar{1})$ planes, as can be seen from Thomson's tetrahedron (figure 7.8). These two planes are both inclined to the plane of the image by 35°, but in opposite senses about the $[\bar{1}10]$ direction. Initially it was thought that the dislocation must lie in one of the directions discussed in the previous two sections. Consulting table 7.5, if the dislocation were of the pure edge type its projected direction should lie along the [001] direction, yet this is not the case: the dislocation is projected along the $[3\bar{3}\bar{2}]$ direction. Next, the possibility that the dislocation direction lay along a <110>-type direction was considered, but then its projection should lie along one of the projected directions in Table 1, which is not the case. Therefore, the dislocation is not pure screw, of the 60° type, or of the Lomer-lock pure edge type. However, further study of table 7.5 showed that the projected direction of the dislocation does correspond to either the $[\bar{1}21]$ direction on the $(11\bar{1})$ plane or the $[\bar{2}11]$ direction on the (111) plane, both of which have the same projection. This means that although the dislocation is not pure edge type, it appears that the dislocation still lies along a <112> type direction. As can be seen from the Thomson's tetrahedron (figure 7.8), each {111} plane contains three <112> directions, and for a given Burgers vector along a <110> direction, one on these is perpendicular to the Burgers vector while the other two make 30° angles with it. Instead of the expected perpendicular configuration, the 30° configuration is found. Even though the dislocation is not pure edge type, both the Burgers vector and

dislocation direction lie in a common {111} slip plane, and so these dislocations will be mobile i.e. able to glide.

Dislocation segment **B** is invisible in figure 7.10(d) for $\mathbf{g} = 1\,\bar{1}\,1$. From the **g•b** criterion and table 7.4, possible Burgers vectors are $\mathbf{b} = {}^{a}/_{2}[10\bar{1}]$ and $\mathbf{b} = {}^{a}/_{2}[0\bar{1}\,\bar{1}]$, which both have the same projection along the $[1\,\bar{1}\,2]$ direction onto the (110) image plane, but are inclined 35° to it in opposite senses. Both of these possible Burgers vectors have a <112> direction 30° from them with projection onto the (110) plane corresponding to the experimental dislocation line projection along $[00\bar{1}]$ (these are the $[11\bar{2}]$ and [112] directions, respectively). This dislocation is of the same type as segment **A**.

Dislocation segment **C** is invisible in figure 7.10(c) for $\mathbf{g} = \bar{1}11$. From the **g•b** criterion and table 7.4, possible Burgers vectors are $\mathbf{b} = {}^{a}/_{2}[\bar{1}0\bar{1}]$ and $\mathbf{b} = {}^{a}/_{2}[01\bar{1}]$, which both have the same projection along the $[\bar{1}1\bar{2}]$ direction onto the (110) image plane, but are once again inclined 35° to it. Like before, both of these possible Burgers vectors have a <112> direction 30° from them with projection onto the (110) plane corresponding to the experimental dislocation line projection, which in this case is $[3\bar{3}2]$, the inclined directions being $[2\bar{1}1]$ and $[\bar{1}2\bar{1}]$, respectively.

Thus it is possible to explain all of the dislocation segments **A**, **B** and **C** in terms of dislocations along <112> directions with Burgers vectors along <110> directions, with 30° degrees between the dislocation line and Burgers vector which lie on a common {111} slip plane. Since projections were used, it is impossible to distinguish between two possible Burgers vectors for segments **B** and **C**, lying on the two possible {111} planes inclined symmetrically to the (110) image plane. Yet, by the fact that the Burgers vector must remain conserved and hence

$$\mathbf{b}_A + \mathbf{b}_B \leftrightarrow \mathbf{b}_C \qquad \textbf{(7.5)}$$

it follows that the Burgers vector of dislocation **C** must lie in the common plane of the Burgers vectors of dislocations **A** and **B**. It was shown that $\mathbf{b}_A = {}^{a}/_{2}[\bar{1}10]$ and $\mathbf{b}_B =$

$^{a}/_{2}[10\bar{1}]$ or $^{a}/_{2}[0\bar{1}\bar{1}]$, while $\mathbf{b}_C = {}^{a}/_{2}[\bar{1}0\bar{1}]$ or $^{a}/_{2}[01\bar{1}]$. So for instance, if $\mathbf{b}_B = {}^{a}/_{2}[10\bar{1}]$, then $\mathbf{b}_A$ and $\mathbf{b}_B$ both lie in the (111) plane, and since all the Burgers vectors must be coplanar, it follows that $\mathbf{b}_C = {}^{a}/_{2}[01\bar{1}]$. The reaction above can then be written as

$$^{a}/_{2}[\bar{1}10] + {}^{a}/_{2}[10\bar{1}] \leftrightarrow {}^{a}/_{2}[01\bar{1}]. \qquad \textbf{(7.6)}$$

The energy of a dislocation is proportional to the square of its Burgers vector (Barrett and Massalski, 1980, p387). Since all the Burgers vectors in this reaction have the same size, to minimize energy the reaction would proceed to the right, and this is what is expected during annealing. However, if stress is placed in the sample the reaction could occur in reverse, creating more dislocations. These may slip to allow plastic deformation, but simultaneously create barriers to dislocation movement, making the material stronger i.e. work hardening occurs.

In figure 7.10, dislocation segment **D** shows exactly the same properties as segment **A**. However, segment **E** is not parallel to segment **B**, nor does it lie projected along any direction in tables 7.4 and 7.5. Despite this it becomes invisible or visible with different **g**-vectors just like segment **B** and therefore must have the same projected Burgers vector. Looking back at figure 7.9, it is clear that many of the dislocations do not follow straight lines, and those that do are projected in various directions. Many dislocations do lie along the projections of <110> and <112> directions as listed in tables 7.4 and 7.5, yet there are also many exceptions, indicating that the dislocations are not constrained strongly to lie in certain directions.

7.3.2 Twins

As previously mentioned, metals with an FCC crystal structure, such as copper, are generally ductile and deform plastically due to dislocation slip on {111} planes in the <110> directions, while BCC metals at low (room) temperature and HCP metals generally deform due to the formation of twins. Yet deformation twinning of copper occurs if deformed at low (liquid nitrogen) temperatures or at high (~1000 s^{-1}) strain

rates. Very recently, deformation twinning has also been reported in copper undergoing low strain rate (~10^{-2} s^{-1}), severe plastic deformation at room temperature (Huang *et al*., 2006). A summary of the twins found in the copper samples by means of TEM, such as shown in figure 7.7 (a), (b) has already been given in table 7.3. These twins observed by TEM are believed to have formed during deformation, as no twins were found in the samples that were left unstrained. The unannealed but strained samples also showed no evidence of twinning. However, twins were present in all four of the annealed and then strained samples. The twins found in the annealed and strained samples cannot be annealing twins, since they did not occur in the only-annealed samples, and are therefore also identified as deformation twins. Furthermore, these deformation twins are in the order of nanometres, whereas the twins viewed using optical and scanning electron microscopes (see section 6.3) were substantially (in the order of a couple of microns) larger.

Figures 7.11 (a) and (b) show the selected area diffraction (SAD) patterns away from, and overlapping, a non-inclined twin in the sample T2S2 annealed at 500°C and strained at 1550 s^{-1}. The first shows many small double diffraction spots (such as the one labelled **E**) due to a surface oxide (see section 7.3.4), while the second contains extra twin spots. Twinning occurs on the $(1\bar{1}\bar{1})$ plane, and the corresponding $2\bar{2}\bar{2}$ diffraction spot almost coincides in the matrix and twinned patterns, with a small misorientation possibly due to many dislocations near the twin-matrix interface (Toa *et al.,* 2004). Figure 7.11(c) shows a bright field (BF) image of the twin, while figure 7.11(d) is a dark field (DF) image of the same region using a twin spot.

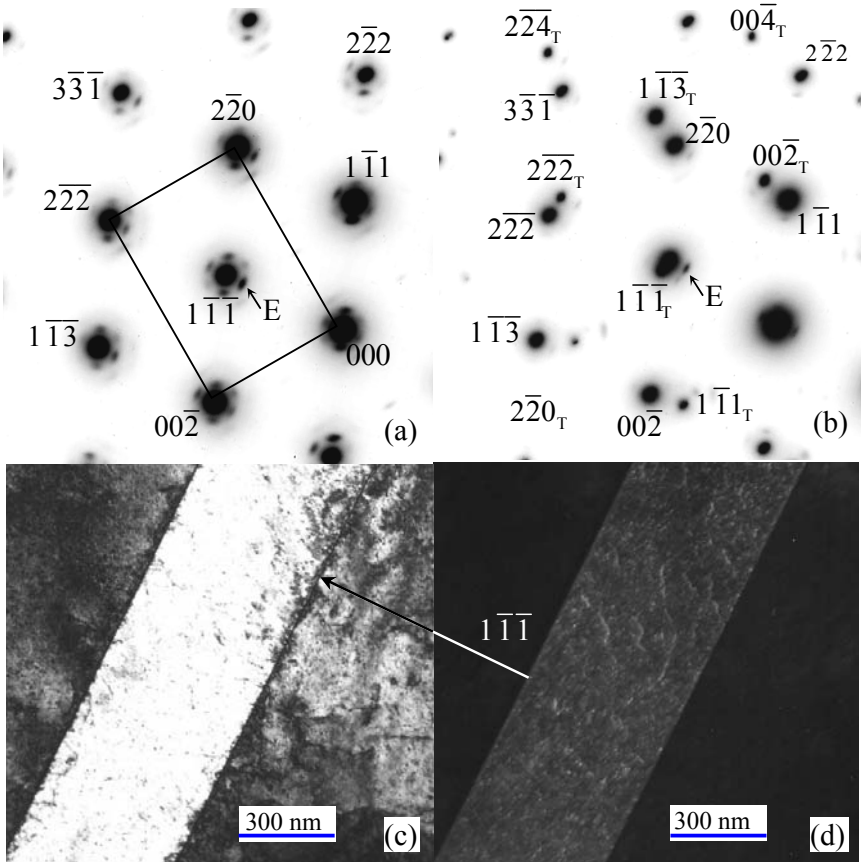

Figure 7.11: (a) SAD pattern in [110] zone axis of copper, away from twin, with many small double diffraction spot due to an oxide layer, **(b)** SAD pattern of region overlapping the twin, showing additional twin spots, **(c)** BF image of twin, **(d)** DF image of twin using a twin diffraction spot. (Images obtained with the CM20 TEM at 200 keV).

Figure 7.12(a) shows a series of thin twin bands in the sample T2S1 annealed at 500°C and strained at 700 s^{-1}. Streaking in the diffraction pattern perpendicular to these thin bands occurs in the corresponding SAD pattern (figure 7.12(b)).

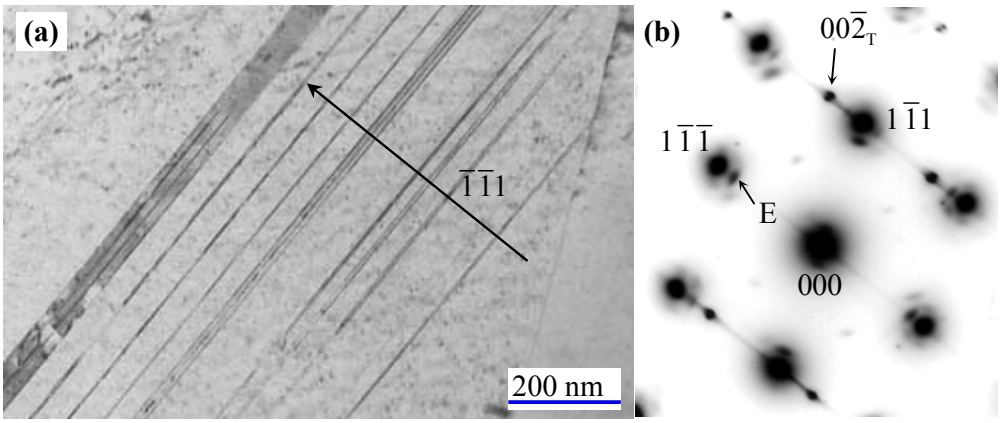

Figure 7.12: (a) BF image of twin bands, and **(b)** corresponding SAD pattern showing streaks, twin spots and double diffraction spots. (Images obtained with the EM420 at 100 keV).

These twins formed at a much lower strain rate than predicted by Meyers *et al*. (2001) for the onset of twinning (see figure 7.13). Their model, however, is questionable because the stress required for twinning was assumed to be constant, whereas it actually decreases with increasing grain size (Huang *et al*., 2006).

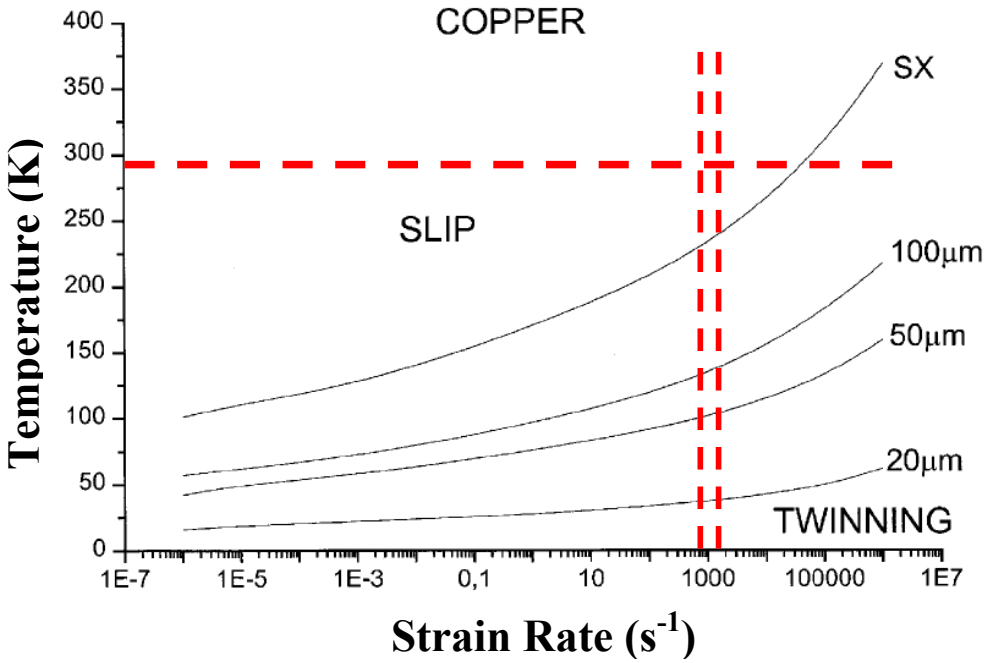

Figure 7.13: Model of Meyers *et al*. (2001) for the slip-twinning threshold in copper. Red dashed lines indicate the straining conditions used in this study. (SX means single crystalline.)

It is interesting that deformation twinning did not occur in the unannealed strained samples, and this is not fully understood. One possibility is that a larger grain size in the annealed samples reduced the stress required for the onset of twinning, which is certainly the case for the higher temperature anneal. A second aspect is that the unannealed samples were strained to only ~7%, whereas the annealed samples were strained to ~14%, making twinning more likely.

7.3.3 Ripples

Ripple like structures were noticed in most of the copper samples. These structures were present in all the samples except T1S0 and T2S2. An example of these structures as found in T0S2 is shown in figure 7.14.

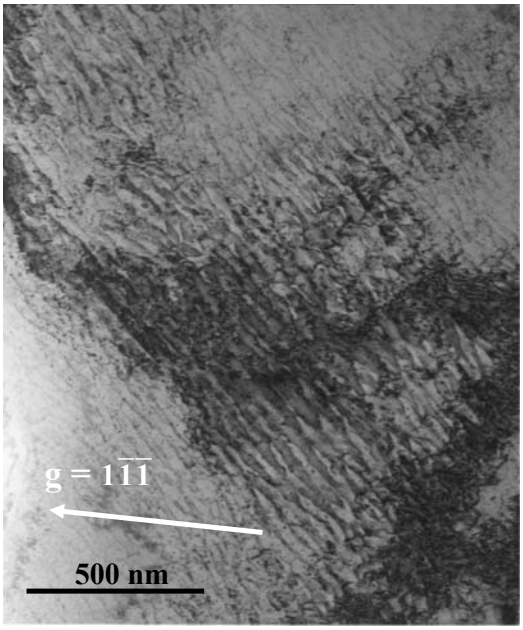

Figure 7.14: Ripple structures in T0S2. Image taken on the CM20 at 200 keV, **B** = [110].

Due to the occurrence of these structures in samples with varying histories (annealing and straining conditions) the possibility must be considered that they are an artefact due to the ion milling that was used during sample preparation.

Chan *et al.* (2006) showed that under Ar^+ ion sputtering, ripples parallel to the beam with a periodicity of hundreds of nanometres can be formed on a Cu (001) surface. These ripples were obtained in samples that were heated to 385 K. As the sample temperature was lowered to 369 K, the ripples changed into arrays of pits. This morphology is different to the ripples shown in figure 7.15 as found in this study. As the samples in this study were ion milled at room temperature (300K) it would be expected that any ion damage would almost certainly manifest itself as pits, and not like ripple structures. Further more, the ripples found in this study are of an order of magnitude smaller, having a spacing of approximately 50 nm, and not in the order of hundreds of nanometres as reported by Chan *et al.* (2006). The results of Chan *et al.* (2006) also show that the orientation of the ripples are dependent on the projected ion beam direction. All the ripples in this study show a [001] direction with **B** = [110]. This is shown in figure 7.15(a), (b) for T2S1 and T2S0.

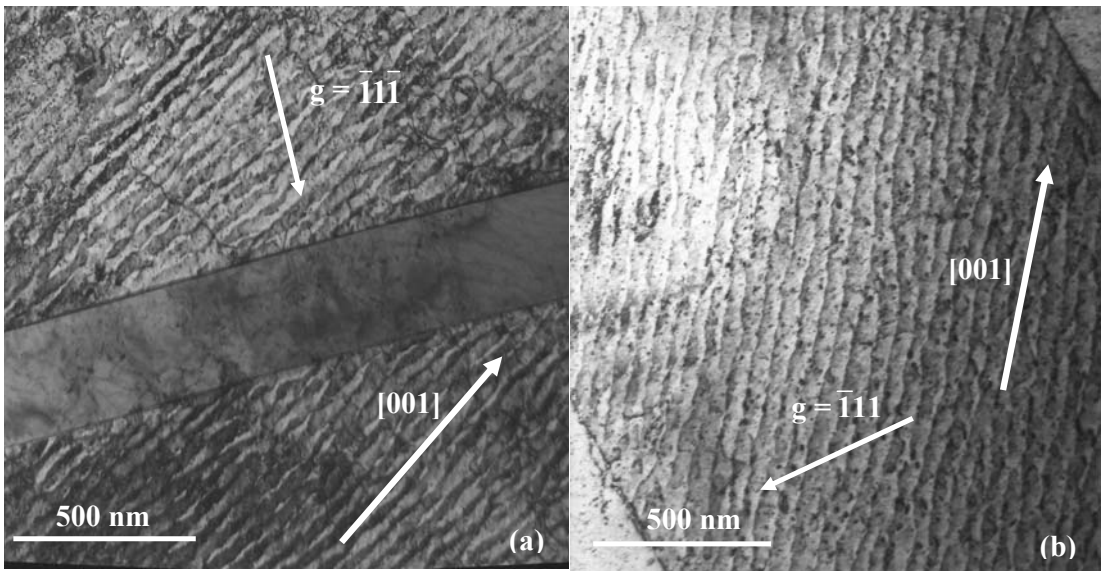

Figure 7.15: (a) Ripple structures in T2S1 taken with the EM420, **(b)** Ripple structures in T2S0 taken with the CM20.

Crystallographically dependent ripple formation has been reported by Qian *et al.* (2004) for Ga^+ ion bombarded tin surfaces. These ripples with magnitudes in the order of microns show similar traits to the ones found in this study in the sense that ripples formed in different grains are oriented in different directions relative to each other. If

the ripples found in this study were indeed ion beam damage dependent on beam direction, it would be expected that two adjacent grains would have ripples with the same orientation, the ripples simply continuing from one grain over the grain boundary to the next grain. Further more as was the case when comparing the ripples found in this study to those reported by Chan *et al.* (2006), the ripples found by Qian et al. (2004) are larger than those found in this study. This might indicate that the ripples are of a size which does not correspond to ion induced artefacts. Furthermore, as can be seen in figure 7.16 these structures were also noticed on the edge of the electron transparent regions of the TEM samples. It is highly unlikely that physical structures caused by ion damage can be contained in an area this thin.

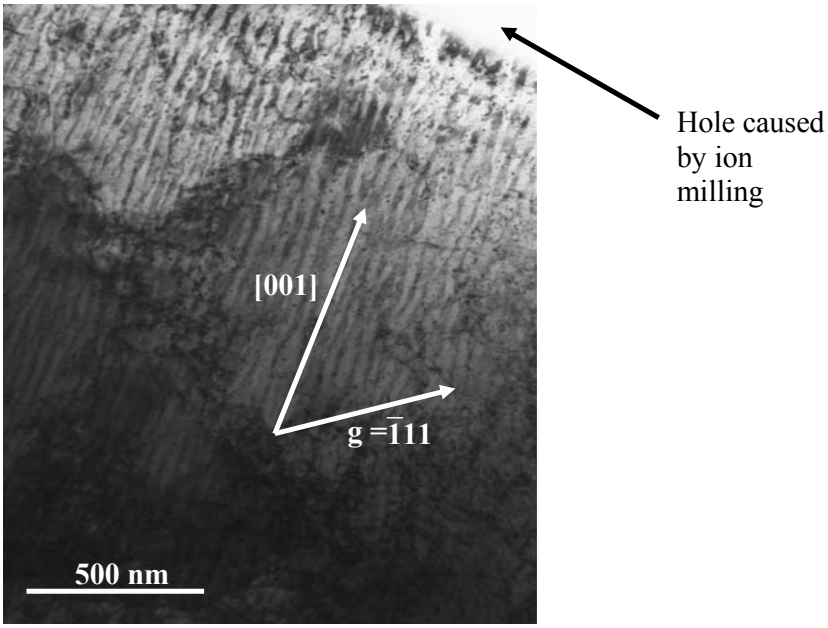

Figure 7.16: Image of T1S2 taken on the CM20 showing ripple structures on edge of hole caused by ion milling.

All of the above point to the possibility that these structures might be dislocation arrays. If it is assumed that these dislocations are pure edge dislocations with a [001] projected direction in the (110) plane and by referencing table 7.5, it can be seen that the only possible Burgers vector is of the type $\mathbf{b} = {}^{a}/_{2}[1\,\bar{1}\,0]$. Figure 7.17 shows three images of the same grain using different diffracting vectors. In figure 7.17 (a, b) the ripples a clearly visible indicating that if these ripples are indeed edge dislocations, the $\mathbf{g}\bullet\mathbf{b}$ criterion should be non zero. Using the possible Burgers vector $\mathbf{b} = {}^{a}/_{2}[1\,\bar{1}\,0]$

and determining **g•b** for figure 7.16 (a), (b) it is found that **g•b** = 2 for figure (a) with **g** = $2\bar{2}0$ and **g•b** = 1 for figure (b) with **g** = $1\bar{1}1$. In the case of figure 7.17 (c) with **g** = 002, **g•b** = 0. This means that the ripples should be invisible using this diffracting vector, as is the case. The ripples are easily viewed with **g** = $1\bar{1}1$, with **g** = $2\bar{2}0$ producing a less distinct ripple pattern. This is contrary to what is expected, as **g•b** is larger for **g** = $2\bar{2}0$ than for **g** = $1\bar{1}1$. This is not understood. One possible reason is that the two beam condition in the case of **g** = $1\bar{1}1$ was better fulfilled than in the case of **g** = $2\bar{2}0$.

These ripples also display some periodicity in that they end in a triangle or pointed shape. This indicates that the diffracting contrast that is seen originates from varying depths in the sample which corresponds to an dislocation forming and angle with the image plane. The dislocations assigned to these structures are indeed inclined to the (110) plane.

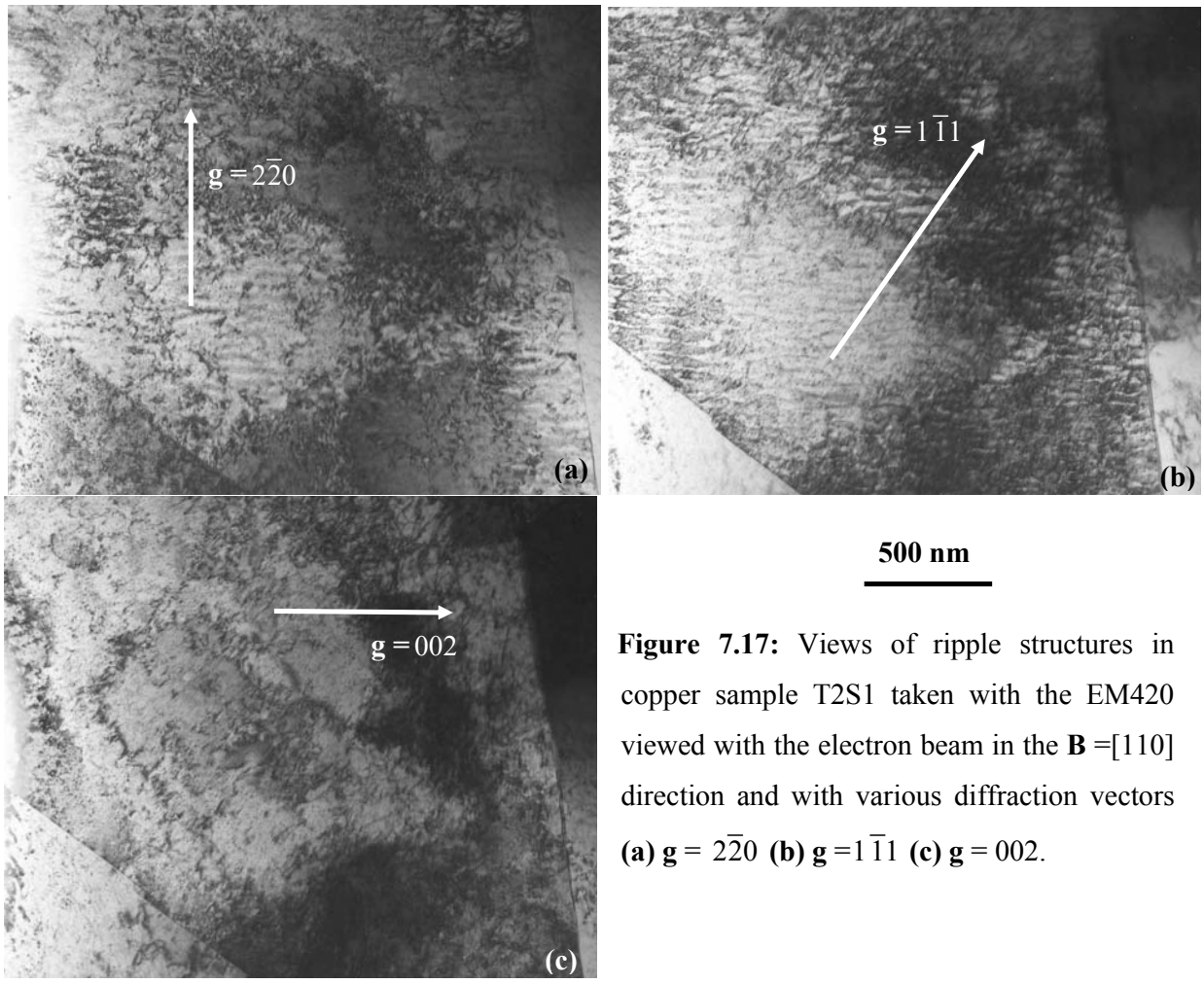

Figure 7.17: Views of ripple structures in copper sample T2S1 taken with the EM420 viewed with the electron beam in the **B** =[110] direction and with various diffraction vectors **(a)** **g** = $2\bar{2}0$ **(b)** **g** = $1\bar{1}1$ **(c)** **g** = 002.

Furthermore, if the [001] direction of these dislocations is considered, the projected direction in the (111) plane can be determined. Subsequently the angle between dislocations in a grain, and the dislocations in an adjacent twin can be determined. Such a situation is shown in figure 7.18.

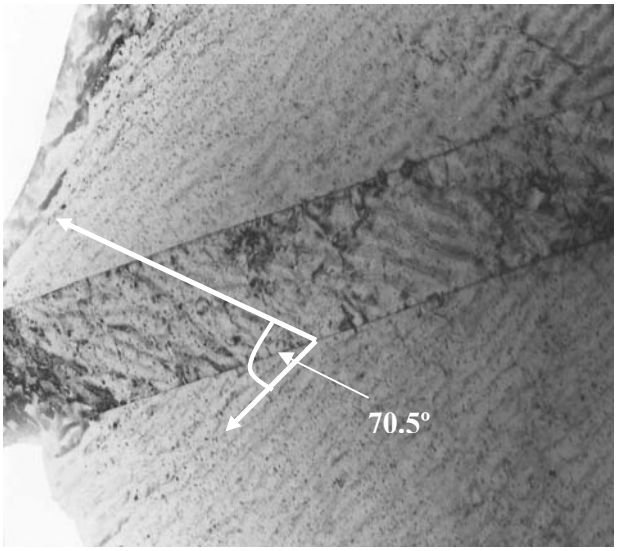

Figure 7.18: Ripple structures over twin boundaries.

Referring to figure 3.9, a $(\bar{1}11)$ twin plane viewed edge on with **B** = [110] lies projected along the $[1\bar{1}2]$ direction and thus makes a 35.25º angle with the [001] direction. Such dislocations should thus meet at 2(35.25º) = 70.5º at the twin boundary as seen in figure 7.18.

7.3.4 Oxide layer

While investigating the occurrence of twinning in a sample, double diffraction in the Selected Area Diffraction (SAD) pattern (figure 7.19(a)) of the [110] zone axis was observed in a grain having no twins. Figure 7.19(b) shows the diffraction pattern of a different copper sample without the secondary reflections. Energy Dispersive X-Ray Spectroscopy (EDS) analysis revealed that in addition to copper, the chemical composition of the sample included approximately 10% oxygen. Interstitial Gas Fusion Analysis of the bulk material from which the samples were extracted, however, showed that the chemical composition only included 30 ppm oxygen (see

chapter 4.7). This indicated that the secondary reflections were most likely due to an oxide growth on the sample.

Copper has two commonly occurring oxides: CuO and Cu_2O (Zhou, 1996). The secondary reflections in figure 7.19(a) closely follow the basic pattern of the reflections from the copper matrix. This suggested that the oxide had a crystal structure similar to the FCC structure of copper, and that the oxide formed an epitaxial layer. As CuO has a monoclinic structure, this left Cu_2O which has a simple cubic structure as the likely candidate.

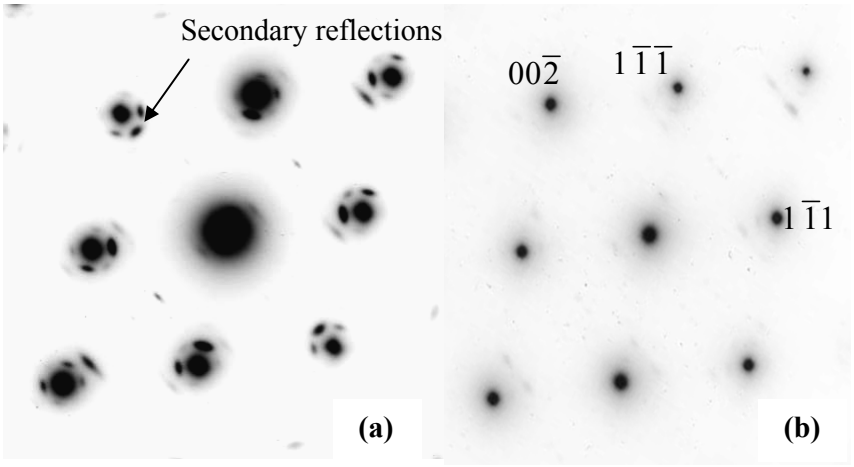

Figure 7.19: (a) SAD pattern of copper showing double diffraction in the [110] zone axis, and **(b)** showing SAD pattern without extra reflections.

This could be confirmed using measurements from figure 7.19(a). By measuring the distance $D = 2R$ between two inner reflections resulting from the oxide in a certain direction, the interplanar spacing of the oxide could be determined using equation 7.2. When the interplanar spacing is known for a certain direction, the lattice parameter of the oxide can be determined using equation 7.3. This was done for both the possible <111> type directions and the $[00\bar{2}]$ direction. The measurements are shown in table 7.6. It followed that the oxide had a lattice parameter of 0.42 nm which compares well to the theoretical value of 0.422 nm for Cu_2O.

Table 7.6: Determination of oxide lattice parameter.

hkl	R (mm)	d (nm)	*a* (nm)
$1\bar{1}1$	9.75	0.246	0.426
$1\bar{1}\bar{1}$	9.75	0.246	0.426
$00\bar{2}$	11.37	0.211	0.421
			$a = 0.424 \pm 0.003$

The occurrence of Moiré fringes in a bright field image (figure 7.20) corresponding to the SAD pattern in figure 7.19(a) further confirmed that this oxygen formed part of an oxide layer, and was not contained in the copper matrix itself.

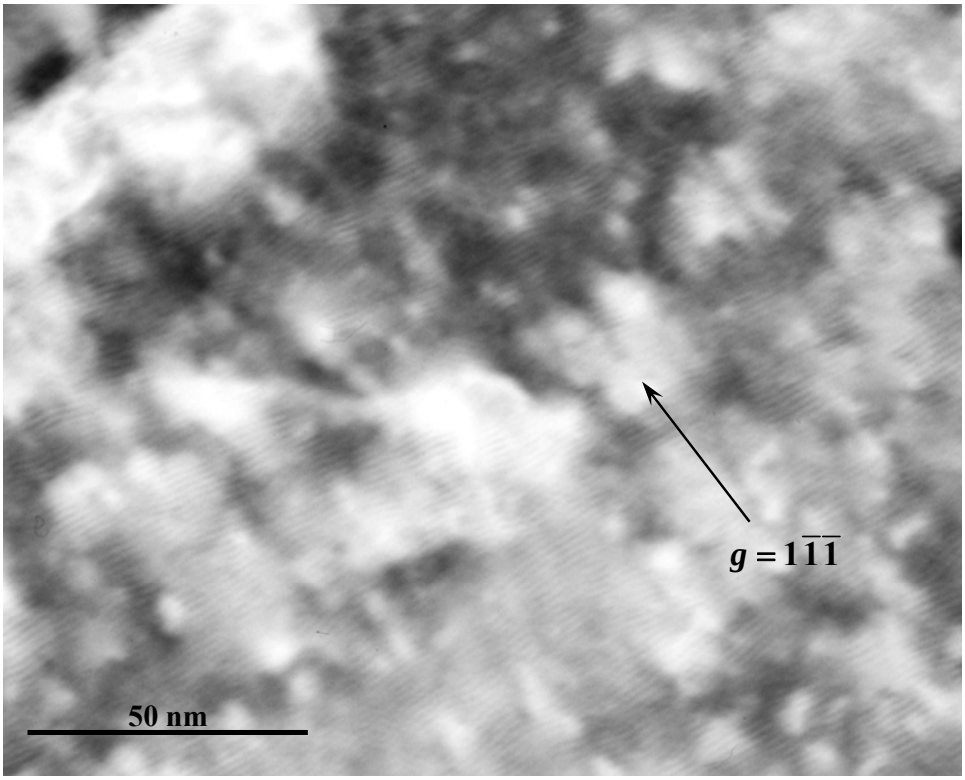

Figure 7.20: Bright field image showing Moiré fringes.

Moiré patterns occur from overlapping crystals as in composite films or in multiple phase systems i.e. a crystal with an oxide layer. Two general cases must be considered (Williams and Carter, 1996, p445):

- Parallel Moiré fringes are formed if two parallel planes of different spacings are reflecting. The lattice spacings (d_1 and d_2) differ only in magnitude. Fringes can be observed with distances

$$d = \frac{d_1 d_2}{|d_1 - d_2|} \qquad (7.7)$$

- A rotational Moiré pattern is formed when planes with equal spacing d, but rotated through an angle α, diffract together. Obtaining the Moiré spacing is more complicated, but this was unnecessary as the image could be explained using parallel Moiré fringes.

The spacing of the Moiré fringes found in figure 7.20 was measured to be 1.4 nm. The Moiré fringe spacing for Cu_2O for the {111} planes were calculated as 1.39 nm using the interplanar spacings d_1 = 0.209 nm and d_2 = 0.246 nm of Cu and Cu_2O respectively (see table 7.7) and calculated using equation 7.7. Hence the theoretical Moiré spacing compares well with the measured value. This procedure was repeated for different Moiré fringes on the (002) plane, and the theoretical value of 1.20 nm corresponded to the measured value of 1.2 nm. This then serves as further confirmation that the oxide is indeed Cu_2O.

Table 7.7: Calculations and values used to determine Moiré spacings.
a (Cu) = 0.3615 nm (Askeland, 1998, p830)
a (Cu_2O) = 0.42685 nm (Kirfel *et al*., 1990)

h	k	l	d_1 (nm)	d_2 (nm)	d (nm)
1	1	1	0.209	0.246	1.39
0	0	2	0.181	0.213	1.20

Although this oxide layer is not directly related to the study of shaped charges, it is none the less of academic importance.

7.3.5 Ion milling damage

The majority of the images taken of the copper samples show a distinct background of small defects, most likely dislocation loops. It is well known that ion milling can produce artefacts (Williams and Carter, 1996, p163-165). Figure 7.21(a) shows an image of copper sample T2S0 displaying these dislocation loops. They appear as speckles on the image. This sample was then etched for 20 seconds at 55ºC using a solution of 57 ml H_3PO_4, 20 ml HNO_3, and 16 ml acetic acid (Vander Voort G.F, 1989). This was done in an attempt to remove this surface damage caused by the ion milling. As can be seen in figure 7.21(b), this attempt proved successful, as no dislocation loops can be seen. This confirms that the dislocation loops are indeed ion damage, and are not a inherent characteristic of the sample material.

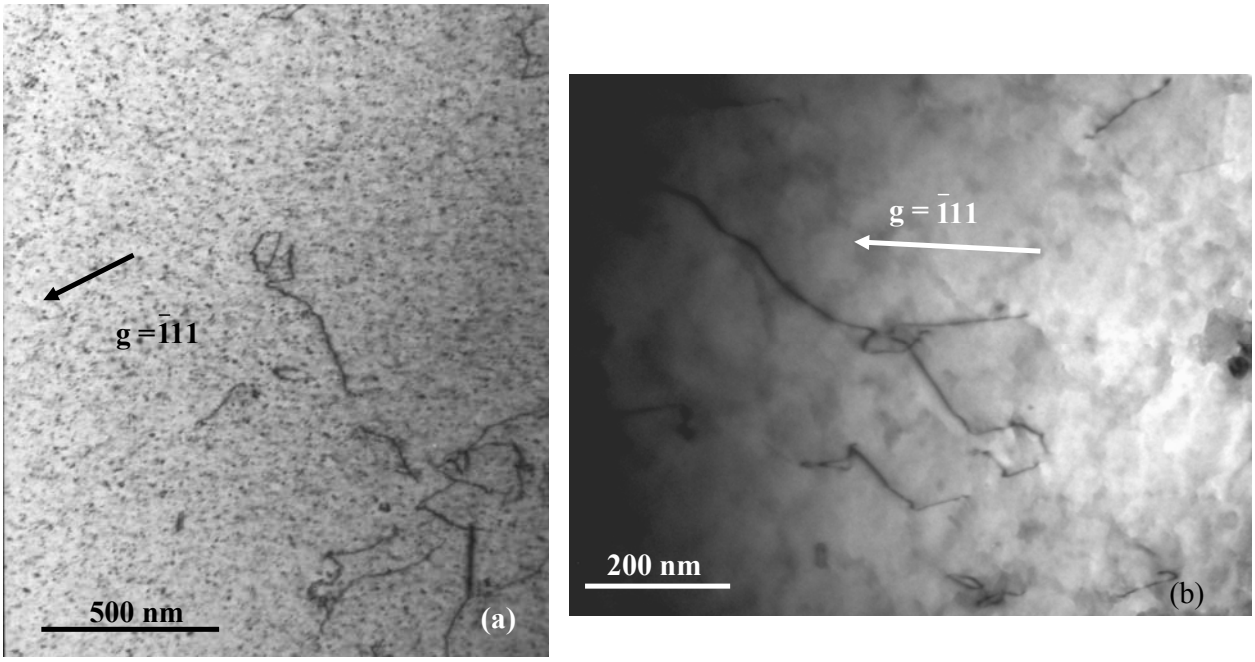

Figure 7.21: (a) Image of sample T2S0 taken on the CM20 showing dislocation loops **(b)** Image of the same sample taken on the CM100 after etching.

7.4 Results for molybdenum

7.4.1 Overview

Analysis of the molybdenum TEM results proved challenging. This was due to additional contrast on the images which is thought to be ion induced damage which occurred during the ion milling stage of the sample preparation. Although this contrast is not entirely independent of crystal orientation, it does exhibit the general trend of displaying similar contrast on both sides of a grain boundary as can be expected from such damage. This can be seen in figure 7.22.

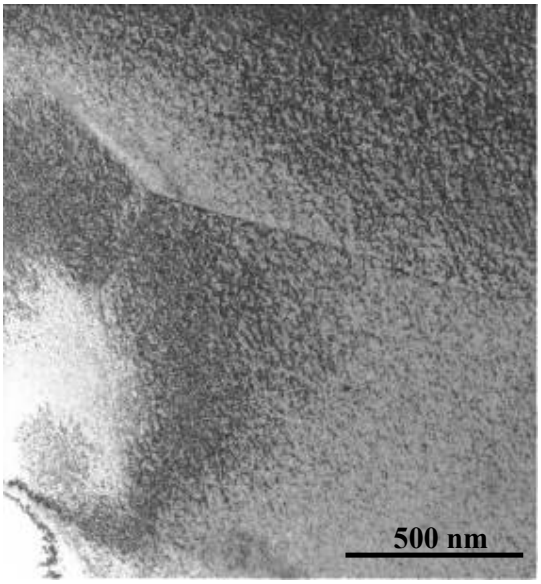

Figure 7.22: Image of molybdenum sample T2S0 taken on CM20 showing a well defined grain boundary.

Furthermore, the thinned region showed evidence of excessive bending. This evidence in the form of bend contours can be seen in figure 7.23(a). Figure 7.23(b) shows an image bend contours obtained from the literature (Williams and Carter, 1996, p374) Besides adding unnecessary contrast, this bending also necessitated additional care in ensuring that the right diffraction pattern was used for each image, as slight changes in the diffraction pattern would occur even when different areas in the same grain were viewed.

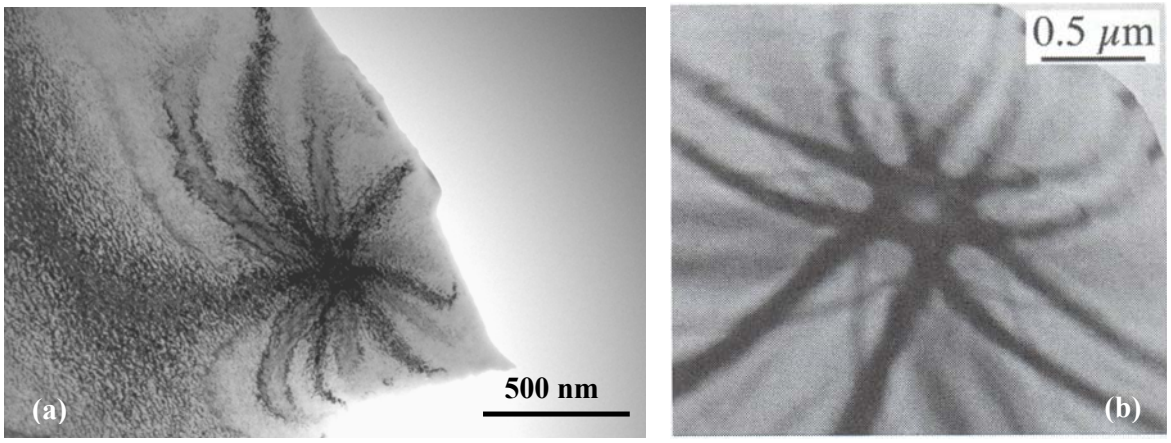

Figure 7.23: (a) Image of molybdenum sample T0S2 taken on CM100 showing bend contours, **(b)** Bend contours in Al_2O_3 (Williams and Carter, 1996, p374).

In both cases mentioned above, the damage is attributed to the ion milling used during sample preparation. Due to this damage caused by the ion milling, and the fact that the annealing of the molybdenum samples did not produce the desired microstructures, only five of the nine molybdenum samples were analyzed using the TEM. Samples T0S0, T2S0, T1S1, T0S2 and T2S2 were analysed. Figures 7.24 - 7.28 show representative images of these samples

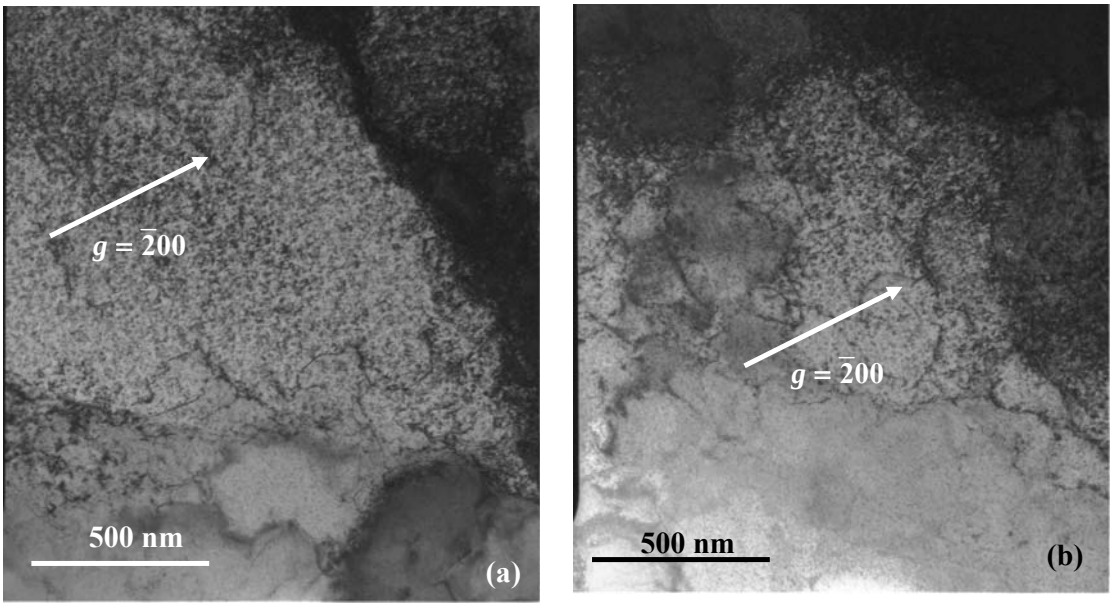

Figure 7.24: (a), (b) Images of molybdenum sample T0S0 taken on the CM20 with **B** = [031].

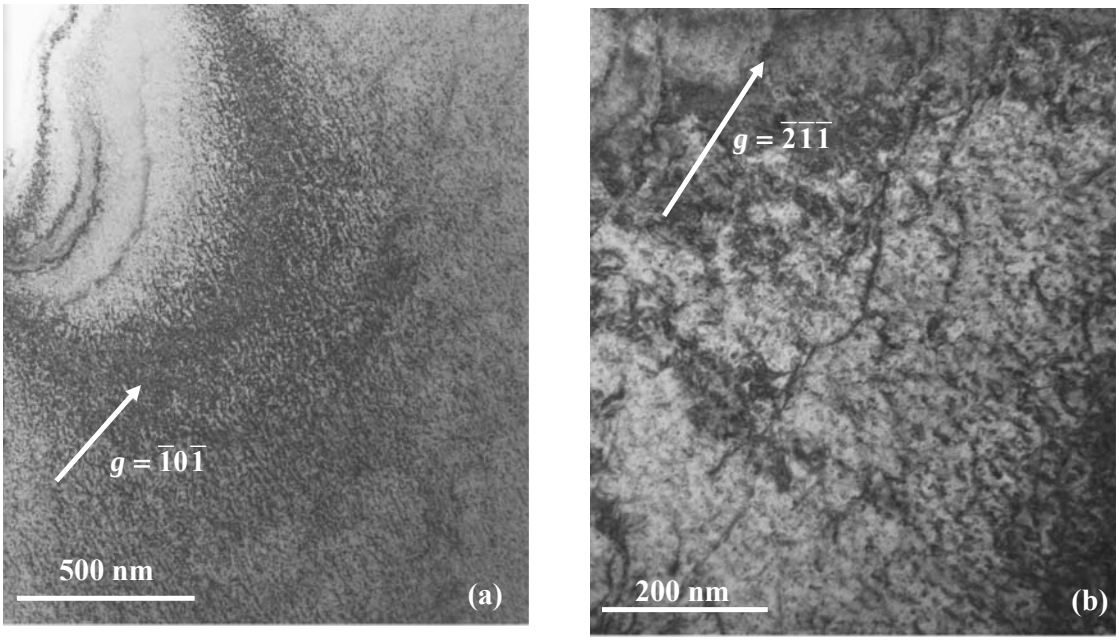

Figure 7.25: (a), (b) Images of molybdenum sample T0S2 taken on the CM20 with **B** = [$\bar{1}$11].

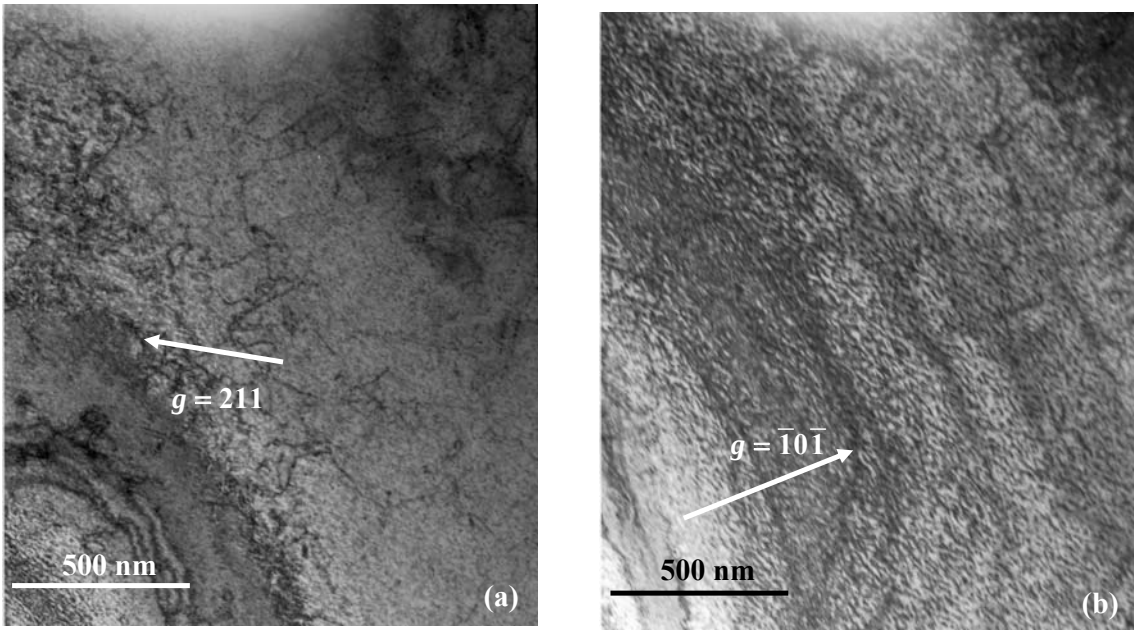

Figure 7.26: (a), (b) Images of molybdenum sample T1S1 taken on the CM20 with **B** = [$\bar{1}$11].

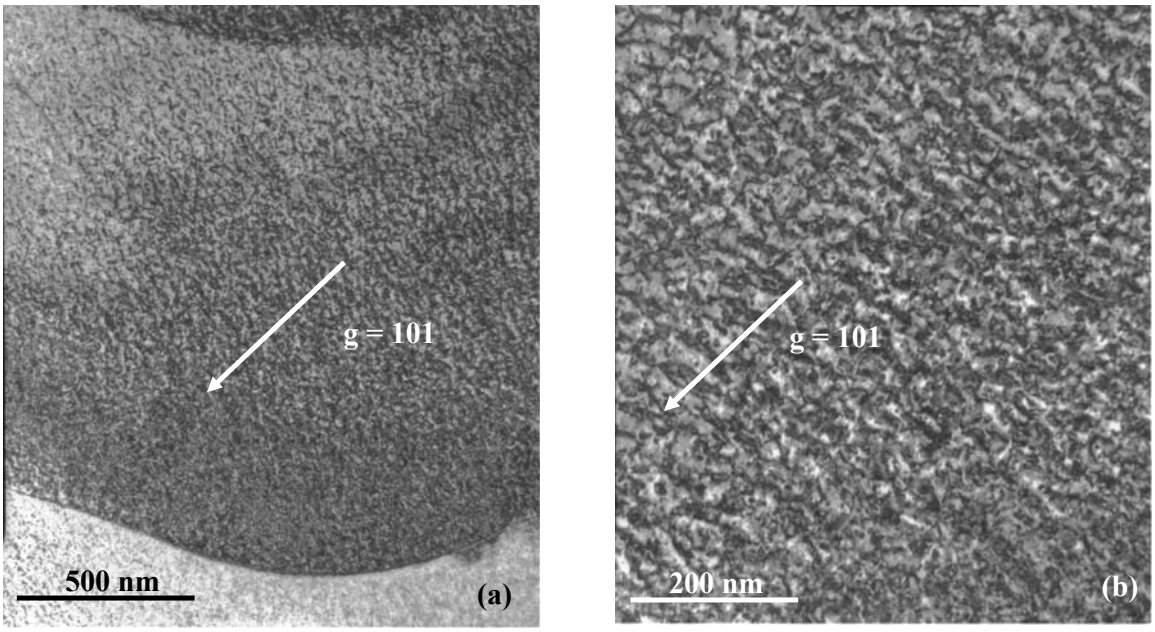

Figure 7.27: (a), (b) Images of molybdenum sample T2S0 taken on the CM20 with **B** = [$\bar{1}$11].

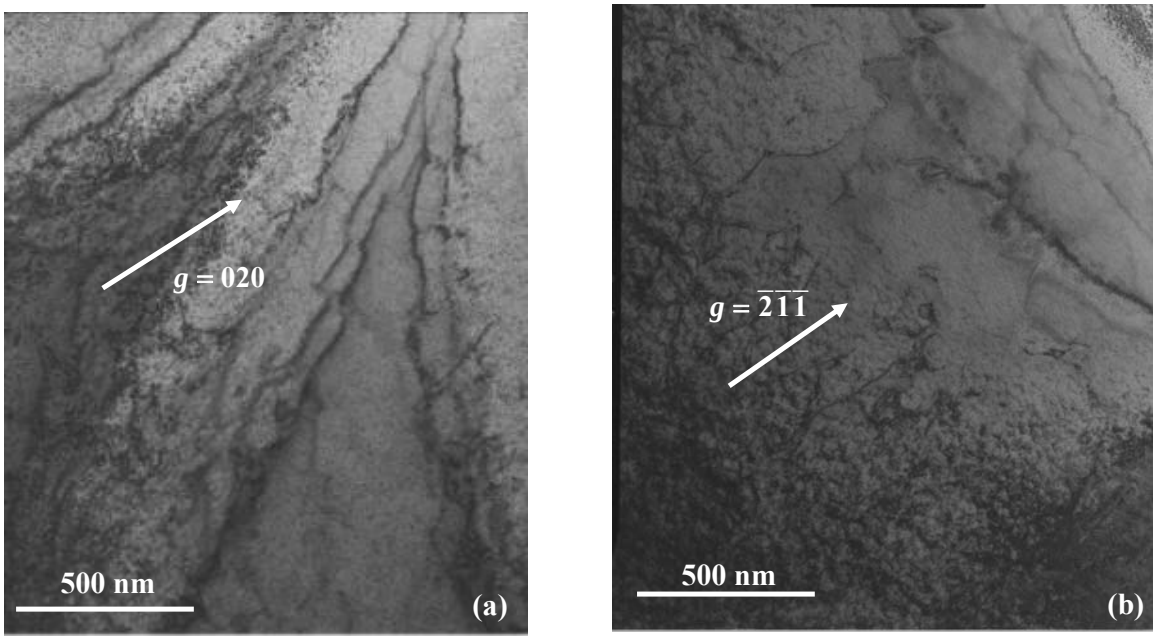

Figure 7.28: Images of molybdenum sample T2S2 taken on the CM20. **(a) B** = [001], **(b) B** = [$\bar{1}$11].

The ion damage mentioned earlier is visible in all of the images above. In addition, bend contours can be seen in figure 7.28 (a, b) of T2S2. The images of T0S0 in figure 7.23 show dislocation segments, but no clear grain boundaries are present. In contrast, sample T2S0 in figure 7.27(a) show well defined grain boundaries, and is virtually devoid of any dislocation segments. Figure 7.27(b) show the ion damage at a large magnification. While sample T1S1 in figure 7.26 show dislocation segments, these segments tend to be shorter in length than those noticed in T0S2 and T2S2. Interestingly enough, no evidence of twinning was found in any of the molybdenum samples. This indicates that in the case of the deformed molybdenum the deformation mechanism must be that of slip.

7.4.2 Dislocation analysis

It is generally accepted that the possible slip systems of BCC metals are {110}<111>, {112}<111> and {123}<111> systems i.e. slip occurs on the {110}, {112}, or {123}-type planes and in the <111>-type directions [Askeland, 1998, p84]. The Burgers vector associated with such slip is $\mathbf{b} = {}^{a}/_{2}\langle 111\rangle$. Figure 7.29 shows images of the same area of molybdenum sample T2S2 with these diffraction vectors. The arrows point to areas that are the same in each image. Possible Burgers vectors, along with the results of the **g•b** visibility criterion, for these three different diffraction vectors are shown in table 7.8.

Table 7.8: Possible Burgers vectors and visibility criteria.

Burgers vector	**g•b** ($\mathbf{g} = 200$)	**g•b** ($\mathbf{g} = 12\bar{1}$)	**g•b** ($\mathbf{g} = \bar{1}2\bar{1}$)
$^{a}/_{2}[111]$	1	1	0
$^{a}/_{2}[\bar{1}11]$	-1	0	1
$^{a}/_{2}[1\bar{1}1]$	1	-1	-2
$^{a}/_{2}[11\bar{1}]$	1	2	1

From table 7.8 it can be seen that an image with **g** = 200 should show all dislocations with a Burgers vector of the type $\mathbf{b} = {}^{a}/_{2}\langle 111\rangle$. This is because the visibility criterion

is always non zero. In the case of **g** = $12\bar{1}$ and **g** = $\bar{1}2\bar{1}$ these dislocations will then be visible or invisible depending on the exact type of $^{a}/_{2}$<111> Burgers vector. By comparing the visible dislocations in images with these three different diffraction vectors, the nature of the Burgers vector of these dislocations can be determined.

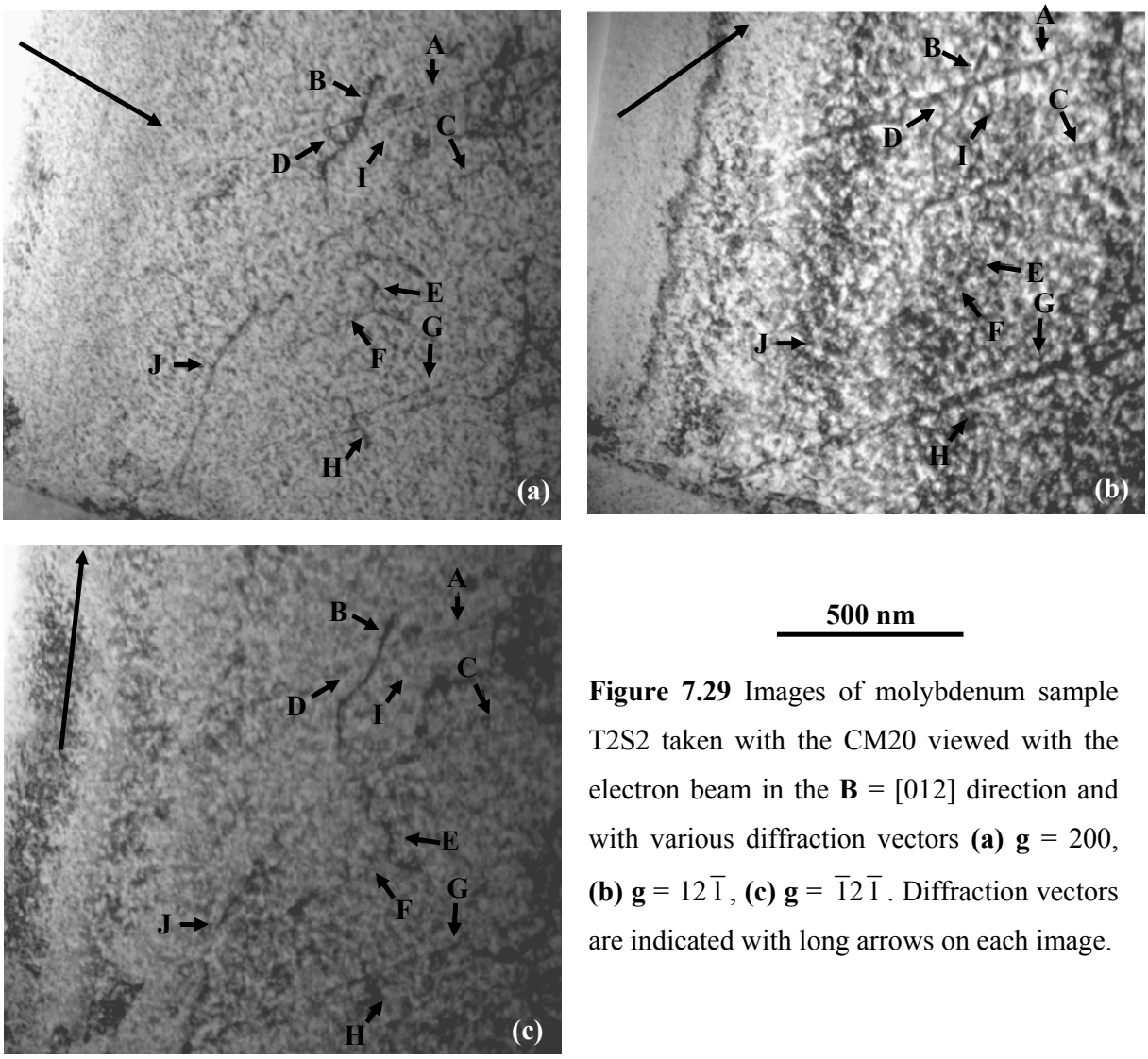

Figure 7.29 Images of molybdenum sample T2S2 taken with the CM20 viewed with the electron beam in the **B** = [012] direction and with various diffraction vectors **(a) g** = 200, **(b) g** = $12\bar{1}$, **(c) g** = $\bar{1}2\bar{1}$. Diffraction vectors are indicated with long arrows on each image.

Dislocations in these areas are marked **A- J**. Table 7.9 gives these dislocations with a indication of the dislocations contrast for each **g** vector**.**

Table 7.9: Marked dislocations for figure 7.29 with each dislocations contrast visibility for different diffracting vectors.

Dislocation	g = 200	g = $12\bar{1}$	g = $\bar{1}2\bar{1}$
A	Weak	Strong	Weak
B	Strong	Weak	Strong
C	Weak	Strong	Weak
D	Weak	Weak	Invisible
E	Weak	Invisible	Weak
F	Weak	Invisible	Weak
G	Weak	Strong	Weak
H	Weak	Invisible	Weak
I	Invisible	Weak	Invisible
J	Weak	Weak	Strong

If these values are compared to those in table 7.8, the marked dislocations can be grouped into dislocations with a certain Burgers vector. This is shown in table 7.10.

Table 7.10: Dislocations with their assigned Burgers vectors.

Dislocations	Burgers vector
A, C, G	$^{a}/_{2}[11\bar{1}]$
E, F, H	$^{a}/_{2}[\bar{1}11]$
B, J	$^{a}/_{2}[1\bar{1}1]$
D	$^{a}/_{2}[111]$
I	-

As can be seen in table 7.10 the dislocations marked **A**, **C** and **G** all have a Burgers vector of the type $^{a}/_{2}[11\bar{1}]$. These dislocations, which are long and straight were at first thought to be twins. In figure 7.30(a) they do appear like band structures, and the accompanying diffraction pattern does show additional diffraction spots. A dark field image using the extra reflection marked **R** in figure 7.30(b) however indicated that these bands were not twins. These additional reflections present in figure 7.30(b) are attributed to reflections from a neighbouring grain.

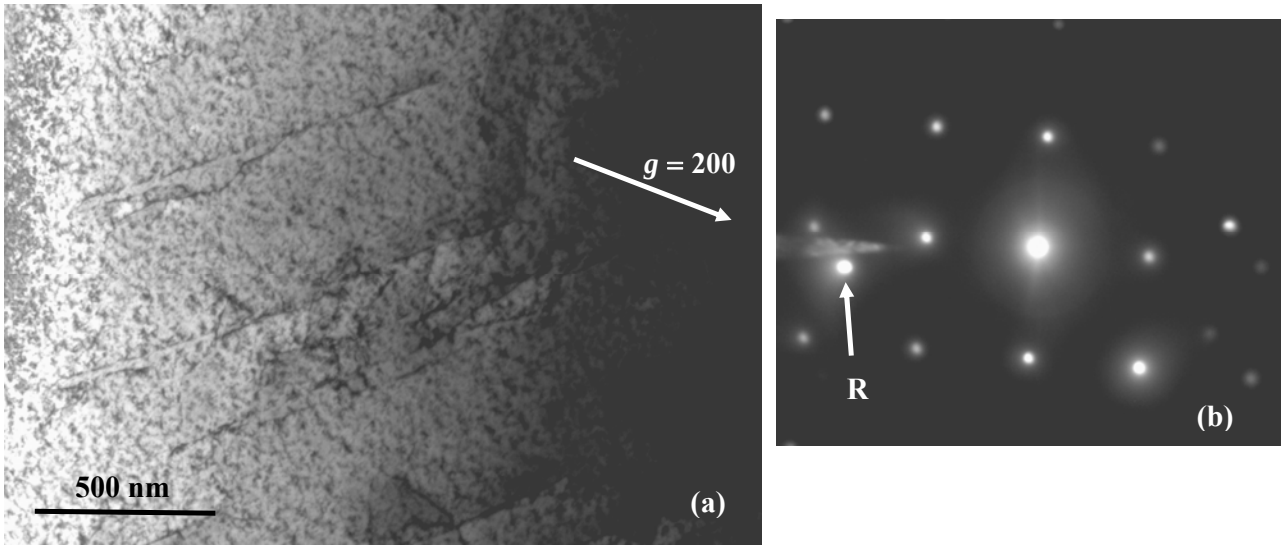

Figure 7.30: (a) Image of band like structures in molybdenum sample T2S2 taken on the CM100 with **B** = [001], **(b)** Diffraction pattern of (a) showing additional reflections. The feature on the left of the diffraction pattern above the spot marked **R** is an artefact of the TEM camera.

Dislocations **E**, **F** and **H** are short dislocation segments with a Burgers vector of the type $^{a}/_{2}[\bar{1}11]$. Dislocations **B** and **G** on the other hand are long dislocations with a Burgers vector of the type $^{a}/_{2}[1\bar{1}1]$. Dislocation **D** has a Burgers vector of the type $^{a}/_{2}[111]$. Of concern is the dislocation marked **I**. This loop-like dislocation can not be explained using a dislocation of the type $\mathbf{b} = {}^{a}/_{2}\langle 111\rangle$.

A similar procedure was followed for the grain adjacent to the one shown in figure 7.29. This grain was imaged using zone axis **B** = [001]. Table 7.11 shows the various possible Burgers vectors as well as the visibility criterion for three different **g**-vectors. Images taken using these diffraction vectors are shown in figure 7.31, as well as an overlay chart, which indicates where on the image, the dislocations that will be discussed occur.

Table 7.11: Possible Burgers vectors and visibility criteria.

Burgers vector	g•b ($g = \bar{2}00$)	g•b ($g=1\bar{1}0$)	g•b ($g = 0\bar{2}0$)
$^{a}/_{2}[111]$	-1	0	-1
$^{a}/_{2}[\bar{1}11]$	1	-1	-1
$^{a}/_{2}[1\bar{1}1]$	-1	1	1
$^{a}/_{2}[11\bar{1}]$	-1	0	-1

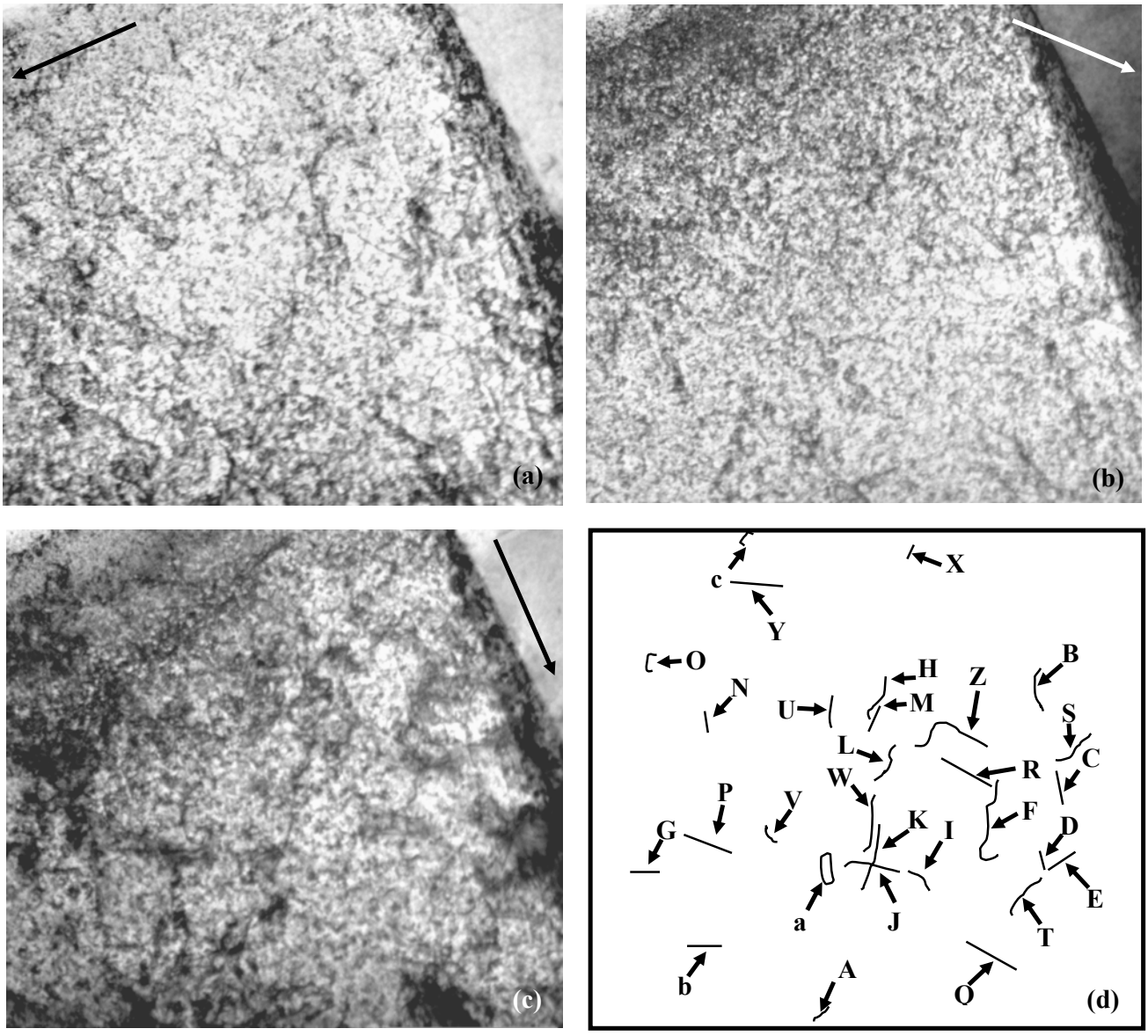

Figure 7.31: Images taken on the CM100 with **B** = [001] **(a) g** = $\bar{2}00$, **(b) g** = $1\bar{1}0$ **,** **(c) g** = $0\bar{2}0$ **, (d)** overlay**.** Diffraction vectors are indicated using long arrows.

Table 7.12 gives a description of the contrast seen in each image (figure 7.31) for the marked dislocations.

Table 7.12: Marked dislocations for figure 7.31 with each dislocations contrast visibility for different diffracting vectors.

Dislocation	$\mathbf{g} = \bar{2}00$	$\mathbf{g} = 1\,\bar{1}0$	$\mathbf{g} = 0\bar{2}0$
A	Strong	Strong	Invisible
B	Invisible	Invisible	Strong
C	Invisible	Strong	Strong
D	Invisible	Invisible	Strong
E	Weak	Invisible	Strong
F	Invisible	Invisible	Strong
G	Weak	Weak	Strong
H	Invisible	Invisible	Strong
I	Invisible	Invisible	Strong
J	Invisible	Strong	Invisible
K	Strong	Invisible	Invisible
L	Invisible	Invisible	Strong
M	Strong	Strong	Invisible
N	Strong	Strong	Invisible
O	Strong	Strong	Invisible
P	Strong	Strong	Invisible
Q	Strong	Weak	Invisible
R	Strong	Strong	Invisible
S	Weak	Strong	Invisible
T	Strong	Invisible	Invisible
U	Strong	Invisible	Invisible
V	Strong	Invisible	Strong
W	Invisible	Weak	Strong
X	Invisible	Weak	Strong
Y	Invisible	Invisible	Strong
Z	Invisible	Invisible	Strong
a	Invisible	Invisible	Strong
b	Invisible	Weak	Strong
c	Strong	Invisible	Invisible

Considering the column for $\mathbf{g} = \bar{2}00$, from table 7.11 it is clear that for this diffraction vector all dislocations should be visible in figure 7.31(a). From table 7.12, however, it is apparent that this is not always the case. In addition, all dislocations should also be visible in figure 7.31(c), which is not true. A noticeable tendency is that dislocations that are visible for $\mathbf{g} = 0\bar{2}0$, are invisible for $\mathbf{g} = 1\bar{1}0$ and vice versa. It thus appears that the dislocations do not have Burgers vectors of the type $\mathbf{b} = {}^{a}/_{2}\langle 111\rangle$. This is however a bold statement and considering the quality of images used to perform the analysis with, it is felt that further research is necessary to obtain any clear results in this regard. The background contrast in the images are simply too strong to make accurate dislocation analysis possible. This background contrast has its origin in small dislocation loops as can be seen in figure 7.32. It is believed that these are an artefact of ion milling, and that the results of this study would have been of a higher quality if electro-polishing were used to prepare the TEM samples. A double tilt sample holder is also necessary to obtain useful diffraction vectors.

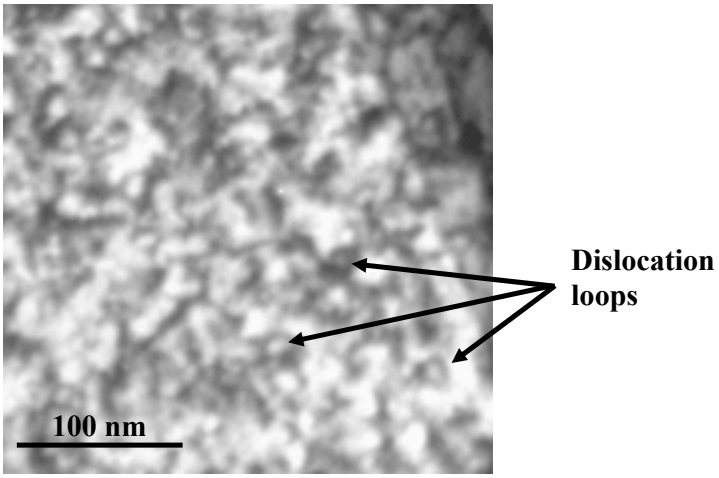

Figure 7.32: Dislocation loops in T2S2. Image taken using the CM100 TEM.

7.5 Discussion and conclusion

The TEM analysis proved challenging with some aspects of the results being strongly influenced by the sample preparation procedure. In both the copper and molybdenum samples, ion milling produced dislocation loops which added to the amount of background contrast viewed in the images. Although not presenting much of a problem in the analysis of the copper samples, these loops definitely complicated the analysis of the molybdenum samples. These loops were larger in the case of the molybdenum samples, when compared to those in the copper sample. The reason for this is not understood. In addition, the copper samples not imaged within a reasonable time span after preparation oxidized, forming a Cu_2O layer. This layer, contributing reflections to the diffraction patterns is unnecessary and can be avoided by performing the final sample preparation as close as possible to when the actual TEM investigation is performed. Similar remarks regarding copper have also been made by Barrett and Massalski, (1980, p590). This is of course difficult when, as in this case, facilities of other institutions are used. Although the punching of TEM samples proved effective in the case of the copper samples, too many molybdenum samples broke during punching because they were too brittle. It is advised that both the copper and molybdenum TEM samples should be sliced from the SHPB samples and cut to their final diameter of 3 mm using EDM. This will eliminate the need for punching. These samples can then be polished to a thickness of 100 μm. The final thinning should then be performed using electro-chemical polishing with a possible dimpling step if the 100 μm proves to be too thick.

Contrary to what was expected if considering the crystal structures of the two materials, no twinning was observed in the molybdenum samples, while twinning proved to be a deformation mechanism in the annealed copper samples. This twinning occurred at a lower strain rate than previously predicted.

Dislocations analysed in copper sample T1S0 occurred in entangled networks separated with areas containing no dislocation. These dislocations were found to have Burgers vectors of the type $\mathbf{b} = {}^{a}/_{2}\langle 110\rangle$ but proved to be mixed dislocations i.e. not pure edge or screw dislocations. Pure edge dislocations with a [100] projected

direction in the (110) plane with a Burgers vector of the type $\mathbf{b} = {}^{a}/_{2}[1\bar{1}0]$ were however found in the copper samples. These dislocation arrays appear as ripple-like structures.

Some dislocations in the molybdenum samples have Burgers vectors of the expected type $\mathbf{b} = {}^{a}/_{2}\langle 111\rangle$. There are, however, exceptions. This is an important observation, and further research would have to be performed to obtain any certainty in this regard.

7.6 References

Askeland D.R. **[1998]** *The Science and Engineering of Materials*, Stanley Thornes Ltd.

Barrett C and Massalski T.B. **[1980],** *Structure of Metals*, Pergamon Press.

Chan W.L. and Chason E. **[2006]** *Nuclear Instruments and Methods in Physics Research* **B242** p228.

Eddington J.W. **[1975]** *Practical Electron Microscopy in Material Science, Vol 2*: *Diffraction in the electron microscope*, MacMillian.

Hornstra J. **[1958]** *Journal of Physics and Chemistry of Solids* **5** p129.

Huang C.X., Wang K., Wu S.D., Zhang Z.F., Li G.Y. and Li S.X. **[2006]** *Acta Materialia* **54** p655.

Kirfel A. and Eichhorn K.D. **[1990]** *Acta Crystallographica A* **39** p1983.

Kittel C. **[1966]** *Introduction to Solid State Physics*, John Wiley and Sons, Inc.

Lee Y.S. and Lee D.N. **[2000]** *Journal of Material Science* **35** p6161

Loretto M.H. and Smallman R.E. **[1975]** *Defect Analysis in Electron Microscopy*, Chapman and Hall Ltd.

Meyers M.A., Vöhringer O. and Lubarda V.A. **[2001]** *Acta Materialia* **49** p4025.

Mizuno K., Yamamoto S., Okamoto H., Kuga M. and Hashimoto E. **[2002]** *Journal of Crystal Growth* **237** p367.

Niewczas M. **[2002]** *Philosophical Magazine A* **282(2)** p393

Qian H.X., Zhou W., Fu Y.Q., Ngoi B.K.A., and Lim G.C. **[2005]** *Applied Surface Science* **240** p140.

Toa. N.R., Wu X.L., Sui M.L., Lu J. and Lu K. **[2004]** *Journal of Materials Research* **19** p1623

Vander Voort G.F **[1989]** *Chemical and Electrolytic Polishing* in *ASM Handbook, Vol 9, Metallography and Microstructures* (Vander Voort G.F.), ASM international.

Von Heimendahl M. **[1980]** *Electron Microscopy of Materials, An Introduction*, Academic Press.

Williams D.B. and Carter C.B., **[1996]**. *Transmission electron microscopy, Vol 1-4,* Springer.

Zhou G. **[1996]** *Dynamics of copper investigated by In Situ UHV-TEM,* Ph.D. Thesis, University of Pittsburgh.

http://www.tf.uni-kiel.de/matwis/amat/def_en/index.htm accessed 29 May 2007 (H.Föll).

Chapter 8

Final Conclusions and Remarks

8.1 Introduction

The aim of this project was to characterize the microstructure and extended defects of copper and molybdenum shaped charge liners and to compare the roles that crystal structure, microstructure and strain rate play in the high strain rate deformation of metals. This knowledge would then enable the manufacturer of such weaponry to maximize the penetration potential of these weapons. Although certain aspects such as the annealing of the liners and the purity of the materials used can be directly addressed, it is felt by the author that a more fundamental and simplified approach is necessary to gain a more complete understanding of the processes and factors that influence the high strain rate deformation of materials. This will be discussed in detail in the following sections.

8.2 Conclusions regarding the copper used in this study

The copper material used in this study proved to be a relatively easy material to work with in terms of sample extraction, sample preparation and the analysis of the results. The only problem directly associated with the copper was the tendency of the material to form an oxide layer in a very short time span. This oxide layer caused additional reflections in the Selected Area Diffraction (SAD) patterns of the copper Transmission Electron Microscope (TEM) samples. It also made the use of the Electron Backscattered Diffraction technique very difficult. Similar remarks regarding copper have been made by other researchers (section 7.6). In addition, Ar^+ ion milling proved to be an unsatisfactory method when used to perform the final thinning of copper TEM samples, producing ion induced artefacts. The experimental

setup used for the Split Hopkinson Pressure Bar (SHPB) also was not suited for the straining of the soft annealed copper samples, causing double straining of some of the samples. Although these factors complicated some of the result analyses, useable results and conclusions were nevertheless obtained.

Chemical analysis of the copper material indicated that it has a high impurity concentration which should be reduced. This is especially true for the P, O, Ag, S and N concentrations. Agreement exists between researchers that an increase in the impurity concentrations of a shaped charge liner leads to a decrease in its performance. It is thus advisable that Denel Land Systems investigates this problem as soon as possible, to ensure that the maximum penetration is obtained from the shaped charges the company manufactures.

The as-received material consisted of a mangled, elongated grain structure as expected from a cold-worked article. The two annealing conditions used for the copper samples (300°C and 500°C for 30 minutes) proved to be satisfactory. The lower temperature produced a fine recrystallised microstructure with a grain size of 5 μm. The higher annealing temperature allowed grain growth, with grains averaging 9 μm. SHPB results of samples annealed under these two conditions proved to be very similar. In both cases the copper samples were very soft, resulting in double straining. This indicates that annealing, using either of these two temperatures does not have a significant influence on the stress–strain response of the copper material. As there is abundant evidence that a fine microstructure produces the best liner performance, it would make practical and economic sense to use the lower temperature (300°C). Modelling the stress-strain response of the liners annealed at the lower temperature might, however be complicated, as the SHPB results obtained with the copper samples annealed at the higher temperature (500°C) corresponded more closely with the Johnson-Cook model.

TEM results indicated the unexpected result that deformation twinning occurred in all of the annealed and strained samples. These results suggest that deformation twinning in FCC materials can occur at a lower strain rate than previously predicted. The occurrence of annealing twins in the annealed samples make a conclusive result difficult. However twins observed in the TEM were of an order of magnitude smaller

than the annealing twins observed in the annealed but unstrained samples. In addition, ripple-like dislocation arrays occurred in the annealed as well as unannealed samples, whether strained or not. These arrays consisted of pure edge dislocations with a [100] projected direction in the (110) plane with a Burgers vector of the type $\mathbf{b} = {}^{a}/_{2}[1\,\bar{1}0]$. Dislocations analysed in an unstrained copper sample occurred in entangled networks separated with areas containing no dislocation. These dislocations were found to have Burgers vectors of the type $\mathbf{b} = {}^{a}/_{2}\langle 110\rangle$ but proved to be mixed dislocations.

8.3 Conclusions regarding the molybdenum used in this study

The molybdenum material presented some challenges. Due to the material being hard and brittle, sample extraction proved difficult and time consuming. Electric Discharge Machining (EDM) and polishing of samples proved to be a tedious undertaking, and a number of samples were lost due to breakage during TEM sample punching. In addition the high recrystallisation temperature of molybdenum made it impossible to obtain a high enough annealing temperature in the available annealing oven to induce grain growth. Also very few previous publications on the high strain rate deformation of molybdenum could be obtained, most research concerning BCC material being performed on tantalum.

Chemical analysis indicated that the molybdenum liner contained a large number of impurities, the most prolific impurities being W, Fe, Cr, O, Ni, Ta, K and Ca. This is an aspect which requires urgent attention.

The as-received material had a large, mangled and elongated microstructure with grains up to 500 μm in size. Annealing at 1200°C for 30 minutes or 3 hours produced a recrystallised, unequiaxed microstructure with grains ranging from 47 μm to 92 μm in size. The longer annealing time changed nothing to the microstructure produced using the shorter time. Although failing in the requirement to produce a different microstructure, this is not considered to be a problem, as the best liner performance

will be obtained using a liner with a recrystallised microstructure as produced by the shorter annealing time. Although the grain size might appear large, similar results for molybdenum have been reported (section 3.4). However, the finest equiaxed grain structure possible is desirable for shaped charge liners. Obtaining a starting material with a finer microstructure would thus be a step in the right direction. In a sintered product this should not pose any manufacturing problems with regard to material hardness. If the current material is used, the annealing condition with the shorter time is recommended.

SHPB results of the material showed a high strain rate dependency. It would be interesting to compare these results with those obtained with strain rates in the ultra-high strain rate regime. This would not be possible using a SHPB, necessitating the use of explosive flyer plate techniques.

Interestingly, no evidence of twinning was found in these samples. This indicates that slip was the deformation mechanism. Although some of the dislocations identified had Burgers vectors of the type $\mathbf{b} = {}^{a}/_{2}\langle 111\rangle$, most could not be characterised. This is an important observation, and further research would have to be performed to obtain any certainty in the regard. Dislocation analysis was complicated by a background of small dislocation loops, which are believed to be ion milling artefacts.

8.4 General comments and suggestions for future work

This study provides a broad background for any future work. As suggested in section 8.1, it is felt that any future work should be simplified. Although such an academic approach might lack any immediate benefit for industry, it is believed that it will yield a better long term understanding of the high strain rate response of materials, which in turn will provide manufacturers of shaped charge liners with the necessary facts needed to produce superior products. One way to simplify such a study is to use commercial metals instead of an already forged liner. By using unforged commercial metal rod as sample material the extracting procedure will be simplified, which in turn

will produce very uniform samples, both in microstructure, and in sample shape and dimensions. This will lead to more consistent SHPB results. In the case of SHPB testing it is felt that such a study might be better served with samples that were strained to a higher degree. This can be achieved by using samples of a shorter length.

It is also recommended that the TEM sample preparation procedure as used in this study should be substituted with a procedure using electro-chemical etching for the final thinning. This will prevent the formation of any Ar^+ ion artefacts as found in this study. In the case of molybdenum, the punching of samples should also be replaced by wire EDM cutting.

If satisfactory samples can be prepared using the mentioned suggestions, TEM investigation with the emphasis on dislocation densities should be done to determine the accuracy of models like those found in Mostert *et al*. (1987) (section 1.1). Experimental evidence to support this model does not exist.